UNIVERSITY OF COPENHAGEN
FACULTY OF SCIENCE
NIELS BOHR INSTITUTE

EXPLORING SUPERCONDUCTING PHASES IN HYBRID NANOWIRE DEVICES

Davydas Razmadze

Ph.D. Thesis
Center for Quantum Devices
Niels Bohr Institute
University of Copenhagen

Academic advisor:
prof. Charles M. Marcus

Assessment committee:
Assoc. prof. Kasper Grove-Rasmussen
prof. Thomas Schäpers
Dr. Elsa Prada

This thesis has been submitted
to the Ph.D. School of the Faculty of Science,
University of Copenhagen

August, 2020

CONTENTS

ABSTRACT

The thesis explores the superconducting properties of hybrid InAs/Al nanowire devices were trivial and topological regimes can be studied using high/low-frequency measurement techniques.

The first chapter introduces the theoretical background of superconductivity to understand the phenomena in the experimental data.

We continue by presenting semiconducting nanowire quantum devices that were studied in this thesis. Detailed fabrication recipes for full/half-shell Al nanowire devices are introduced together with experimental setups for transport measurements.

The thesis continues by demonstrating improved tunability of overlapping gate geometries compared to conventional side-gated devices, allowing clean and effective characterization of hybrid nanowire junctions.

The following chapters present full-shell Al/InAs nanowires interferometer devices, where novel means of probing topological states in the nanowires are possible by changing the parity of the quantum-dot in the Josephson junctions. Further, the display of subgap-state splitting that decays with finite length in Majorana islands is presented, suggesting the topological nature of full-shell nanowires.

The thesis concludes with radio-frequency and dispersive readout methods that are compatible with nanowire-based quantum devices. This enables fast device tuning and characterization. The measured signal-to-noise ratios of these sensors suggest that these techniques could be used for future topological nanowire qubit measurements.

ACKNOWLEDGMENTS

PUBLICATIONS

1. **Davydas Razmadze**, Eoin C. T. O'Farrell, Peter Krogstrup, Charles M. Marcus.
   Quantum-Dot Parity Effects in Trivial and Topological Josephson Junctions.
   Accepted: Phys. Rev. Lett., (2020).
   arXiv:2005.11848

2. David M. T. van Zanten*, Deividas Sabonis*, Judith Suter*, Jukka I. Väyrynen, Torsten Karzig, Dmitry I. Pikulin, Eoin C. T. O'Farrell, **Davydas Razmadze**, Karl D. Petersson, Peter Krogstrup, Charles M. Marcus.
   Photon-assisted tunnelling of zero modes in a Majorana wire.
   Nat. Phys., **1**-6, (2020).

3. Deividas Sabonis*, Eoin C. T. O'Farrell*, **Davydas Razmadze**, David M. T. van Zanten, Judith Suter, Peter Krogstrup, Charles M. Marcus.
   Dispersive sensing in hybrid InAs/Al nanowires.
   Appl. Phys. Rev., **115** (10), 102601 (2019).

4. **Davydas Razmadze***, Deividas Sabonis*, Filip K. Malinowski, Gerbold C. Ménard, Sebastian Pauka, Hung Q. Nguyen, David M. T. van Zanten, Eoin C. T. O'Farrell, Judith Suter, Peter Krogstrup, Ferdinand Kuemmeth, Charles M. Marcus.
   Radio-Frequency Methods for Majorana-Based Quantum Devices:

Fast Charge Sensing and Phase-Diagram Mapping.
Phys. Rev. Appl., **11** (6), 064011 (2019).

5. Filip Krizek, Thomas Kanne, **Davydas Razmadze**, Erik Johnson, Jesper Nygård, Charles M. Marcus, Peter Krogstrup.
Growth of InAs wurtzite nanocrosses from hexagonal and cubic basis.
Nano Lett., **17** (10), 6090-6096 (2017).

1

INTRODUCTION TO SUPERCONDUCTIVITY

This chapter highlights some of the key phenomena of the widely studied theory of superconductivity since its first experimental discovery in 1911. First, the definition of normal and superconducting states is presented in the context of BCS theory followed by the description of Andreev reflection to explain the necessary techniques used for tunneling spectroscopy experiments. We continue with the introduction of the Josephson effect that is necessary to explain current-phase relationship in a superconducting quantum interferometer device. Josephson junctions with quantum-dots are introduced, where π-shift in current-phase relation can be observed by changing the dot parity. Finally, we present topological superconductivity in terms of Majorana fermions and discuss how it can be engineered in one dimensional condensed matter systems.

1.1 Phenomenon

At the turn of the 20th century, H. C. Onnes discovered that mercury (Hg) cooled below a certain temperature (T_c) become superconducting, meaning electrons that carry charge experience zero resistance [1]. The non-dissipative transport of electrons as they propagate through the superconductor, interact with lattice atoms causing net attractions of the free electrons, which leads to bound pairs called *Cooper pairs* with a charge of $2e$, where e is the elementary electron charge. Fig, 1.1 depicts a superconductor phase diagram with charge dynamics.
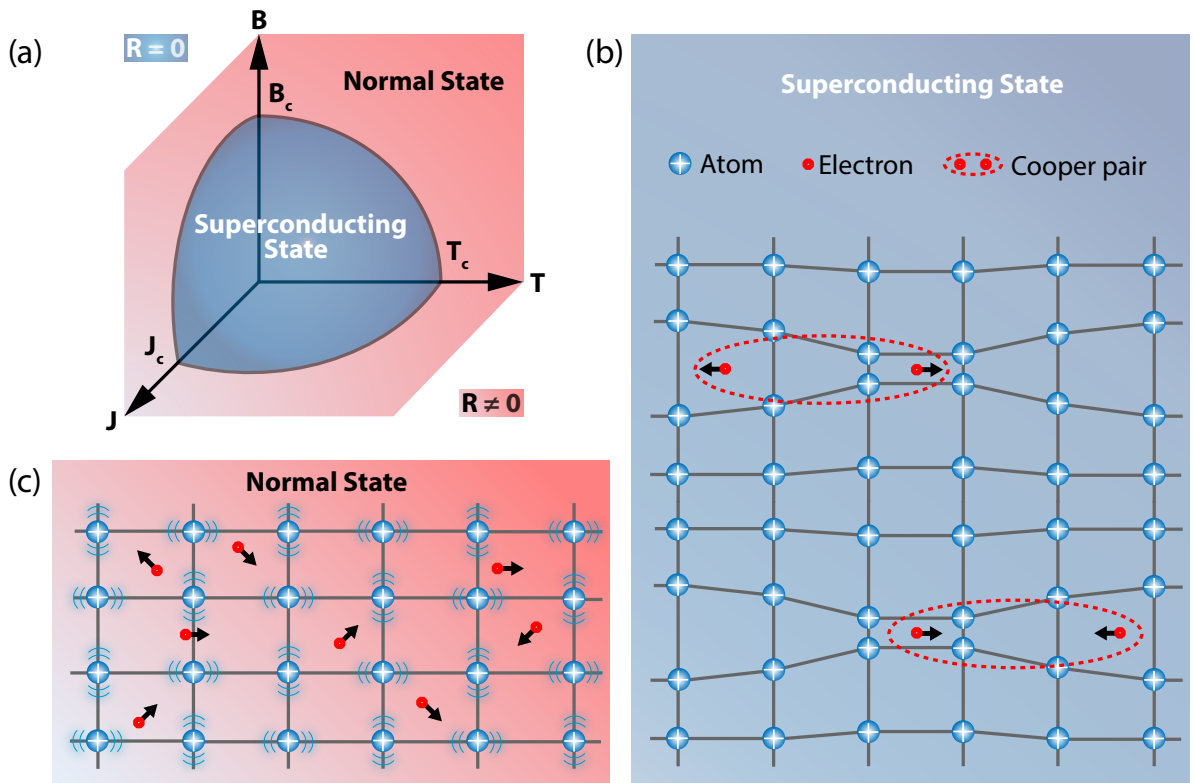
Figure 1.1: Phase diagram of normal and superconducting states. (a) A representative sketch of normal-superconducting phase boundaries as a function of temperature (T), external magnetic field (B), and current density (J). Boundaries of T_c, B_c, and J_c define critical values of all three parameters between superconducting (resistance R=0) and normal (resistance R≠0) phases. (b) In the superconducting state, electrons paired up to form Cooper pairs moving in an almost motionless lattice of well-defined atoms. The Cooper pair condensate energy is minimized when opposite momenta electrons are paired up. (c) The normal state, where atoms have enough energy to break up the Cooper pairs, leading to dissipative electron motion.

1.2 Normal state

The so-called Fermi-gas in the normal state [see Fig. 1.1(c)] of non-interacting electrons or fermions are filled up in its ground state to the Fermi energy E_F determined by the total number of electrons [2,3]. We define particles in momentum state $\mathbf{p}$ with the corresponding energy $E_F = E_{\mathbf{p}}$ defines the Fermi surface in momentum space p_F. Exciting an electron above E_F will increase the total energy of the system compared to the ground state. This leaves a *hole* excitation below the Fermi energy and can be view by two simultaneous processes: first, an electron with momentum p' and energy E' is moved to the Fermi energy E_F by $E_{-\mathbf{p}'} = E_F - E'$ and can be viewed as *hole* excitation with opposite momenta $-p_v$ of an electron; second, *particle* added above the Fermi energy by $E_{\mathbf{p}} = E - E_F$ with the same momenta p_u as an electron. Excitation spectrum will be defined as:

$$
E_p = \begin{cases} \frac{p^2}{2m} - E_F, & p > p_F \ (\textit{particle excitation}) \\ E_F - \frac{p^2}{2m}, & p' < p_F \ (\textit{hole excitation}) \end{cases} \tag{1.1}
$$

We will define the quasi-particle state with a wave vector $\mathbf{k} = \mathbf{p}/\hbar$. It is useful to double the degrees of freedom to describe superconductivity for quasi-particles as spontaneous symmetry breaking, where single-particle Hamiltonian is described by [4]:

$$
H(\mathbf{r}) = \frac{-\hbar^2}{2m} \partial_{\mathbf{r}}^2 - \mu_c, \tag{1.2}
$$

with $\hbar$ and m being reduced Planck's constant and effective particle/hole mass, respectively. Chemical potential is defined as μ_c and $\partial_{\mathbf{r}}$ is the partial derivative with respect to spatial coordinate $\mathbf{r}$. Then the single quasi-particle spectrum can be calculated by solving the Schrödinger equation with plane wave approximation for free particles with corresponding eigenvalues:

$$
E = \begin{cases} \left(\frac{\hbar^2 p^2}{2m} - \mu_c \right), & (\textit{particle excitation}) \\ -\left(\frac{\hbar^2 p^2}{2m} - \mu_c \right), & (\textit{hole excitation}) \end{cases} \tag{1.3}
$$

3
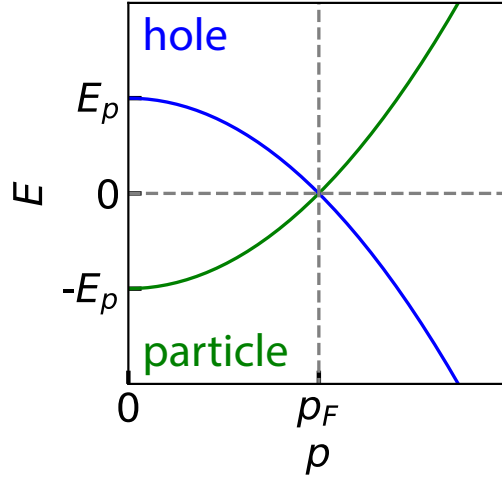
Figure 1.2: Single quasi-particle spectrum for the normal state for particles (green) and holes (blue).

We can plot the energy spectrum for quasi-particles close to the Fermi surface in Fig. 1.2(a).

1.3   BCS model

The microscopic superconducting dynamics were explained by Bardeen-Cooper-Schrieffer (BCS) theory model. Other superconducting aspects such as electrodynamic properties were described by London theory [5], and Ginzburg-Landau theory described superconductivity on a phenomenological level. Leon Cooper in 1956 noticed that in the presence of a filled Fermi sphere, the two-particle interactions can give rise to a bound state [6]. The pairing interaction Hamiltonian of a system can be written:

$$H = \sum_{\mathbf{k}\sigma} \xi_{\mathbf{k}} c^{\dagger}_{\mathbf{k}\sigma} c_{\mathbf{k}\sigma} + \sum_{\mathbf{k}\mathbf{k}'} V_{\mathbf{k}\mathbf{k}'} c^{\dagger}_{\mathbf{k}\uparrow} c^{\dagger}_{-\mathbf{k}\downarrow} c_{-\mathbf{k}'\downarrow} c_{\mathbf{k}'\uparrow}, \tag{1.4}$$

where $\sigma = \uparrow, \downarrow$ defines the particle/hole spin, $c^{\dagger}_{k}$ and c_{k} is the creation and annihilation of single quasi-particle with momentum k and spin σ. The first term of the summation describes the kinetic energy of the system with $\xi_{\mathbf{k}} = \frac{\hbar^2 p^2}{2m} - \mu_c$, whereas the second term summation describes the pairing potential between the *particles/holes* with different spin and

momenta. Using mean-field approximation the pairing amplitude can be defined as:

$$\Delta_{\mathbf{k}} = \sum_{\mathbf{k}'} V_{\mathbf{k}\mathbf{k}'} c_{-\mathbf{k}'\downarrow} c_{\mathbf{k}'\uparrow}, \quad \Delta_{\mathbf{k}}^* = \sum_{\mathbf{k}'} V_{\mathbf{k}\mathbf{k}'} c_{\mathbf{k}'\uparrow}^\dagger c_{-\mathbf{k}'\downarrow}^\dagger \tag{1.5}$$

The Hamiltonian for the new type of quasi-particles, called Bogolubov quasi-particles can be written as [7]:

$$H_{BdG} = \sum_{\mathbf{k}} \Psi_{\mathbf{k}}^\dagger \mathcal{H} \Psi_{\mathbf{k}}, \quad \mathcal{H} = \begin{pmatrix} \xi_{k\uparrow} & \Delta_k \Delta_k^* & -\xi_{k\downarrow} \end{pmatrix} \tag{1.6}$$

where Ψ_k is the spinor field matrix. For homogeneous superconductors, the $\Delta_k = \Delta$ and is called pairing amplitude or the superconducting energy gap that is needed to break up the Cooper pair. Plane-wave Schrödinger equation solution eigenvalues of Bogolubov de Gennes Hamiltonian H_{BdG}:

$$E = \begin{cases} \sqrt{\xi_k^2 + |\Delta|^2}, & (particle\ excitation) \\ -\sqrt{\xi_k^2 + |\Delta|^2}, & (hole\ excitation) \end{cases} \tag{1.7}$$

The single-particle energy dispersion relation is gapped for $|\Delta|$ values [Fig. 1.3].

Single quasi-particle excitation probabilities u_0 and v_0, satisfies normalizing condition, $u_0^2 + v_0^2 = 1$. Combination of plane-wave Schrödinger equation of H_{BdG} and 1.7 yields the particle/hole probabilities, which are defined [8]:

$$u_0^2 = \frac{1}{2} \left(1 + \frac{\sqrt{E^2 - |\Delta|^2}}{E} \right) \quad \text{and} \quad v_0^2 = 1 - u_0^2 \tag{1.8}$$
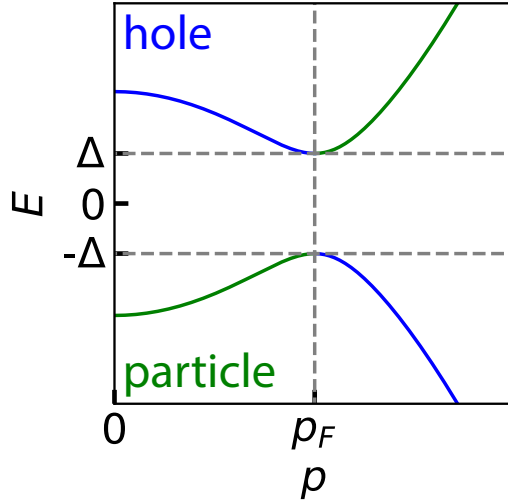
Figure 1.3: Single quasi-particle spectrum for the normal state for particles and holes. At momentum, p_F, particle/hole mixture takes place, therefore the is no difference between them.
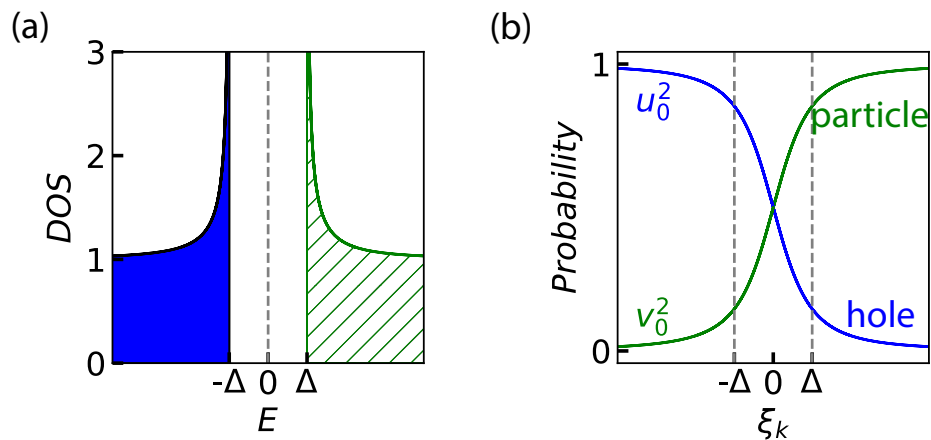
Figure 1.4: Single quasi-particle density of states with particle/hole probability spectrum. (a) Quasi-particle excitation density of states as a function of E for ref see Eq. 1.9. Particle/hole occupation indicated by filled up to -Δ by holes and empty states by particle excitation above Δ. (b) Probability of single quasi-particle excitation weights u_0^2 and v_0^2 as a function of ξ_k, see Eq. 1.8. Particle/hole mixing below the superconducting energy gap $|\Delta| < \xi_k$, indicates Cooper pair condensation region in energy space.

As seen in Fig. 1.4(b) both particle/hole weight probabilities are finite at around $\pm|\Delta|$. From Eq. 1.7, the density of states (DOS) can be deduced to the form:

$$DOS = \frac{N_S}{N_N} = \frac{E}{\sqrt{E^2 - |\Delta|^2}} \tag{1.9}$$

And is plotted in Fig. 1.4(a), with a quasi-particle density of states (particle/hole), are filled up to $\pm\Delta$ values, where it diverges. Single quasi-particle states are fully gapped by the pairing potential $|\Delta|$.

1.4 Tunneling spectroscopy

The charge transfer in the normal-superconducting (NS) interface can be view by the following mechanism. Consider an incident electron in the normal metal with momentum $k_\uparrow$ and energy $E_{electron}=E_F$ is traveling to the NS interface shown in Fig. 1.5(a)-(b), then the incident electron wavefunction can be written as:

$$\Psi_{Incident} = \begin{pmatrix} 1 \\ 0 \end{pmatrix} e^{i\mathbf{k}_\uparrow \mathbf{x}} \tag{1.10}$$

The Fermi energy will be aligned for both normal and superconducting regions, and within the superconductor only available quasi-particle (single electron or hole) states are at $E > |\Delta|$, meaning the incident electron will undergo a retroreflection if its energy is below $|\Delta|$, and its wavefunction is now written as:

$$\Psi_{Reflection} = a \begin{pmatrix} 0 \\ 1 \end{pmatrix} e^{i\mathbf{k}_\downarrow \mathbf{x}} + b \begin{pmatrix} 1 \\ 0 \end{pmatrix} e^{-i\mathbf{k}_\uparrow \mathbf{x}} \tag{1.11}$$

This will take place if the normal metal can donate an extra electron with opposite momenta to that of an incident electron, then the Cooper pair singlet $(k_\uparrow, -k_\downarrow)$ is formed that can enter and propagate through the

superconductor. With momentum conservation, normal metal Fermi sea is left with a hole opposite spin and momenta.
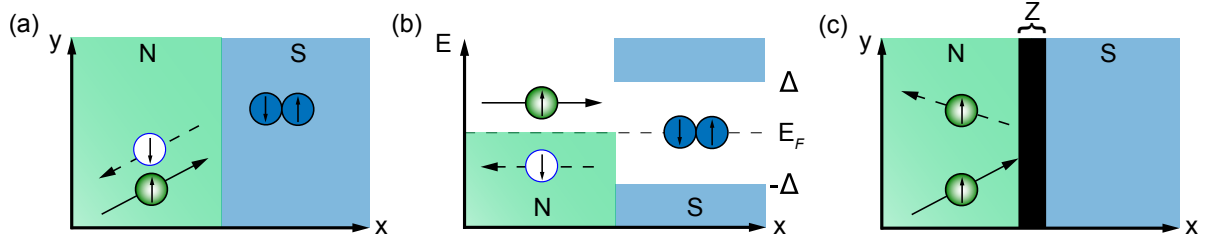
Figure 1.5: Andreev reflection process. (a) Real space representation of Andreev reflection. (b) Energy representation along the NS interface. (c) Normal reflection representation in real space at the NS interface with finite dimensionless Z barrier height.

Now if we introduce a finite energy barrier $Z = \sqrt{1/\tau - 1}$, where τ is transmission [see Fig. 1.5(c)], an electron can undergo a specular reflection whereas below the superconducting gap Δ electron is reflected and no Cooper pair is formed. If incident electron energy $E_{electron} > |\Delta|$, then electron propagation through the superconductor can be described by Eq. 1.12 as an electron/hole-like quasi-particles.

$$\Psi_{Transmission} = c \begin{pmatrix} u \\ v \end{pmatrix} e^{i\mathbf{k}_e \mathbf{x}} + d \begin{pmatrix} u \\ v \end{pmatrix} e^{-i\mathbf{k}_h \mathbf{x}} \tag{1.12}$$

From Eq. 1.11 - 1.12, probabilities coefficients for Andreev reflection $A = a^*a$ and specular reflection $B = b^*b$, as well as transmission probabilities for electron and hole-like particles $C = c^*c$ and $D = d^*d$, respectively. With probability conservation $A + B + C + D = 1$, each process can be written in Table 1.1 and shown in Fig. 1.6 for different dimensionless barrier Z values.

With finite voltage drop, V, across the normal-superconducting (NS) interface, transmission current can be expressed as an integral [10]:

$$I_{NS}(V) = \frac{G_N}{e} \int_{-\infty}^{+\infty} [f_\rightarrow(E) - f_\leftarrow(E)] dE, \tag{1.13}$$

where right moving distribution function, $f_\rightarrow$, that originates from the normal side, and left moving function distribution, $f_\leftarrow$, originating from

Probability	$E < \Delta$	$E > \Delta$
A	$\frac{\Delta^2}{[E^2+(\Delta^2+E^2(1+2Z^2)]^2}$	$\frac{\Delta^2}{\gamma^2}$
B	$1 - A$	$\frac{4Z^2(1+Z^2)(E^2-\Delta^2)}{\gamma^2}$
C	0	$\frac{2(1+Z^2)\sqrt{E^2-\Delta^2}(E+\sqrt{E^2-\Delta^2})}{\gamma^2}$
D	0	$\frac{2Z\sqrt{E^2-\Delta^2}E-\sqrt{E^2-\Delta^2})}{\gamma^2}$

Table 1.1: Reflection and transmission probability coefficients at the NS interface. Coefficient A defines Andreev reflection probability, while coefficient B defines normal (specular) reflection. Second column for incident electron below the superconducting gap Δ and third column is for energies above the gap. C and D coefficients define transmission into the superconductor with particle-like and hole like excitation. Here $\gamma^2 = (E + (1+2Z^2)\sqrt{E^2 - \Delta^2})^2$. Table was inspired by [9].

the superconducting reservoir.

$$f_\rightarrow(E) = f_0(E - eV) \tag{1.14}$$

$$f_\leftarrow(E) = A(E)[1 - f_\rightarrow(-E)] + B(E)f_\rightarrow(E) + [C(E) + D(E)]f_0(E) \tag{1.15}$$

Then Eq. 1.13 can be rewritten as:

$$I_{NS}(V) = \frac{G_N}{e} \int_{-\infty}^{+\infty} [f(E) - f(E - eV)][1 + A(E) - B(E)]dE \tag{1.16}$$

The second product term, [1 + A(E) - B(E)] is denoted as electron transmission coefficient through the interface [8] and noting that transport is dominated by normal and Andreev reflection process we can study them for different values of the dimensionless barrier, Z, in Fig. 1.6.

If we take the derivative of Eq. 1.16 in respect of voltage, we will get differential conductance, dI/dV:

$$G(V) = \frac{dI}{dV} = G_0[1 + A(eV) - B(eV)], \tag{1.17}$$
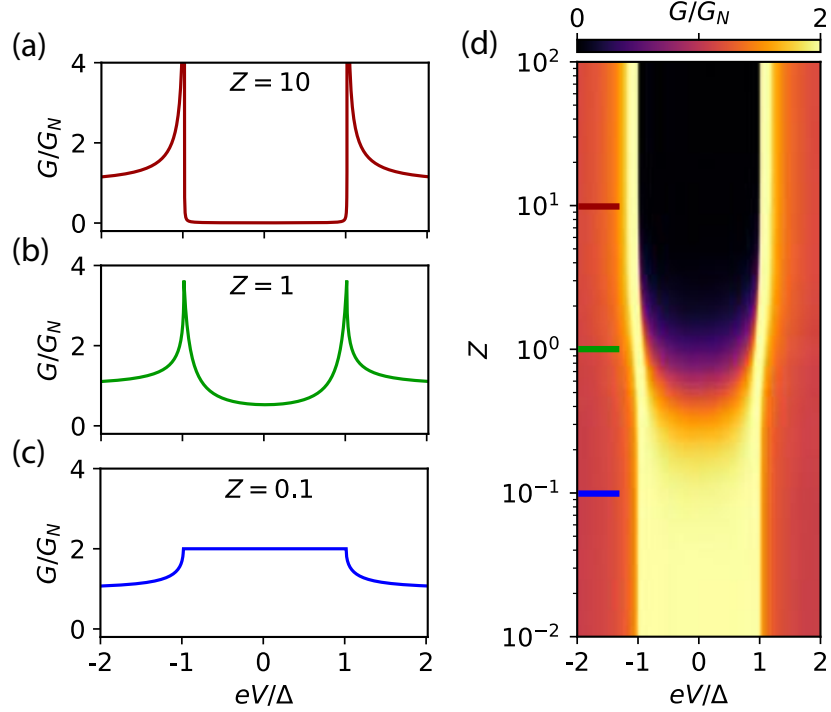
Figure 1.6: Andreev and normal reflections for different barrier, Z, values. (a) Differential conductance, dI/dV, of density of states with fixed barrier height of $Z = 10$, indicating suppressed quasiparticle transmission below the superconducting gap, Δ. (b) The same as (a) only for $Z = 1$, indicating finite quasiparticle spectrum below $|\Delta|$. (c) same as (a)-(b) only for $Z = 0.1$ maximum quasiparticle transmission into the superconductor. (d) Full differential conductance, dependence for different barrier, Z, values (plotted using Eq. 1.17). Figure was inspired by Ref [9].

with energy, E, expressed in units of eV. If we normalize to normal state conductance, $G_N = G_0/(1 - Z^2)$ for $E = eV > |\Delta|$, we will get the Blonder-Tinkham-Klapwijk expression for measured density of states in the superconductor [8]:

$$DOS \equiv \frac{dI}{dV} = G/G_N = \frac{E}{\sqrt{E^2 - |\Delta|^2}} \tag{1.18}$$

1.5 Josephson effect

In the 1960s Josephson predicted that Cooper pairs could tunnel between two superconductors separated by a thin insulating region, preserving coherence [11]. Followed by a series of experimental confir-

mation of such phenomena [12], with natural formed Al/AlO$_2$ barriers showed a perfect solution in creating high-quality tunnel junctions [13].

1.5.1 Cooper pair wavefunction

Since Cooper pairs are charge carriers of supercurrent in superconducting junctions we first describe their wavefunction.

An electron is known as a *fermion*, a combination of two electrons or a pair - *boson*. Just like other elementary particles such as photons, bosons like to occupy the lowest and exact energy state. Therefore, it costs more energy to move them in another state and so they tend to move together within a single state. We can define Cooper pair wavefunction in the ground state as [4]:

$$\psi(\mathbf{r}, t) = \rho^{1/2} e^{i\varphi(\mathbf{r},t)}, \tag{1.19}$$

where ρ is the current density and it is proportional to $P = \psi\psi^*$ is the probability density, with φ given as the global phase of the entire superconductor. All three parameters are real functions and can be experimentally observed. We know that the Schrödinger equation of a moving free particle in a magnetic field can be written:

$$\frac{-\hbar}{i} \frac{\partial \psi}{\partial t} = \frac{1}{2m} \left(\frac{\hbar}{i} \partial_r - q\mathbf{A} \right)^2 \psi + E_{pot}\psi, \tag{1.20}$$

where $\mathbf{A}$ is the vector potential, q - charge of Cooper pairs i.e. $2e$, with e as elementary electron charge, and the last term describes the potential energy of the particle.

Since the probability density is locally conserved we can write down that the current satisfies:

$$\frac{\partial P}{\partial t} = -\partial_r \cdot \mathbf{J} \tag{1.21}$$

From Eq.1.20 it can be shown that:

$$\frac{\partial P}{\partial t} = -\partial_r \left[\frac{1}{2m} \psi^* \left(\frac{\hbar}{i} \partial_r - q\mathbf{A} \right) \psi + \frac{1}{2m} \psi \left(-\frac{\hbar}{i} \partial_r - q\mathbf{A} \right) \psi^* \right] \tag{1.22}$$

11

Taken into account Eqs. 1.19 and 1.22 one can deduce the current density to:

$$\mathbf{J} = \frac{\hbar}{m} \left(\partial_r \varphi - q\mathbf{A} \right) \rho \qquad (1.23)$$

There will exist a finite supercurrent when there is a phase gradient, φ. One way to introduce a phase drop in a superconductor is to have a tunnel junction to break the single-valued phase of the superconductor.

Josephson concluded that current density is simply a function of the phase difference:

$$I(\phi) = I_c sin(\phi), \qquad (1.24)$$

where I_c is the critical current, which defines maximum bias current through the tunnel junction before it turns to a normal state. Current-phase relation (CPR) could take a more general form with higher harmonics:

$$I(\phi) = \left[\sum_{n \geq 1} I_n sin(n\phi) + J_n cos(n\phi) \right] \qquad (1.25)$$

In the presence of time-reversal symmetry, odd integer, J_n vanishes and giving sinusoidal current-phase relationship. As we will see later for highly transparent junctions CPR will become highly non-sinusoidal.

1.5.2 *Andreev bound states*

Here we will show how this current is transferred via so-called bound states as a function of the phase difference.

Consider a normal region (semiconducting, normal metal or insulating material) that is sandwiched between two superconductors with the same energy gap Δ but with different superconducting phase, φ_L and φ_R as shown in Fig. 1.7(a). Superconducting-normal-superconducting

(SNS) junction, energy gap potential, Δ, takes a step-like function profile:

$$\Delta(x) = \begin{cases} \Delta e^{i\varphi_L}, & for\ x < 0 \\ 0, & for\ 0 < x < L \\ \Delta e^{i\varphi_R}, & for\ x > L \end{cases} \tag{1.26}$$

Now if we imagine an electron in the normal region with $E < |\Delta|$, traveling to the NIS interface on the right, will experience Andreev reflection, where a hole is retro reflected, propagating backward through the normal region. This hole will experience the reverse process, where an electron is retro reflected once hitting another NIS interface on the left. This continuous reflection will give rise to discrete energy states for quasi-particles called *Andreev bound states* (ABS).

To be more explicit, we consider right ($\Psi_{\rightarrow}$) and left ($\Psi_{\leftarrow}$) moving wavefunctions for electrons ($p = +1$) and holes ($p = -1$), respectively, and write down them compactly throughout the SNS junction [14]:

$$\Psi_p = \begin{cases} A_p \begin{pmatrix} v_0 e^{-i\varphi_L} \\ u_0 \end{pmatrix} e^{ip\tilde{k}_{-p}x}, & for\ x < 0 \\ B_p \begin{pmatrix} v_0 e^{-i\varphi_L} \\ 0 \end{pmatrix} e^{ipk_e x} + B_p \begin{pmatrix} 0 \\ u_0 \end{pmatrix} e^{ipk_h x}, & for\ 0 < x < L \\ C_p \begin{pmatrix} v_0 e^{-i\varphi_R} \\ 0 \end{pmatrix} e^{ip\tilde{k}_p(x-L)}, & for\ x > L \end{cases} \tag{1.27}$$

Energy eigenvalue of this system, for perfect transmission, ($\tau = 1$), yields:

$$\left(\frac{E}{\Delta}\right)\left(\frac{L}{\xi_0}\right) = 2arccos\left(\frac{E}{\Delta}\right) \pm \phi + 2\pi n, \ where\ n = 0, 1, 2... \tag{1.28}$$

With $\phi = \varphi_R - \varphi_L$ the phase difference across the junction. In the short SNS junction limit where superconducting coherence length,
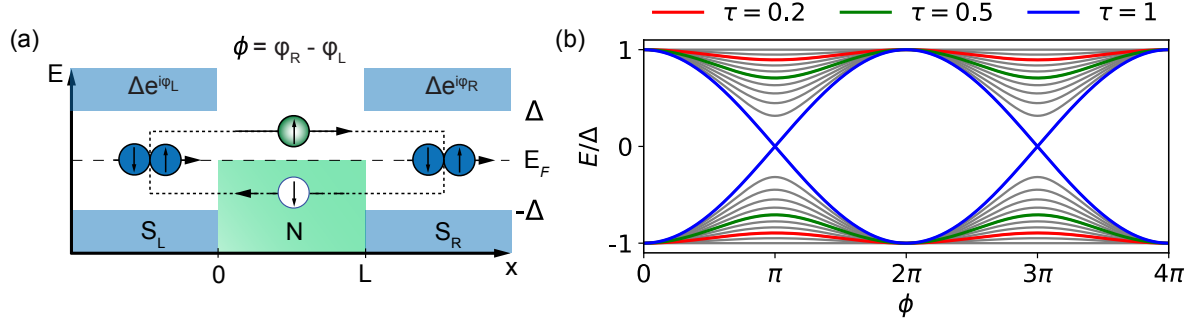
Figure 1.7: Andreev bound states in SNS junctions. (a) SNS junction with continuous Andreev reflection from SN interface in the normal region L. Left and right superconductors with the same energy gap, Δ, but with different phases, φ_L and φ_R. Calculated ABS ground state energy for different transmission coefficients, τ, using Eq. 1.30

$\xi_0 = E_F/k_f\Delta$ is much smaller than the normal region length, $L \ll \xi_0$, left-hand side of Eq. 1.28 reduces to:

$$E_{ABS} = \pm\Delta cos\left(\frac{\phi}{2}\right)$$ (1.29)

So far we assumed a perfect transmission through the SNS junction. For dirty junctions with impurities, scattering will reduce the transmission coefficient and now the ABS energy can be calculated by the following:

$$E_{ABS} = \pm\Delta\sqrt{1 - sin^2\left(\frac{\phi}{2}\right)\tau}$$ (1.30)

The ABS ground state energy is plotted in Fig. 1.7(b) for different transmission, τ coefficients. For a perfect transmitting channel, ABS ground state is degenerate at a phase difference of π with $2\pi n$ periodicity.

1.5.3 Flux quantization

Up until now, we discussed superconductors as a single piece of material, however interesting phenomena arise when we have ring-shaped superconductor. If we apply an external magnetic field normal to this imaginary ring-shaped superconductor, the magnetic field will be expelled from the interior of the ring. If we turn off the external magnetic

field, some flux will be trapped inside the ring and the supercurrent will flow around the ring. The flux, Φ can't decrease inside the ring, because $\partial\Phi/\partial t$ must be equal to the line integral of **B** in the ring, which is zero in the superconductor. From London equations [5] we know that the supercurrent will flow on the surface ($1/\lambda$, where λ is the penetration depth).

Inside the superconductor, the current density is zero, then the Eq. 1.23 will be reduced to:

$$\hbar\partial_r\phi = q\mathbf{A} \qquad (1.31)$$

Taking a line integral around the ring in a closed curve, L, Eq. 1.31 will be:

$$\hbar \oint_L \partial_r\phi ds = q \oint_L \mathbf{A}ds \qquad (1.32)$$

And since a line integral of a closed-loop around **A** is equal to the magnetic field, **B**, flux $\oint_L \mathbf{A}ds = \Phi$, Eq. 1.32 reduces to:

$$\oint_L \partial_r\phi ds = \frac{q}{\hbar}\Phi, \qquad (1.33)$$

where ϕ is the phase difference $\int_1^2 \partial_r\phi ds = \varphi_1 - \varphi_2$ between two points in the superconductor. Previously we have stated that superconducting wavefunction, $\psi = \sqrt{\rho}e^{i\varphi}$, takes on single-value in a continuous piece of superconductors and in a ring-shaped superconductor following a fixed closed contour, L, phase difference, φ, will only take multiples of $2\pi n$. Finally our Eq. 1.33 can be written [4]:

$$2\pi n = \frac{q}{\hbar}\Phi \qquad (1.34)$$

So any trapped flux in the ring will be quantized and can be changed by an integer value, with an external magnetic field.

1.5.4 Phase control with flux

As we have seen in previous section, the Andreev bound states carry supercurrent through Josephson junctions, particularly by adjusting the
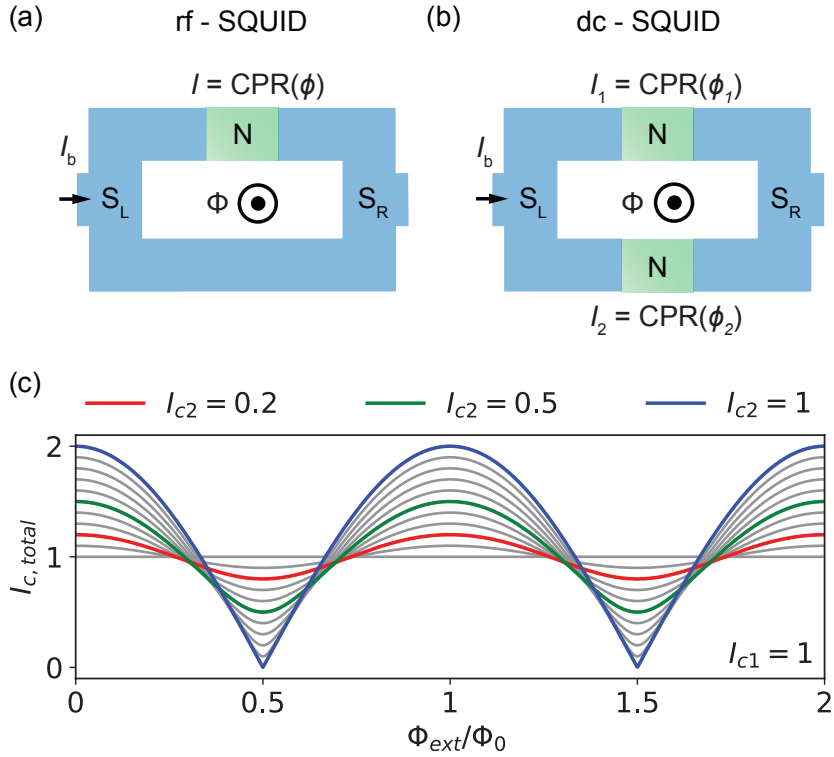
Figure 1.8: Phase biasing of Jospehson junctions embedded in superconducting loop. (a) rf - SQUID with single Josephson junction embedded into a superconducting loop with phase control using flux, Φ, (b) dc - SQUID consisting of two Josephson junctions in parallel embedded into a superconducting loop. (c) Total critical current as a function of applied flux through a dc - SQUID for different values of junction current, I_2 and fixed junction critical current, $I_1 = 1$.

superconducting phase difference, ϕ, one can change the magnitude of that current. However, changing the phase difference in SNS junctions with source and drain is not trivial.

It was shown that by embedding a Josephson junction into a superconducting loop, one can change the phase difference of a junction by applying an external magnetic field that threads a flux, Φ, through the loop [15,16]. This so-called Superconducting Quantum Interference Devices (SQUIDs) [17,18] can be viewed as interference devices for supercurrents, which is phenomenologically the same as a double-slit interference experiment [19], where the interference pattern position on the screen would be equivalent to the phase difference (tunable with the external magnetic field) and the two slits would represent the two Josephson junctions in parallel.

A single Josephson junction embedded into a superconducting loop is called an rf - SQUID [see Fig. 1.8(a)]. The circulating current sets flux quantization condition [20]:

$$\varphi + \Phi = 2\pi n, \quad \Phi = \frac{2\pi}{\Phi_0}\Phi_{ext} \tag{1.35}$$

where $\Phi_0 = \frac{h}{2e}$ is the flux quantum and $\Phi_{ext} = B_\perp S$ is the applied external magnetic field through the loop. Applying an external field will induce some screening current, that means the total flux will be:

$$\Phi_{total} = \frac{2\pi}{\Phi_0}\Phi_{ext} - \Phi_{screen}, \tag{1.36}$$

where the screening flux is given by $\Phi_{screen} = \frac{2\pi}{\Phi_0}(L_g + L_k)I$, L_g and L_k being geometric and kinetic inductances of the loop. rf - SQUID are used to measure inductance using microwave signals via LC-tank circuits, where the resonant frequency is sensitive to loop inductance.

Having two Josephson junctions in parallel in a loop is called a dc - SQUID [1.8(b)]. Now the total measured current through the loop will be determined by the two junction critical currents, I_{c1} and I_{c2} with phase differences across the two junctions, ϕ_1 and ϕ_2, respectively. We can approximate that the superconducting loop geometric and kinetic inductance are negligible in interferometer devices investigated in this thesis.

Now the flux quantization will bare two phase differences of the two junctions:

$$\phi_1 - \phi_2 = \Phi_{total} + 2\pi n \tag{1.37}$$

The total current through the loop will be given by the sum of two supercurrents passing the two junctions, $I = CPR_1(\phi_1) + CPR_2(\phi_2)$. We can introduce an asymmetry coefficient, $a = (I_{c1} - I_{c2}) / (I_{c1} + I_{c2})$, that determines an asymmetry of critical currents between two junctions.

With some trigonometry tricks, the total critical current through the loop can be written [18]:

$$I_{c,total} = (I_{c1} + I_{c2})\sqrt{(1 - a^2)cos^2\left(\frac{\Phi_{tot}}{2}\right) + a^2} \qquad (1.38)$$

This total critical current is plotted in Fig. 1.8(c) for different values of I_{c2} while keeping fixed $I_{c1} = 1$.

1.6 Supercurrent reversal and π-junctions

In the previous section, we observed that critical current across the Josephson junction has a sinusoidal dependence. An interesting phenomenon can occur where the transferred current through the junction changes sign meaning there is a π phase offset in the current-phase-relation:

$$I = I_c \sin(\varphi + \pi) = -I_c \sin(\varphi) \qquad (1.39)$$

This implies a supercurrent reversal in SNS junctions, where supercurrent flows the opposite direction with respect to the applied phase difference.

The first theoretical proposal of a π-junction comes from Bulaevskii and colleagues [21] where magnetic impurities in the tunnel junctions were contributing to a reordering of Cooper pair singlet. They also argued that one could detect signatures of a π-junction in SQUID based geometry devices. More relevant to this thesis is that prediction of S-QD-S system, where Josephson junction hosts a quantum-dot could also give rise to spin-flip [22] leading to a π-junction as well as predicted by Refs [23, 24] and shown experimentally by [25–27].

One can also engineer a system to get supercurrent reversal is using ferromagnetic metal or insulator that forms an SNS junction. In the latter system due to the exchange interaction of the ferromagnetic material Cooper pair singlet degeneracy is lifted. As a consequence singlet tries to compensate this by acquiring finite kinetic energy which in turn leads to non-zero momentum as electron propagates and order parameter changes in space. This was argued by Larkin and Ovchinnikov [28] and by Fulde and Farrel [29], which is now called a LOFF state.

In an S-QD-S system, if sufficient charging energy is introduced, discrete energy levels arise in the QD. Including electron-electron interactions, one can write the whole system Hamiltonian in terms of the Anderson impurity model [30]:

$$H = H_L + H_R + H_T + H_{QD}, \tag{1.40}$$

where $H_T = \sum_{k\sigma,v}(V_{k\sigma,v}c_{k\sigma,v}^\dagger d_{0\sigma} + h.c.)$ and $H_{QD} = \sum_\sigma \epsilon_0 d_{0\sigma}^\dagger d_{0\sigma} + E_C n_{0\uparrow} n_{0\downarrow}$. Here electron spin σ creation operator is defined as $d_{0\sigma}^\dagger$ and number operator is defined as $n_{0\sigma} = d_{0\sigma}^\dagger d_{0\sigma}$. Left and right lead Hamiltonian takes the usual form introduced in Eq. 1.4. Solving Eq. 1.40 is difficult, therefore certain approximations are needed. Since electron-electron interaction in real systems plays a major role we approximate that on the single dot level it can accept just a single electron. Charging energy E_C imposes a constant electron number, whereas in the superconducting leads Cooper pair number can fluctuate. The rate at which electrons tunnel is given by tunneling rate $\Gamma = \Gamma_L + \Gamma_R$.

It is possible to categorize three distinct regimes based on three parameters: Γ, Δ, E_C:

First, the strong coupling regime, where $\Gamma \gg \Delta, E_C$ meaning dot couples well to the superconducting leads, electrons can tunnel through the dot. It can be viewed as an SNS junction with a perfect transmission.

Second, a weak coupling regime, where $\Gamma \ll \Delta, E_C$, no supercurrent is observed because large charging energy prohibits the transfer of Cooper pairs. Single electrons can tunnel through on a characteristic time scale of h/Γ which is much larger that of Cooper pair coherence time h/Δ.

Third, intermediate coupling regime, $\Gamma \sim \Delta \sim E_C$, here individual transfer of electrons does not prohibit to observe supercurrent since electrons recombine into a Cooper pair singlet via a fourth-order co-tunneling process.

Introducing the constant interacting model one can write down the new QD Hamiltonian:

$$\sum_\sigma = \epsilon_\sigma d_{0\sigma}^\dagger d_{0\sigma}, \tag{1.41}$$

where $\epsilon_\uparrow = \epsilon_0 - E_C/2$ and $\epsilon_\downarrow = \epsilon_0 + E_C/2$. Within this model one can find a global minimum of ground state at phase difference, $\varphi = 0$, for empty dot ($\epsilon_0 > 0$) what is known as a 0-junction. With the same reasoning, a π-junction is constructed by having singly occupied dot ($\epsilon_0 < 0$) the global minimum of the ground state is found at $\varphi = \pi$. Changing of the occupancy of the dot is can be viewed equivalently as changing the Zeeman field that transitions from 0-junction to π-junction. So simply put finding π shift in current-phase relation one has to adjust the energy level $\epsilon_0 = E_C/2$ in the odd number of Coulomb diamonds.

1.7 Topological superconductivity

The word *topology* comes from a mathematical description of shapes that can be continuously deformed without tearing. To give an example: a coffee mug and a doughnut are in the same topological class, meaning they can be mathematically deformed between one and the other. It was shown quantum Hall phenomena could be categorized as a topological system, where adiabatic continuity is mathematically viewed by an integer Chern number [31]. In 2005 theoretical discovery stated that quantum spin Hall insulator system had topologically invariant properties [32, 33].

1.7.1 Majorana fermions

The search for topological condensed matter in low dimensional systems lies within exotic quasi-particle excitations called *Majorana fermions*. In 1937 young Italian physicist Ettore Majorana took on the famous Paul A. M. Dirac wave equation [34] and showed that neutral fermionic particles which are their own anti-particles and have real wavefunction function solutions [35]. Ever since it was theorized that such particles could exist as fundamental particles, physicists searched in high energy particle accelerators with no conclusive evidence yet.

Fairly recently [37–39] it was shown that conventional superconductors could be used to engineer a system where Majorana fermions could be realized in condensed matter systems. Here we will introduce a toy model describing Majorana fermions in 1D that was first put forward by
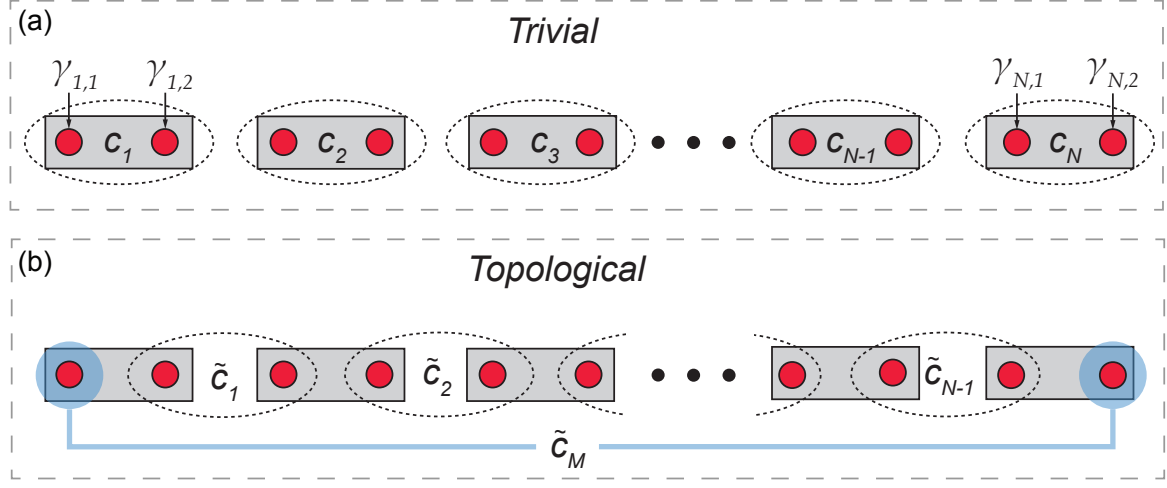
Figure 1.9: Phase biasing of Jospehson junctions embedded in superconducting loop. (a) Trivial case (*s-wave* pairing). (b) Topological case (*p-wave* pairing). Figure was inspired by [36]

A. Kitaev [40]. A spinless *p-wave* pairing superconductor Hamiltonian can be written:

$$H_{1D} = \sum_i^N \left[-\mu c_i^\dagger - t \left(c_i^\dagger c_{i+1} + c_i c_{i+1}^\dagger \right) + \Delta c_i c_{i+1} + \Delta^* c_i^\dagger c_{i+1}^\dagger \right], \quad (1.42)$$

where c_i and $c_i^\dagger$ is the particle annihilation and creation operator, respectively, for site i. Chemical potential is μ. We now can write down the Majorana operators as:

$$c_i = \frac{1}{2}(\gamma_{i,1} + i\gamma_{i,2}), \quad c_i^\dagger = \frac{1}{2}(\gamma_{i,1} - i\gamma_{i,2}) \quad (1.43)$$

By inverting Eq. 1.43 we get Majorana operators living on site i.

$$\gamma_{i,1} = c_i^\dagger + c_i, \quad \gamma_{i,2} = i(c_i^\dagger + c_i) \quad (1.44)$$

It is known that Majorana physics arises when $\mu = 0$ and $t = \Delta$. By inserting Eq. 1.43 the Hamiltonian in Eq. 1.42 reduces to:

$$H_{1D} = -it \sum_i^{N-1} \gamma_{i,2}\gamma_{i+1,1}, \quad (1.45)$$

21

Majorana operators are composed of electron and hole parts and satisfy the following relation:

$$\gamma_i = \gamma_i^\dagger, \quad \gamma_i^2 = 1 \tag{1.46}$$

With special fermion pairing of adjacent sites, it is possible to write the Majorana operators of neighboring sites, $\tilde{c}_i = (\gamma_{i+1,1} + i\gamma_{i,2})/2$. With this pairing in mind, our Hamiltonian 1.42 can be written:

$$H_{1D} = 2it \sum_{i}^{N-1} \tilde{c}_i^\dagger \tilde{c}_i, \tag{1.47}$$

Note that in Eq. 1.47 Majorana operators, $\gamma_{N,2}$ and $\gamma_{1,1}$ are missing, which shows the non-local nature of Majorana fermions that are living at the two ends of a 1D chain. In the trivial regime single fermionic state is combined within the same site, whereas in the topological regime fermionic state is combined by adjacent sites. The non-locality of outer Majoranas can be written in terms of creation and annihilation operators [also highlighted in Fig. 1.9 (b)]:

$$\tilde{c}_M^\dagger = \frac{1}{2}(\gamma_{1,1} - i\gamma_{N,2}) \quad and \quad \tilde{c}_M = \frac{1}{2}(\gamma_{1,1} + i\gamma_{N,2}) \tag{1.48}$$

1.7.2 *Ingredients for topological matter*

So far we assumed the *p*-wave pairing [41] in a 1D chain, however in reality such materials do not exist but they could be manufactured by combining several ingredients. The scope of this thesis deals with high g-factor and spin-orbit coupling InAs nanowires [42], combined with *s-wave* superconductor such as aluminum one can recreate an environment that mimics *p-wave* superconducting pairing.

We can write down Bogoliubov-de Genes equation for such nanowires:

$$H = \int \Psi^\dagger \mathcal{H}_{BdG} \Psi dx \tag{1.49}$$

where

$$\mathcal{H}_{BdG} = \left[\frac{p^2}{2m} - \mu(x)\right]\tau_y + \frac{\alpha_R}{\hbar}p\sigma_y\tau_y + g\mu_B\frac{B(x)}{2}\sigma_z + \Delta(x)\tau_z \quad (1.50)$$

With μ is the chemical potential, μ_B is the Bohr magneton, $\hbar$ is the reduced Plank constant, p is the momentum operator, τ and σ is the Pauli matrices operating on particle-hole and spin space, respectively. In Eq. 1.50, $\Psi^\dagger = (\psi_\downarrow^\dagger, \psi_\uparrow^\dagger, \psi_\uparrow, -\psi_\downarrow)$ is the Nambu spinor. Zeeman energy is defined, $E_Z = g\mu_B B(x)/2$. One can find the eigenenergies of Hamiltonian in Eq. 1.50:

$$E_\pm^2 = E_Z^2 + \xi_p^2 + \Delta^2 + \left(\frac{\alpha_R}{\hbar}p\right)^2 \pm 2\sqrt{E_Z^2\Delta^2 + E_Z^2\xi_p^2 + \left(\frac{\alpha_R}{\hbar}p\right)^2\xi_p^2} \quad (1.51)$$

Assuming no superconductivity ($\Delta = 0$) and zero magnetic field (Zeeman energy, $E_Z = 0$) in 1D nanowire with $\mu = 0$, energy dispersion is plotted in Fig. 1.10(a). Due to spin-orbit coupling, we have two shifted parabolas in momentum space, $\pm k_{SO} = \pm m\alpha_R/\hbar^2$ and in energy space by spin-orbit energy, $E_{SO} = m\alpha_R^2/2\hbar^2$. As the axial magnetic field is increased to the nanowire, effective Zeeman energy will open a $2E_Z$ gap at $k = 0$ as seen in Fig. 1.10(b) and with further increase in E_Z shown in Fig. 1.10(c). Spin and momentum is locked at $\mu = 0$ with finite $E_Z > 0$.

If now we introduce superconductivity into our system ($\Delta > 0$) this will open a gap in energy dispersion as shown in Fig. 1.10(d), with doubled energy bands from particle-hole symmetry as discussed in the previous section (Sec. 1.3). For finite Zeeman energies but $< \Delta$ the system is still in trivial phase, increasing E_Z energy gap at Fermi energy is reduced by $E^* = \Delta - E_Z$. When E_Z is equal to the superconducting gap, Δ, a full closure of the gap at $k = 0$ is seen in Fig. 1.10(e). Exceeding $E_Z > \Delta$ leads to energy band inversion and the topological phase is reached where now it is said topological gap is opened, $E_{topo} = 2(E_Z - \Delta)$, which is shown in Fig. 1.10(f). We can generalize the critical energy condition needed to reach the topological phase as:

$$E_{Z,c} = \sqrt{\mu^2 + \Delta^2} \quad (1.52)$$
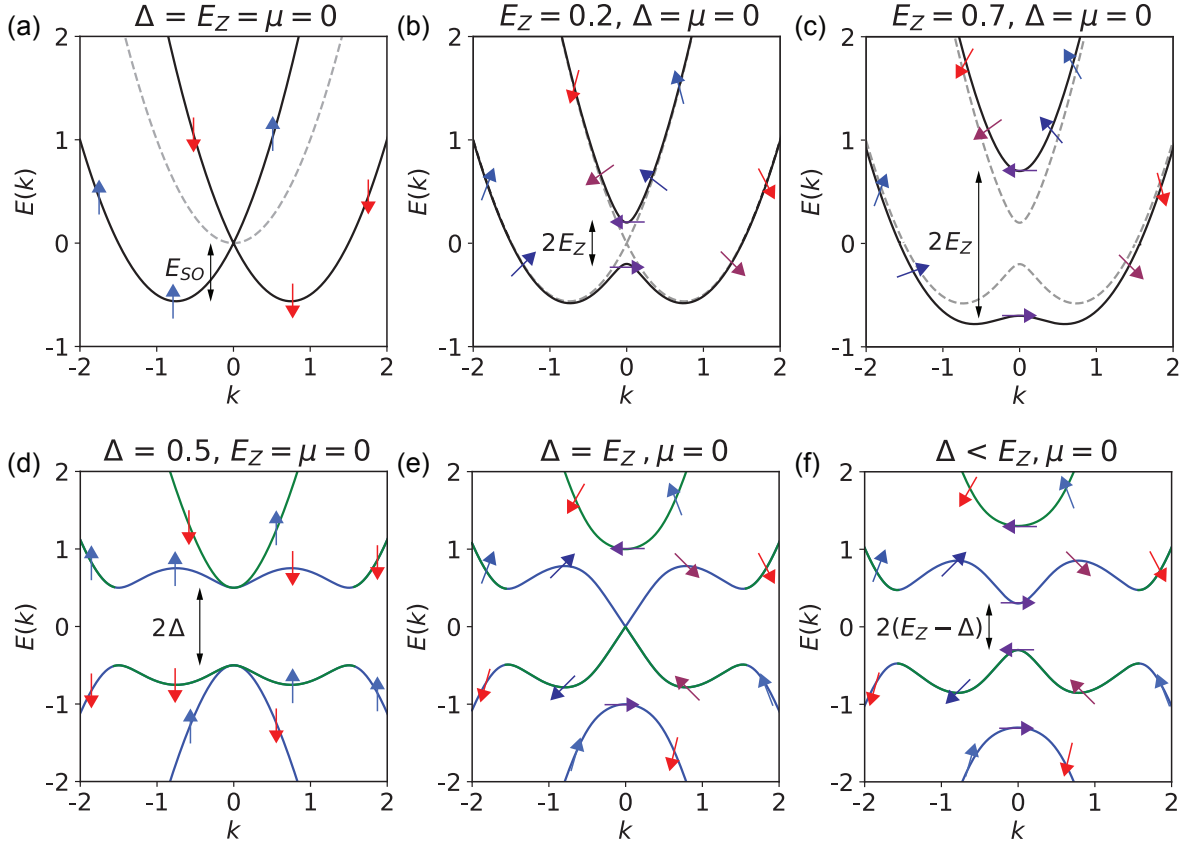
Figure 1.10: Energy dispersion of topological phase transition. (a) Without super-conductivity ($\Delta = 0$), split-bands due to spin orbit coupling ($E_{SO} > 0$). (b)-(c) Same as (a) but with introduction of axial magnetic field, which increases Zeeman energy, $E_Z = 0.2$ and $E_Z = 0.7$, respectively. (d) Introducing superconductivity ($\Delta = 0.5$) at $B = 0$, with Zeeman energy, $E_Z = 0$, where spin-split bands are coupled for particle and holes. (e) Increasing axial magnetic field, B, increases the Zeeman energy, at the transition point where $E_Z = \Delta$ energy dispersion band gap closes. (f) Further increasing magnetic field opens the topological gap of $2(E_Z - \Delta)$. For all the plots $\alpha = 1.5$ and $E_{SO} = m\alpha^2/2$. Figure was inspired by Ref [44].

We will now look qualitatively at the eigenvalues of Eq. 1.50 using tight-binding simulation software from Ref [43] for different Majorana wire lengths, $L_1 < L_2 < L_3$, with fixed Rashba coupling α_R. In Fig. 1.11(a)-(c) it is shown how the energy spectrum evolves as a function of E_Z, for different wire lengths. In all Fig. 1.11(a)-(c) it can be seen that the lowest energy bands oscillate as the Zeeman energy is increased, this is due to finite Majorana wavefunction overlap of the Majorana modes that are living at the boundaries of the nanowire. This energy oscillation can be suppressed by increasing the wire length dimension, L.
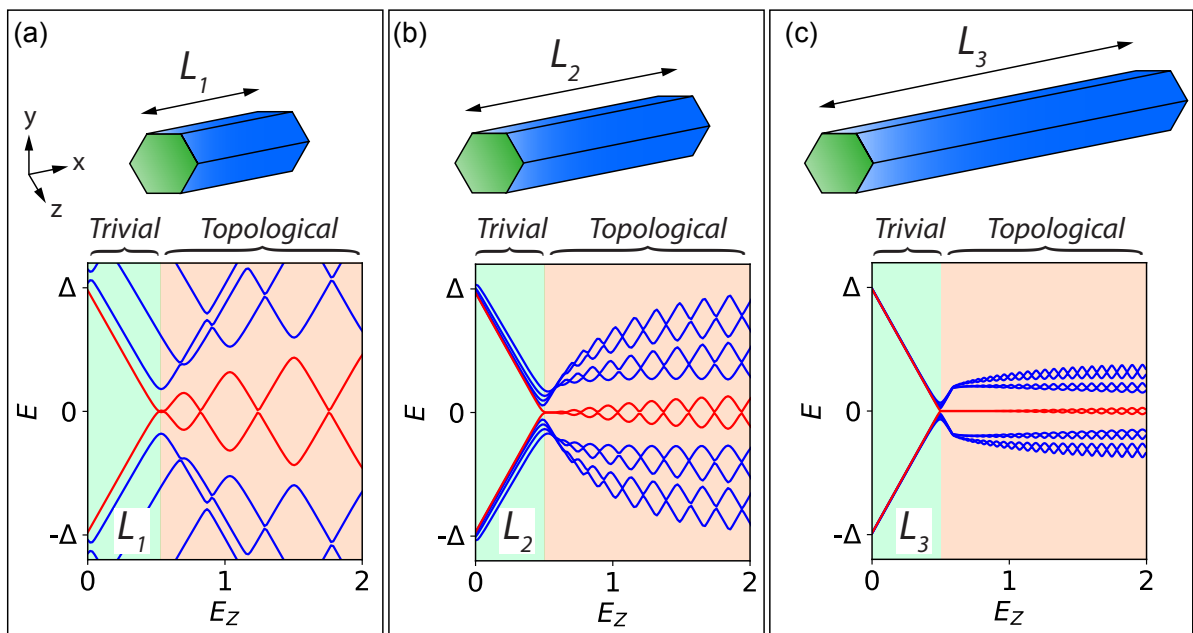
Figure 1.11: Topological length dependence in 1D wires ($L_1 < L_2 < L_3$). (a) Energy spectrum of finite L_1 length 1D topological wire as a function of increasing Zeeman energy, E_Z. Common ranges in all the figures is $0 < E_Z < \Delta$, where the wire is in the trivial regime and for $E_Z > \Delta$, the wire is in the topological regime. (b) Same as (a) except the 1D wire is longer $L_2 > L_1$. (c) Same as (b) but for even longer wire $L_3 > L_2$. All figures were produced using Ref [43] source code, with fixed α_R and chemical potential, μ.

2

FABRICATION AND EXPERIMENTAL TECHNIQUES

This chapter describes general steps that were used to create quantum devices and different measurement setups to gather experimental data. Firstly, the material used is the InAs nanowires with epitaxially grown aluminum is briefly described. Second, nanowire transfer from the growth substrate and to Si/SiO_2 blank chips using a micromanipulator tool is described. Followed by detailed steps used to fabricate different devices that are presented in the thesis, with specific fabrication recipes presented in Appendix A tables. Finally, the measurement setup and experimental techniques that were used to gather data are presented.

2.1 Super-semi nanowires

Materials that were investigated in this thesis are one-dimensional semiconductor crystals of InAs. First reports of such structures to be grown are from Wagner and Ellis [45], using the Vapor-Solid-Liquid growth technique, where catalyst nanoparticles (*e.g.* Au droplet) are deposited on the growth substrate (*e.g.* InAs wafer). Which is then placed in an ultra-high vacuum chamber of a molecular-beam-epitaxy system, in which the growth substrate is heated up and InAs precursor fluxes are opened. Once the melted nanoparticle droplets are supersaturated with introduced material fluxes, growth starts to take place normal to the wafer substrate, replicating the crystal orientation and structure of the substrate. After growth, single-crystalline nanowires structures are created as free-standing nanowires. [see Fig. 2.1].
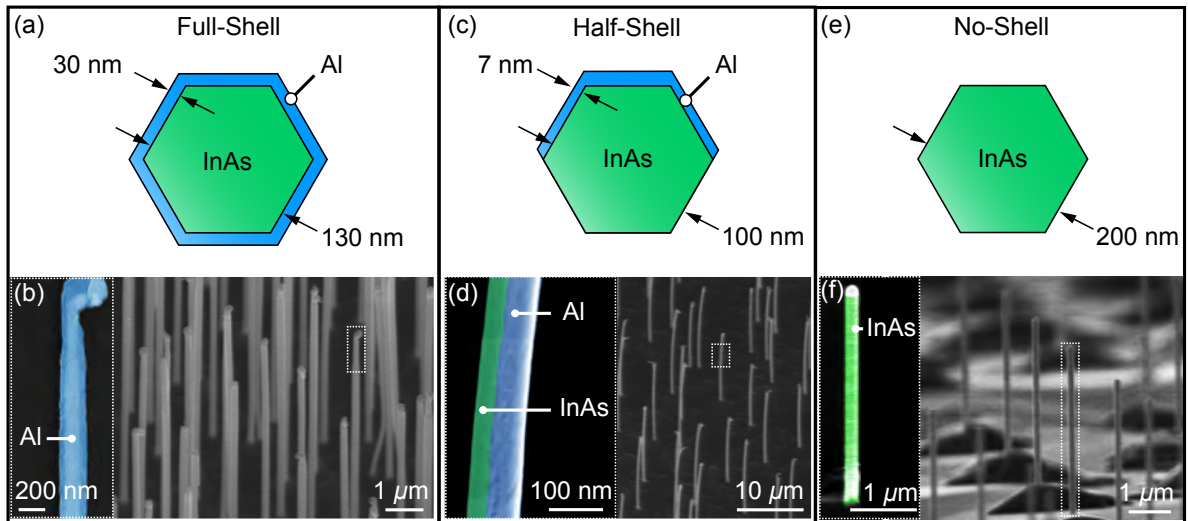
Figure 2.1: Investigated hybrid InAs/Al nanowires with cross-section illustration. (a) Full-shell Al surrounding the InAs core nanowire schematics, with dimensions. (b) False-color scanning electron micrographs with high and low magnification of fully surrounding Al the InAs nanowire core. (c) Half-shell Al covering three facets of the nanowire showing cross-section schematics with dimensions. (d) False-color scanning electron micrographs with high and low magnification of the three facet Al that covers InAs nanowire. (e) No-shell nanowires that were used as charge sensors cross-section schematics with dimensions. (f) False-color scanning electron micrographs with high and low magnification of bare InAs nanowires. Scanning electron micrographs, courtesy of Peter Krogstrup.

Recent advances have improved the quality of nanowires, but more specifically the epitaxial growth of superconductors such as Al [46] and Ta, Nb, and V [47] on InAs nanowires. With *in-situ* Al growth, the quality of the interface has dramatically improved, and the induced superconductivity properties due to the proximity effect. Tunneling spectroscopy suggests a hard superconducting gap, compared to *ex-situ* deposited superconductor. This indicates free of conventional quasi-particles below the superconducting energy gap Δ [48].

2.2 Micromanipulation

After nanowire growth, there are different approaches of transfer-ring them onto so-called blank Si/SiO_2 with degenerately n-doped Si substrate chips with pre-defined Au bonding pads and alignment marks. The most widely used nanowire transfer technique is dry de-position, using a cleanroom wipe, brushing over the nanowire growth substrate, and then immediately casting the nanowires onto the blank chip. This technique requires some precision but the transfer is fast compared to the technique that was used in this thesis. Though the nanowire transfer is fast, it has some downsides – there could be mul-tiple nanowires with a small separation between them, which would make device fabrication unnecessary challenging. Second, there is no selectivity in choosing nanowires and it can take some time to post-select the ones that look reasonable to fabricate devices, under opti-cal/scanning electron microscope. Finally, damages that the cleanroom wipe potentially does to the nanowires could influence the electrical performance during the measurement stage (not investigated in this thesis). The blank-chip oxide SiO_2 thickness is 200 nm. A blank chip DesignCad sketch is presented in Fig. 2.2(a) inset.

Considered all the above potential problems, the micromanipulator tool was used for presumably safer and more precise nanowire transfer from the growth substrate to the blank chip. The micromanipulator tool is equipped with a joystick movable stage, where the growth substrate and blank chip are placed, with x-y-z axis rotational axis. The transfer is accomplished with a spatially adjustable disposable needle (0.1 μm in diameter). The stage is also equipped with a large working distance optical microscope, for the needle to have access under the microscope.

Individual nanowires are inspected under the optical microscope and picked up with the needle and transferred with high spatial and angle precision onto the blank-chip with alignment marks.

2.3   Fabrication

Nanowire interferometer device fabrication is described in detail. Also, during each step, fabrication recipes are referenced in Appendix A.

A complete interferometer device fabrication flow is presented in Fig. 2.2. Blank chip sketch and optical microscope image with full-shell nanowires deposited are presented in Fig. 2.2(a). Selective full-shell Al etching is shown in 2.2(b), with an inset displaying etched Al region [see also Tables A.1 – A.3]. Polymer e-beam resist ramp structure formation and cross-link fabrication are presented in Fig. 2.2(c), with inset showing the final ramp structure [see Table A.4 and Fig. A.1]. Leaded Al loops deposition is shown in Fig. 2.2(d), with inset showing dark ramp structure and selectively etched regions [see Table A.5]. Local atomic layer deposition (HfO_2 = 7 nm) is followed next, covering the nanowire and is shown in Fig. 2.2(e) [see Table A.6]. Top-gates (Ti/Au = 5 nm/200 nm) are deposited on the etched regions of the nanowire in Fig. 2.2(f) [see Table A.7]. False-color scanning electron micrograph of the finished interferometer device is shown in Fig. 2.2(g).
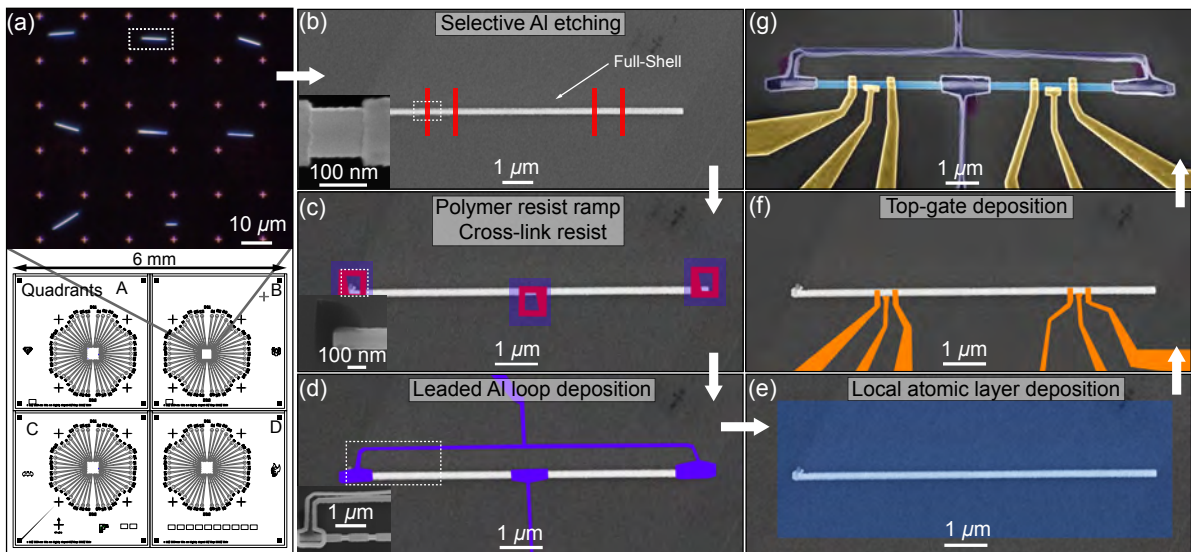
Figure 2.2: Full-shell nanowire interferometer device fabrication flow. (a) Blank chip sketch and optical microscope image of one out of four quadrants with micromanipulated nanowires. (b) Scanning-electron micrograph of a nanowire, with defined selective etching regions in red. (c) Rectangular frame exposure for polymer resist ramp structure in red, followed by cross-link exposure of the resist ramp in transparent blue rectangle. (d) Leaded Al loop structure deposition on the full-shell nanowire, with inset showing etched regions and dark cross-linked resist ramp for Al loop leads. (e) Local atomic layer deposition covering the full-shell nanowire. (f) Ti/Au top-gate deposition covering the etched regions and formed Al islands. (g) Scanning-electron micrograph of finished interferometer device.

Other structured nanowire devices were investigated, specifically to demonstrate capacitive coupled charge sensors with nearby nanowires, as well as gate-dispersive sensing readout. For that, slightly different fabrication steps were employed compared to full-shell nanowire interferometers, though some steps are repeated and referenced accordingly in Appendix A

The transfer of nanowires from the growth substrate to blank-chips are identical to previous device fabrication of full-shell nanowire devices. Except for nanowire charge sensors, two wires placed near the long wire ($\sim$1 μm apart) [see Fig. 2.3 (a)]. A long half-shell nanowire was intended as the main device, whereas two shorter no-shell nanowires from different growth batch were intended as charge sensors.

Half-shell Al nanowires were selectively etched in a slightly different fabrication sequence and materials that are presented in Table A.8, also see Fig. 2.3(b). Device lead fabrication is identical to full-shell interferometers (Table A.5) [see also Fig. 2.3(c)], with an exception of material used which is 5 nm of Ti – acting as a sticking layer, followed by Au leads with 180 nm thickness. Atomic layer deposition is the same fabrication procedure as for full-shell nanowire devices (Table A.6)[see Fig. 2.3(d)]Finally, top-gate deposition and charge sensor coupler between the main device (long wire) and charge sensor nanowires are patterned using as previous fabrication steps on full-shell interferometers (Table A.7)[see also Fig. 2.3(e)].
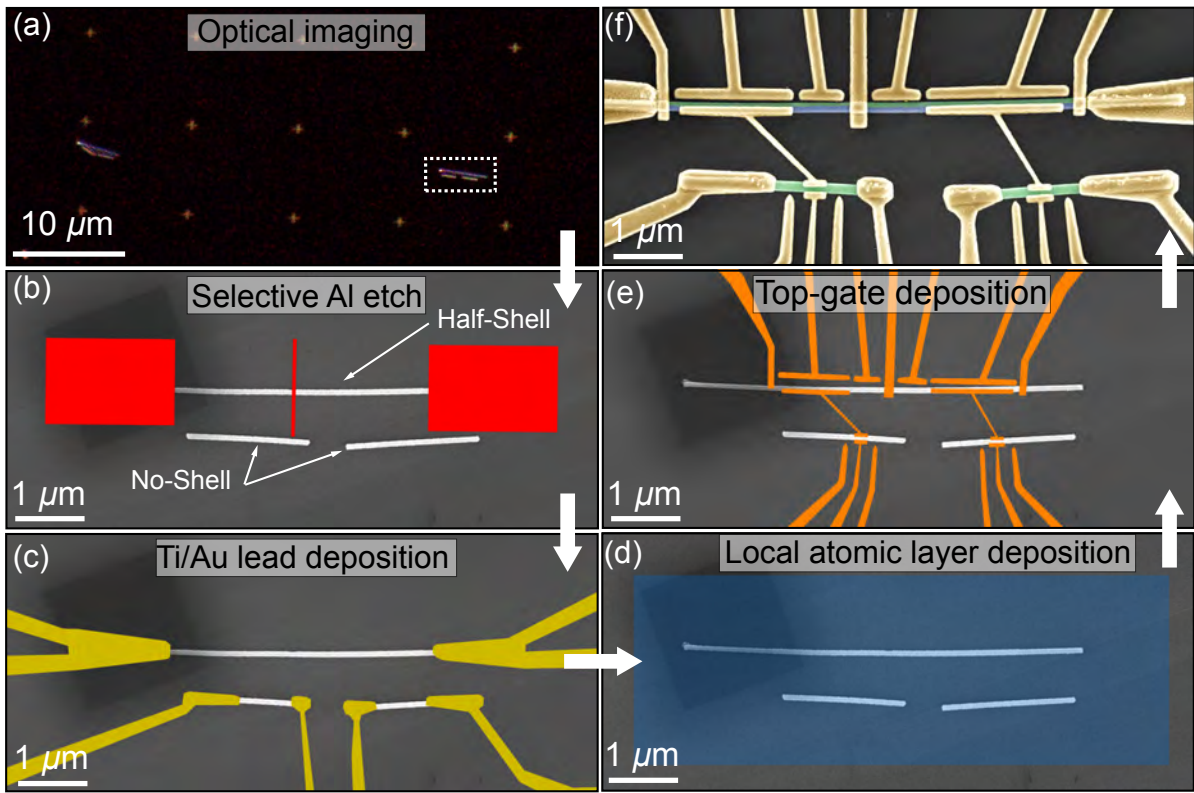
Figure 2.3: Half-shell nanowire device with external nanowire charge sensors fabrication flow. (a) Scanning-electron micrograph of micromanipulated two different nanowires (Main device – half-shell Al nanowire and charge sensor – no-shell Al nanowires), with selective etching regions on the half-shell nanowires. (b) Ti/Au leads for main device and charge sensors. (d) Local atomic layer deposition covering both half-shell nanaowire and no-shell nanowires. (e) Ti/Au top-gate deposition with floating couplers between main device and charge sensors. (d) Finished double-island Al nanowire device with two external charge sensor nanowires coupled by floating Ti/Au metallic couplers.

2.4 Bonding and loading

Devices are bonded to the in-house built daughterboard shown in Fig. 2.4, with cleaved blank-chips glue with silver paste to make good electrical contact between the daughterboard cavity and the Si/SiO$_2$ Au plated back-gate. Full-shell interferometer devices were investigated using standard low-frequency lock-in techniques, meaning no resonant circuit was used and only dc lines were bonded [Fig. 2.4(a)]. Half-shell charge and dispersive sensing devices, on the other hand were investigated using both low/high-frequency reflectometry
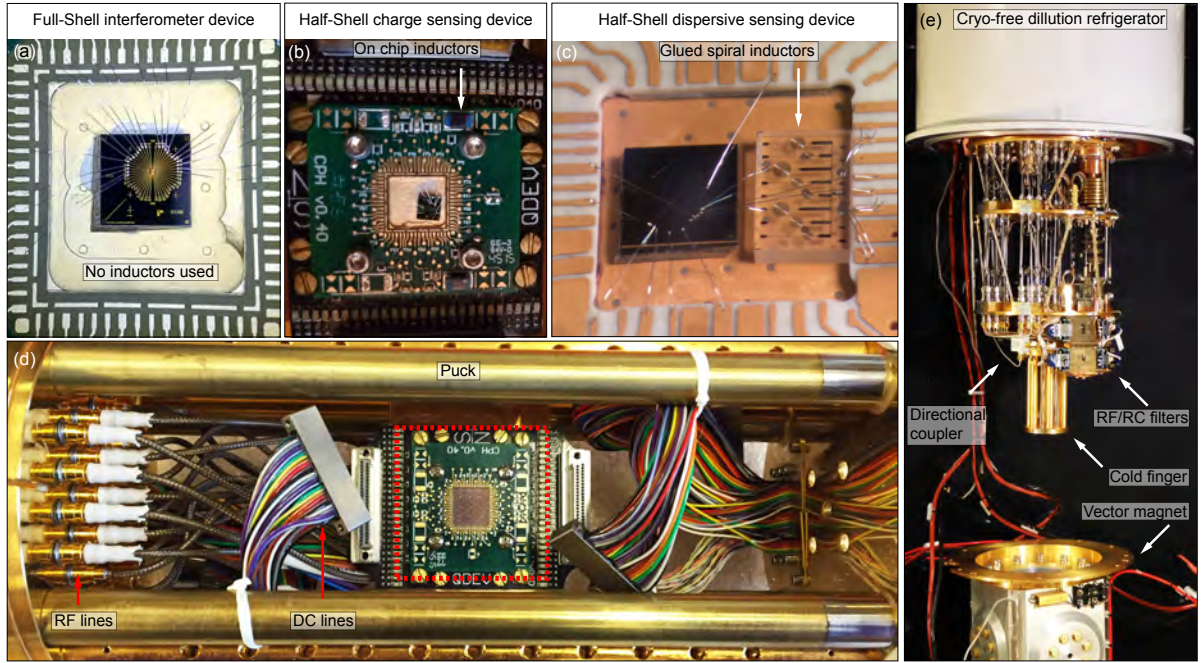
Figure 2.4: Bonding and loading individual devices. (a) Cleaved blank-chip with full-shell nanaowire interferometer devices glued to the daughterboard with bonding wires (no inductors used).(b) Half-charge sensing device chip glued on daughterboard with ceramic core inductors.(c) Half-shell dispersive sensing devices with glued spiral inductors.(d) Bonded devices onto daughterboard is placed into motherboard of the dillution fridge puck equipped RF and DC lines.(e) Image of open cry-free dilution refrigerator, equipped with vector magnet.

techniques Fig. 2.4(b)-(c), with an on-chip ceramic core and spiral inductors, respectively. Each bonded daughterboard is mounted onto the motherboard that is fixed in a cryogenic brass cylindrical-shaped puck that is equipped with rf and dc wiring [see Fig. 2.4(d)].

2.5 Measurement setup

The experiments were carried out in a cryo-free dilution refrigerator with a base temperature of ∼20 mK, equipped with vector magnet 6–1–1 T. Standard lock-in amplifier with frequencies < 200 Hz were used to measure both differential conductance, dI/dV_b, and differential resistance, dV/dI_b, for devices in this thesis [Fig. 2.5].
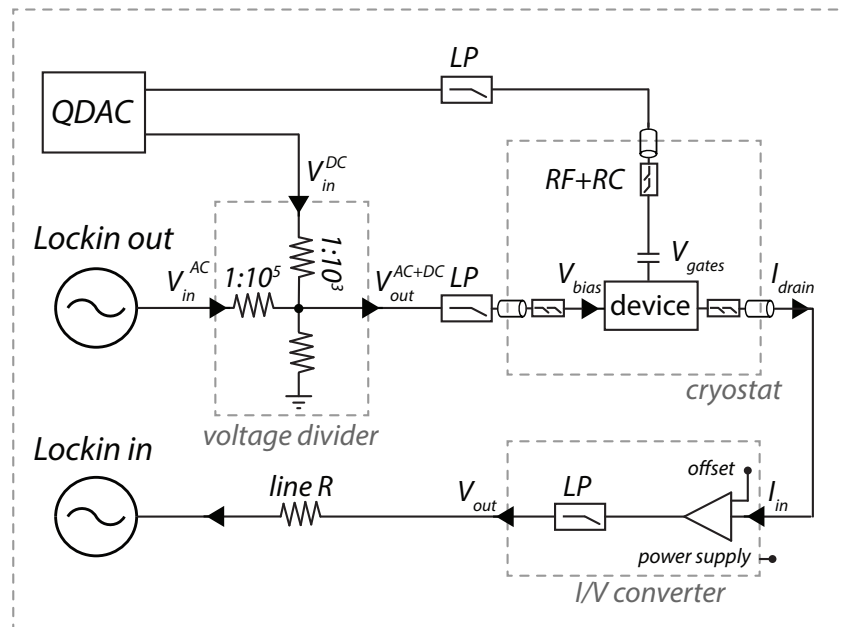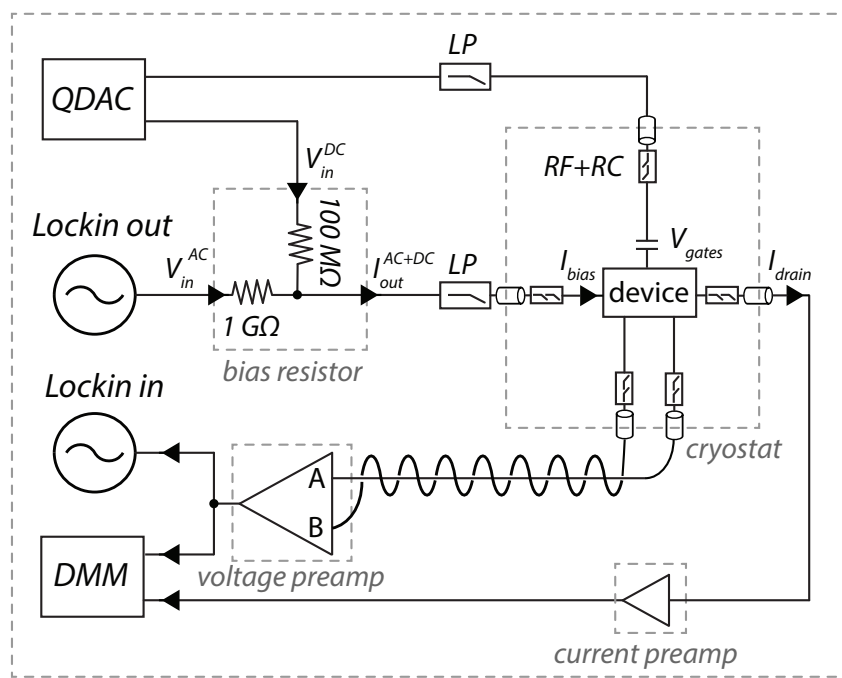
Figure 2.5: Transport measurement setups for voltage and current-bias. (a) Voltage-bias setup for measuring full-shell interferometer and half shell charge sensing devices. (b) Current-bias setup for measuring full-shell interferometer devices. Figures were inspired by Ref [49]

3

NIS AND *SNS* JUNCTIONS

Improving tunability of hybrid InAs/Al nanowire devices is important not only for finding clear signatures of Majorana bound states but also for peeving the way to nanowire-based topological qubits [50, 51]. In this chapter, we explore different tunneling gate geometries and compare them. First, we show the limitations of side-gated tunneling devices. Second, an improved device geometry with an overlapping lead and top-gate is presented. Clean tunneling spectroscopy with a reduced number of junction quantum dots is observed and could be used for finding clear signatures of Majorana zero modes in nanowires. Finally, we present a three overlapping gate geometry that shows sharp and clean tunable junction spectroscopy that could be used in fast on and off switch between regimes with and without charging energy, which is one of the key requirements in recent topological qubit proposals [52, 53].

3.1 Introduction

R ecent years have seen a lot of interest in using superconductor-semiconductor heterostructures for various applications starting from a nanowire-based charge sensing [54, 55] to proposals for the realization of topologically protected qubits [53, 56]. By now some experiments show that hybrid one-dimensional nanowire systems under certain conditions can act as an environment where Majorana zero modes emerge [57–59] which show potential in building topologically protected qubits.

Some of the proposed schemes rely on tuning the Josephson energy using flux [60] or using electrostatic gates suggested to dynamically control the Josephson E_J and charging E_C energies [53]. The gates are responsible for coupling or decoupling the rest of the one-dimensional system to the environment depending on the voltage on the gate. Such control between the E_J and E_C dominant regimes has to happen faster than the relaxation time of the qubit [56].

The absolute voltage control of closed and open regimes becomes important considering the characteristic breakdown voltage of the dielectric as well as operational voltages which all have to be lower than this breakdown limit. At the same time the relative voltages between the regimes with $E_J/E_C \gg 1$ and $E_J/E_C < 1$ also matter because arbitrary waveform generators involved in qubit control pulse sequences have only a limited voltage output range. When unavoidable intentional and unintentional attenuation in high-frequency lines in dilution refrigerators is taken into account the maximum available voltage range at room temperature is reduced at cryogenic temperatures. As a result, this makes it preferable to aim for control of the junction (E_J) within a relatively narrow range of voltages below the breakdown limit with a nanosecond time resolution that is accessible in experimental low-temperature physics laboratories.

In this chapter, motivated by the technological challenges involved in realizing the electrostatic gate-controlled topological qubit [52], we investigate several relevant tunneling barrier geometries defined by etching in hybrid InAs/Al nanowires. We demonstrate a significant reduction of pinch-off range by employing the gate dielectric by ~ 40 times compared to side-gate geometry. We also introduce the overlap-

ping gate geometry that combines both the small pinch-off range with the hard induced superconducting gap and a minimal amount of junction quantum-dots.

3.2 Side-gated devices

Current experiments in hybrid epitaxial nanowires mostly focus on exploring the properties of epitaxial InAs/Al [48, 61] and InSb/Al [59, 62] nanowires where the core is made of InAs and InSb, the shell is made from Al that is evaporated in the Molecular Beam Epitaxy system without breaking the vacuum. To achieve the mentioned control of the Josephson energy E_J [56] the nanowire is usually subjected to harsh conditions where the Al is selectively removed with the wet etch that is supposed to leave the InAs minimally intact. However, due to non-perfect etching time control and surface irregularities, Al removal
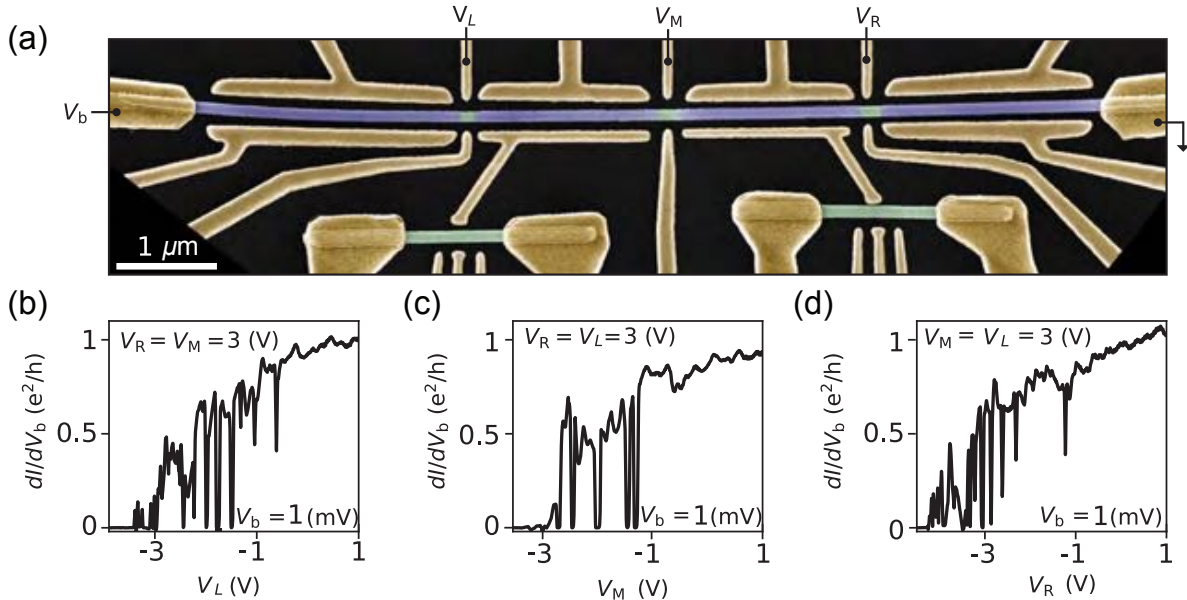
Figure 3.1: Half-shell side-gated geometry device with pinch-off traces. (a) False-color electron micrograph of half-shell InAs/Al nanowire with three etch regions controlling tunneling barrier with side-gates (V_L, V_M and V_R independently). (b) Differential conductance measurement, dI/dV_b, as a function of V_L gate showing a typical pinch-off trace for side-gated devices at finite voltage-bias, $V_b = 1$ mV, while keeping other two gates, V_M and V_R, at positive voltages with no voltage drop across. (c) the same as (b) except V_M is varied while keeping V_L and V_R at fixed positive voltages. (d) the same as (c) only V_R is varied, with V_L and V_M fixed to +3 V.

always leaves surface defects and small potential variations that can act as trapping centers for charges. After exposure to Al wet etchant, nanowire facet erosion may occur. Thus after etching, the nanowire surface is terminated with more oxides (presumably indium or arsenic oxide) or adsorbents from the wet etch itself. As a result, accidental quantum dots can be formed in the etched region. This gives rise to more surface states which will scatter more electrons propagating within the bulk of the wire. These accidental dots are responsible for introducing unintentional multiple dips and peaks in conductance as a function of the barrier gate. The appearance of such resonances is hard to control.

A side-gated nanowire device is presented in Fig. 3.1(a), the geometries closely resemble the theoretical proposals [56] for observing Majorana zero mode fusion rules and coherent oscillations of the parity degree of freedom qubit. Al continuity is broken by selectively removing it [see Ch. 2.3]. Places were Al is removed have electrostatic sides-gates (V_L, V_M, and V_R) nearby that allows tuning the potential barrier height with applied voltage. To make the effect stronger every single junction has two individual side-gates on each side that would allow for a smaller voltage range to pinch-off the nanowire.

Figure 3.1(b) shows differential conductance measurement, dI/dV_b, as a function of the V_L gate. The so-called pinch-off trace was recorded at a finite bias ($V_b = 1$ mV) while keeping other gates (V_M and V_R) open with very positive voltages (+3 V). Hence the presented pinch-off traces are representing the behavior of junction as a function of V_L. The same measurement was repeated for the other two junctions in Figs. 3.1(b),(c). In all three junctions, one can see multiple amounts of accidental resonances for conductance values below around 0.8 e^2/h.

3.3   Overlapping top-gates

We introduce two possible paths towards reducing the number of accidental dots in the etched regions for clean tunneling spectroscopy and efficient control over closed and open regimes of the Josephson junction.

The first method has to do with employing the overlapping top-gate geometry. The voltage-controlled gate is on the HfO$_2$ [see Ch. 2.3] insulating layer to increase the coupling to the junction but now it is par-

tially overlapping with the metallic lead. In this case, it is possible to effectively make a very narrow junction. As experimentally discovered helps to minimize the number of accidental resonances in the pinch-off trace at the same time realize a clear, hard gap behavior not interrupted by as many accidental resonances as in previous barrier geometries. Gap hardness for a few different V_g values is shown in Fig. 3.2(c) together with a two-dimensional map showing the top-gate, V_g, dependence of the induced superconducting gap in NIS spectroscopy seen in Fig. 3.2(e). Zero-bias conductance in the superconducting state, G_S, as a function of normal state conductance, G_N, taken at $V_B = 0.3$ mV is shown in Fig. 3.2(d). We fit the experimental data to a theoretical dependence of superconducting and normal state conductance and find excellent agreement with theoretical expectations [63]:

$$G_S^{V_b=0} = 2G_0 \frac{G_N^2}{(2G_0 - G_N)^2} \tag{3.1}$$

3.4 Triple top-gates

The second possible method to minimize the number of accidental resonances that we discovered involves more complicated geometry having three gates per junction, see Fig. 3.3(a) for scanning electron micrograph and Fig. 3.3(b) for schematics. Here, instead of trying to avoid the accidental resonances by design we instead introduce an additional set of gates allowing to tune the electrostatic potential profile of the junction. In this triple gate geometry, two side gates are separated by an additional layer of oxide on top of which the third gate resides. Two outer gates act as a partially overlapping set of gates similar to the one presented in Fig. 3.2 and is responsible for minimizing the number of accidental resonances that were observed before. We note that while having multiple gates for single-junction makes the fabrication more complex it also introduces additional tuning parameters giving more flexibility. This allows us to tune the pinch-off trajectory in multi-dimensional space to minimize the number of accidental resonances. To demonstrate the principle of tunability we fixed the two outer gates to the same potential (voltage) and swept it at zero bias as a function of the V_M gate. The resulting map is shown in Fig. 3.3 together with several
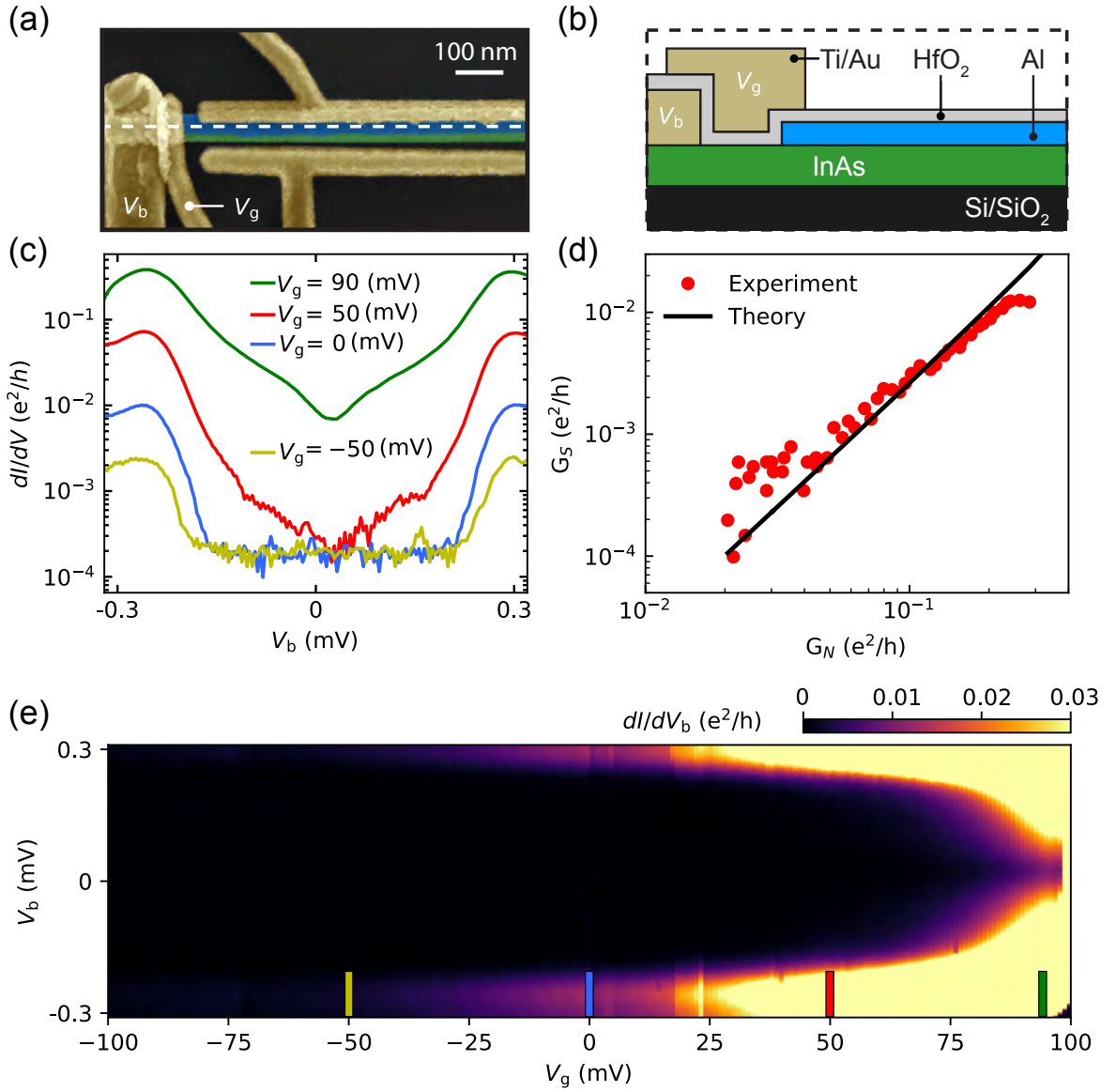
Figure 3.2: Overlapping NS top-gated geometry device with clean pinch-off. (a) False-color micrograph of a overlapping gate, V_g, with a bias lead, V_b. (b) Cross-sectional schematics of the device in (a) with dashed white line. (c) Differential conductance measurement, dI/dV_b, for different V_g values as a function of voltage-bias, V_b. (d) Extracted normal-state, G_N, and superconducting-state, G_S, conductance, with theoretical curve [63].
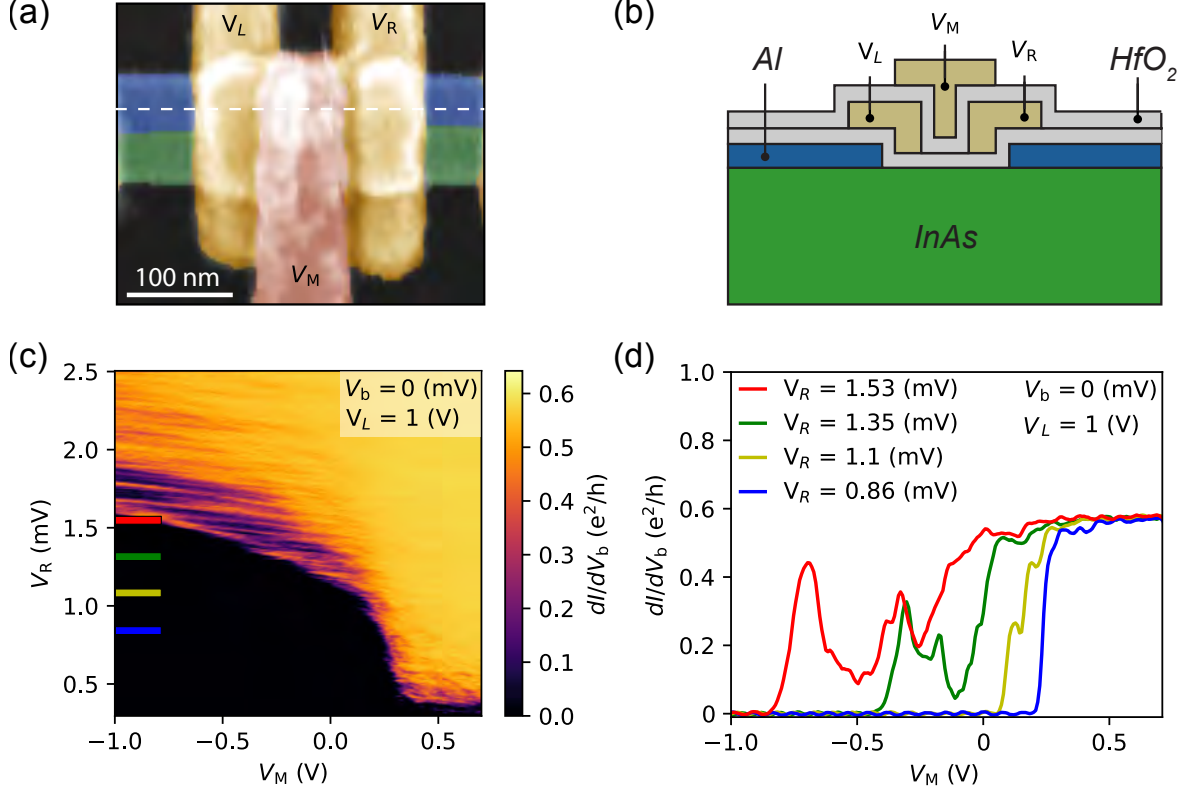
Figure 3.3: Triple SNS top-gated overlapping geometry device characterization. (a) False-color electron micrograph of SNS three top-gate overlapping geometry device with tunable V_L, V_M and V_R voltage gates. (b) Cross-sectional schematics of the device in (a) white dashed line. (c) Differential conductance, dI/dV_b, measurement as a function of two top-gates, V_R and V_M at zero-bias, $V_b = 0$, while keeping, $V_L = 1$ V (open regime). (d) Differential conductance traces at different top-gate voltages, V_R, in (c) as a function of V_M.

cuts and indicate the parameter space where gates have to be positioned to minimize the number of potential resonances. The pinch-of voltage range is on the order of a few hundred mVs, and readily accessible with available arbitrary waveform generators and there are a minimal number of accidental resonances deleterious to the pulsing protocols.

3.5   Conclusions

In summary, we report an experimental improvement for several tunneling barrier geometries for clean and effective tuning. We show that employing the dielectric one can reduce the effective voltage range needed to go from an open-to-close regime to values in principle accessible with currently available waveform generators. Secondly, we show an overlapping gate geometry allowing the minimization of the number of accidental junction dots. Finally, by employing the triple gate geometry we combine the advantage of a reduced pinch-off range and control over the cutter dots for future application.

4

QUANTUM-DOT PARITY EFFECTS IN TRIVIAL AND TOPOLOGICAL JOSEPHSON JUNCTIONS

In this chapter, we present a quantum-dot parity interferometer designed to probe topological superconductivity in proximitized nanowires. It is known that an odd-occupied quantum-dot in a Josephson junction can flip the transmission phase, creating a π-junction. When the junction couples topological superconductors, no phase flip is expected. We investigate this and related effects in a full-shell hybrid interferometer, using gate voltage to control dot-junction parity and axial magnetic flux to control the transition from trivial to topological superconductivity. Enhanced zero-bias conductance and critical current for odd parity in the topological phase reflects the hybridization of the confined spin with zero-energy modes in the leads.

---

4. QUANTUM-DOT PARITY EFFECTS IN TRIVIAL AND TOPOLOGICAL JOSEPHSON JUNCTIONS

4.1 Introduction

The development of topologically protected qubits [51, 52] for quantum computing [65, 66] benefits from fundamental investigations that examine signatures of topological superconductivity in various device geometries. These serve both to test theoretical models and solidify the interpretation of experiments [67, 68]. A fruitful system for exploring topological states is based on semiconductor nanowires with strong spin-orbit coupling in contact with a metallic superconductor [38,39,69]. Recently, semiconductor nanowires with a fully surrounding superconducting shell were found to offer a convenient means of tuning into the topological phase using applied axial magnetic flux [70]. In this system, the destructive Little-Parks effect [71], with the associated winding of the superconducting phase around the shell, induces a topological phase in the semiconductor core.

Here, we investigate Josephson junctions realized in full-shell InAs/Al nanowires, focusing on parity effects of a gate-controlled quantum dot in the junction. We investigate even and odd occupancies of the dot for the zeroth and first lobes of the reentrant Little-Parks structure in the leads. The hybrid nanowire containing the dot-junction is embedded in a superconducting interferometer, allowing the phase across the dot-junction to be measured relative to a reference arm containing a second gate-controlled junction. Depleting the reference junction *in situ* with a gate voltage allowed the dot-junction to be measured in isolation, revealing related parity-dependent features in conductance.

Two main results are reported: (1) First, differential conductance of the isolated dot-junction as a function of applied voltage bias showed a strong zero-bias peak throughout the first lobe only for an odd-occupied dot-junction, reminiscent of Kondo-enhanced zero-bias conductance peaks [72–74] seen for odd-occupied dots with superconducting leads [72–87]. To our knowledge, this effect has not been predicted or previously observed. When the dot-junction had even occupancy, the zeroth and first superconducting lobes showed comparable conductance at all biases. (2) Second, opening the reference junction to connect the interferometer loop, we observed a 0-π transition as a function of dot occupancy in the zero lobe, as previously reported [25, 26, 82, 88],

while in the first lobe, the 0-π transition was absent, as recently predicted [89–93] but not previously reported experimentally.

The absence of a π-junction in the first lobe can be understood as resulting from hybridization (anticrossing) of the electronic level in the dot-junction with zero-energy states in the leads, which protects the hybridized state around the junction from undergoing a parity switch where the corresponding unhybridized level would have crossed zero [93]. Hybridization of an odd junction state with *discrete* zero-energy states in the leads are reminiscent of, but distinct from, Kondo hybridization [94], which also favors a 0-junction [73, 82, 85, 87, 95, 96].

Supercurrent through a conventional Josephson junction is given by $I = I_\mathrm{c} \sin(\varphi)$, where I_c is the critical current, and φ is the phase difference of the superconducting order parameter across the junction. In few-channel junctions, including the semiconductor junctions, investigated here, higher harmonics of $I(\varphi)$ are also present, but the basic periodicity, $I(\varphi) = I(\varphi + 2\pi)$, and symmetry, $I(\varphi) = -I(-\varphi)$, remain [97]. Symmetry upon reversing phase can be lifted for particular arrangements of magnetic and spin-orbit fields [27, 98] not considered here, and the 2π periodicity broken by Majorana coupling [99, 100], which is not observed here.

As discussed in recent proposals [89–93], the transmission phase through a quantum dot embedded in a Josephson junction—a well-studied system, see experimental [101] and theoretical [85, 102] reviews—provides a means of investigating topological superconductivity. The Coulomb energy of the dot-junction suppresses Cooper-pair tunneling, relying on spin-dependent cotunneling processes, which in turn depend on dot occupancy [23, 25, 87, 88, 103–105]. In its simplest form, for even dot parity (*e*-state), the phase across the junction matches the conventional current-phase relation, while for odd parity (*o*-state), supercurrent typically involves a sign reversal, $I = I_\mathrm{c} \sin(\varphi + \pi) = -I_\mathrm{c} \sin(\varphi)$, resulting in a supercurrent reversal, or π-junction.

4.2 Materials and Methods

InAs nanowires with ~ 130 nm diameter were grown by molecular beam epitaxy using the vapor-liquid-solid method, followed by *in-situ* growth of a ~ 30 nm epitaxial Al shell fully surrounding the semi-
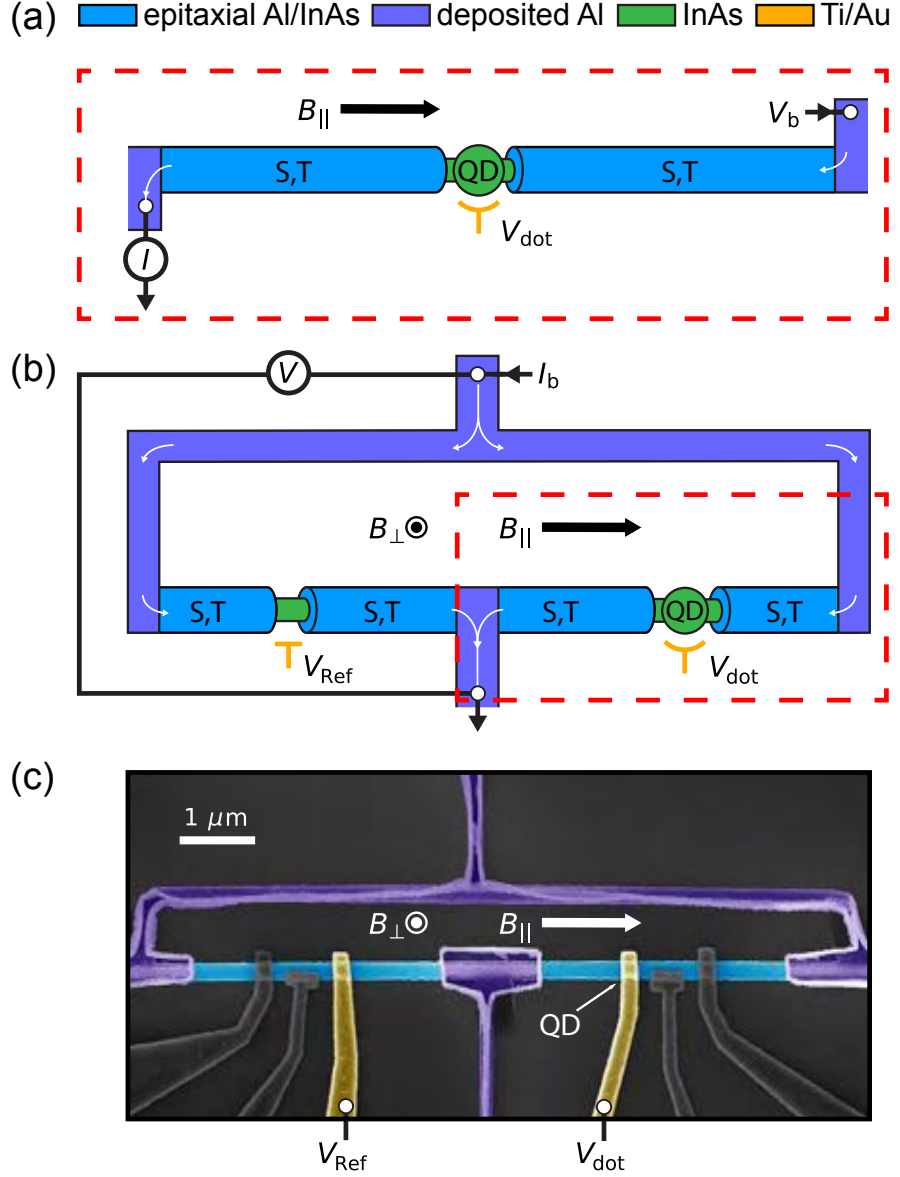
Figure 4.1: Schematics and false-color electron micrograph of interferometer device.
(a) Schematic of dot-junction made from an InAs nanowire (green) containing a quantum dot (QD) with coupling and occupancy controlled by voltage V_{dot}. A voltage bias, V_b, with a small AC component was applied across the single dot-junction and the current, I, measured. Thin Al leads (purple) remain superconducting with applied $B_{\parallel}$. Lobe structure in the destructive Little-Parks regime accesses trivial (S) or topological (T) superconductivity in the leads [70]. (b) The dot-junction was embedded in an interferometer with a reference junction controlled by gate voltage V_{Ref}. Current bias, I_b, with small AC component was applied and voltage, V, measured. For asymmetric junctions, the perpendicular magnetic field, $B_{\perp}$, controlled phase across the dot-junction. (c) False-color micrograph of measured device, showing loop of thin Al deposited on ramps to contact the full-shell wire. Uncolored gates were set to $+2\,V$.

conductor core [46] [see also Fig. 2.1 (a)]. After placing the nanowires on an Si/SiO$_2$ substrate [see Ch. 2.2 and 2.3 for details], polymer ramps were patterned to connect a loop and leads made of 25 nm of deposited Al [see Appendix A], as shown in Fig. 4.1(c). The thin Al ensured that superconductivity was maintained in moderate fields along the nanowire axis. An insulating layer of HfO$_2$ (7 nm) was then deposited, followed by patterned Ti/Au top-gates used to control electron density in regions where the Al was removed by wet etching. An electron micrograph of one of the devices is shown in Fig. 4.1(c), with false-colored active regions and uncolored gates set to +2 V. All wire segments exceed 1 μm, several times the Majorana localization length, $\xi \sim 180$ nm [70].

Measurements were carried out in a dilution refrigerator with a base the electron temperature of ~ 50 mK using conventional lock-in techniques in both voltage-bias and current-bias configurations. A vector magnet provided independent control of the magnetic field along the wire axis, $B_\parallel$, and a small transverse field, $B_\perp$, was used to apply flux to the interferometer loop [see Fig. 4.1]. A total of ten devices were cooled. Three devices were reasonably stable and showed qualitatively similar behavior. One of those is presented in this chapter and the other two in the Appendix B. Among the others, three were nonconducting or did not show a supercurrent, two showed excessive noise and did not have a controllable dot in the junction, one did not show a π-junction in the zeroth lobe, and one appeared non-topological which we present in the main text, without zero-bias conductance feature in the first lobe and a π-junction in both lobes. Which we discuss at the end of this chapter.

4.3 Voltage-bias spectroscopy

With the reference arm closed by setting $V_{\text{Ref}} = -2$ V, the dot-junction was measured in a voltage-bias configuration, applying ac+dc voltage V_b (2 μV ac excitation), as shown in Fig. 4.1(a) [see also Fig. 2.5(a)]. At negative V_{dot}, approaching depletion, sharp resonances in tunneling conductance, dI/dV_b, were observed, indicating that a Coulomb blockaded quantum dot has formed in the junction. Note that V_{dot} controlled both the dot-junction occupancy and, on larger voltage scales, the coupling to the leads. Tunneling spectra at $B_\parallel = 0$,
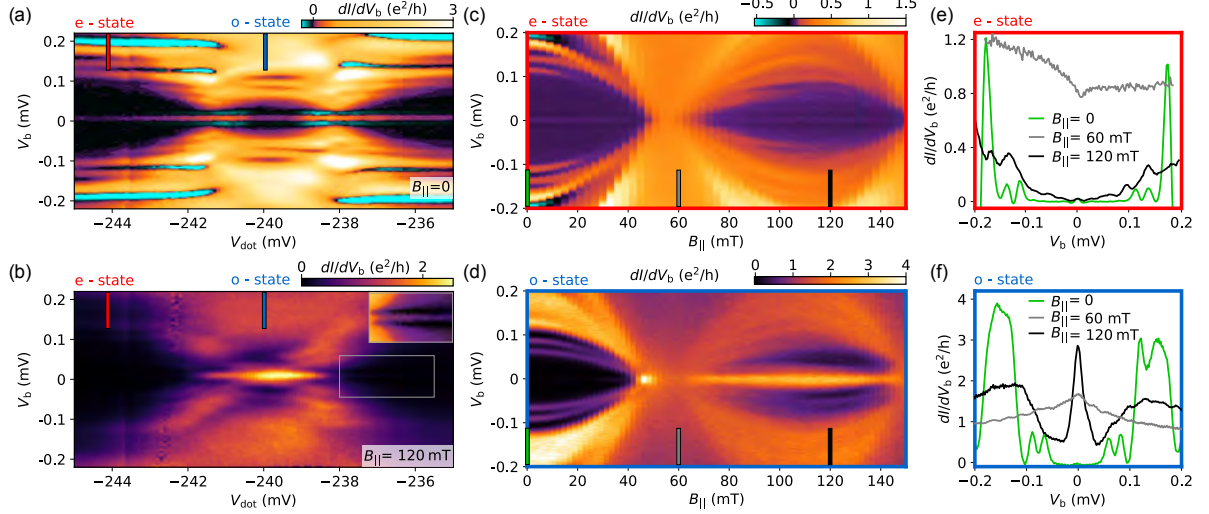
Figure 4.2: Bias spectroscopy of isolated dot-junction (with reference arm closed).
(a) In the zeroth lobe ($B_\parallel = 0$) showing differential conductance, dI/dV_b, as a function of DC bias V_b across the junction. As the gate voltage, V_{dot}, takes the occupancy of the dot from even (e-state) to odd (o-state) to even, a uniform conductance (supercurrent) peak at $V_b = 0$ is visible throughout the range of V_{dot}. Negative differential conductivity (green) are most prevalent in the e-state. Red (blue) cut indicate location of $e(o)$-state shown in (c(d)). (b) Same as (a) except in the first lobe ($B_\parallel = 120$ mT), where topological superconductivity in leads is expected. A strong enhancement of the zero-bias conductance peak occurs in the odd occupied state. (c) Lobe structure in bias spectroscopy as a function $B_\parallel$ for e-state. Green and black marks indicate cuts in (e). (d) Same as (c) for o-state, with green and black marks showing cuts in (f). Note the enhanced zero-bias conductance persisting through the first lobe, which is absent both in the zeroth lobe and in the e-state of the first lobe. We note, without explanation, a strong zero-bias feature over a small field range as the zeroth lobe closes, around 42 mT. (e) Cuts from (c) in the e-state showing small supercurrent peaks at zero bias in both the zeroth (green) and first (black) lobes. (f) Cuts from (d) in the o-state, showing a large zero-bias conductance peak in the first lobe.

across a range of V_{dot} spanning two e-states and one o-state are shown in Fig. 4.2(a). A narrow supercurrent feature at zero bias can be seen throughout the sweep with two enhancements at the charge transition points, corresponding to Coulomb blockade resonances. Negative differential conductance in the zeroth lobe [green stripes in Fig. 4.2(a)] at low bias near the charge transitions, and higher bias in the e-states presumingly reflects the opening of weakly coupled channels that blockade transport [106]. Their prevalence in the e-state indicates spin-dependent excited states for even occupancy.

50

Applying $B_\parallel$ reveals the lobe structure of destructive superconductivity, with suppressed superconductivity around $B_\parallel = 50 - 60$ mT and a first lobe centered around $B_\parallel = 120$ mT, corresponding to one quantum of applied flux and one twist of superconducting phase round the shell circumference. Figures 4.2(a,b) reveal a striking difference in bias spectra of the lobes. In particular, the first lobe [Fig. 4.2(b)] showed strongly enhanced zero-bias conductance in the o-state but not in the e-state, while spectra in the zeroth lobe showed similar conductance for both occupancies [Fig. 4.2(a)]. Bias spectra as a function of $B_\parallel$ in Figs. 4.2(c,d) show a complementary view: In the zeroth lobe, o-state and e-state spectra are comparable, while throughout the first lobe the zero-bias conductance is strongly enhanced only for the o-state, with enhancement roughly tracking the size of the topological gap. Cuts in Figs. 4.2(e,f) show a large zero-bias conductance peak in the first lobe for the o-state, with $12\,\mu$V half-width at half maximum. Cuts along zero bias as a function of $B_\parallel$ are shown in Appendix Fig. B.6. We note that the zero-bias peak in the o-state in the first lobe does not appear to split with increasing $B_\parallel$. For a conventional Kondo peak in conductance, for instance arising from a soft gap in the first lobe [74], the peak would be split by $2g\mu_B B_\parallel > 50\,\mu$eV in the first lobe, which would be visible.

We note in Fig. 4.2(d) a small, bright zero-bias peak at the closing of the zeroth lobe, $B_\parallel \sim 46$ mT. This small feature does not persist further into the zeroth lobe or into the destructive regime, where instead a broad zero-bias peak can be seen [gray cut in Fig. 4.2(f)], while in the e-state, the destructive regime had a zero-bias dip [gray cut in Fig. 4.2(e)]. The bright peak at $B_\parallel \sim 46$ mT is more easily seen in Fig. 4.2(e). We interpret the narrow peak at $B_\parallel \sim 46$ mT as Kondo-enhanced conductance in the superconducting regime [72–74]. From the ratio of superconducting to normal conductance, $G_S/G_N \sim 2$, [from Figs. 4.2(d) and B.6] we infer a rough ratio of Kondo temperature to gap, $T_K/\Delta \sim 2$ [72, 73]. Within this interpretation, the width of the peak and its appearance only at the closing of the zero lobe suggests a low T_K, of order 10 μeV. The zero-bias peak in the o-state destructive regime presumably reflects normal-state Kondo enhancement.

Zero-bias conductance peak width in the *o-state* dot occupancy is investigated in Fig. 4.3(a). The axial-magnetic field evolution as a function of voltage-bias is shown, with each cut having an offset of 0.25 e^2/h
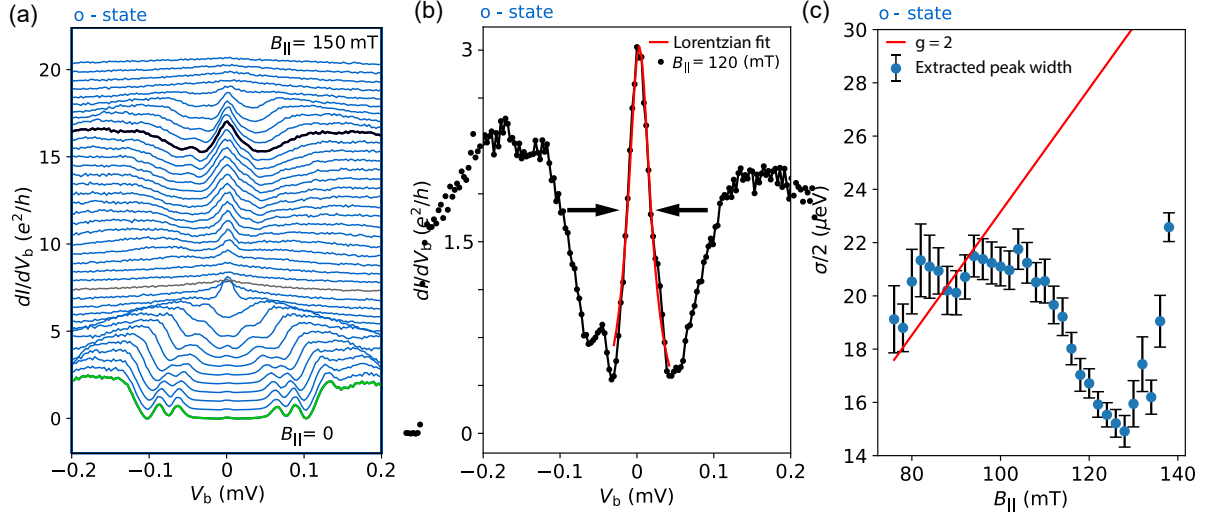
Figure 4.3: Bias spectroscopy as a function of axial-field evolution for odd quantum dot occupancy and extracted peak width. (a) Differential conductance, dI/dV, measurement voltage-bias cuts at different axial magnetic field, $B_\parallel$, in the o-state. Each cut has an offset of 0.25 e^2/h. (b) Differential conductance, dI/dV, voltage-bias cut at $B_\parallel = 120$ mT in the o-state with a Lorentzian fit to the data of the zero-bias peak in the first lobe. Extraction of $9\,\mu V$ half-width at half maximum from the fit. (c) Extracted half-width at half maximum peak widths, $\sigma/2$, for different $B_\parallel$ values in the 1st lobe, with theory prediction of Kondo peak width increase as a function of magnetic field for $g = 2$.

in steps of 5 mT. Figure 4.3(b) shows a voltage-bias cut of a differential conductance measurement at $B_\parallel = 120$ mT with fitted Lorentzian function. The fit is then done for different $B_\parallel$ field values in the first lobe, with extracted half-width at half maximum, $\sigma/2$, in Fig. 4.3(c). The expected Kondo peak splitting for g-factor of 2 [107] is plotted as a red line, which is not consistent with the measured peak width.

4.4 Current-bias

We investigate the dot-junction with current-bias, still with reference arm closed, $V_{Ref} = -2$ V, and varying dot-junction gate V_{dot} at $B_\parallel = 0$. Dot-junction gate, V_{dot}, covers e-state and o-state, and are indicated by red and blue markers, respectively. The measured differential resistance, dV/dI_b, as a function of applied current-bias, I_b, is shown in Fig. 4.4(a), the quantum-dot degeneracy points where superconducting state ($dV/dI_b = 0$) develops zero dV/dI_b resistance can be
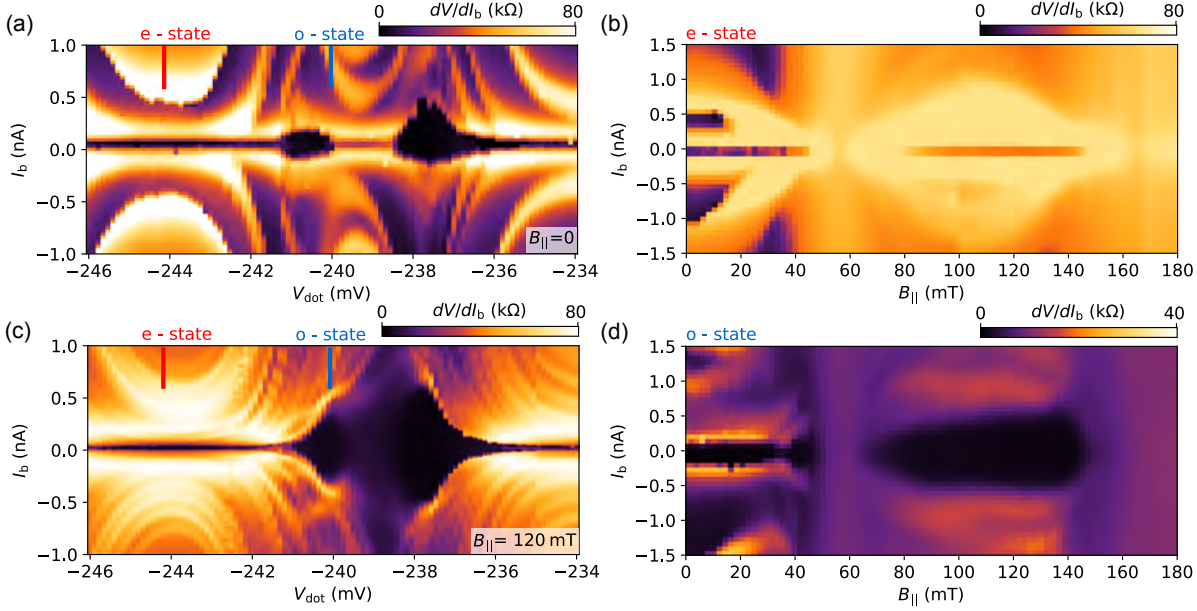
Figure 4.4: Current-bias of isolated dot-junction (with reference arm closed). (a) In the zeroth lobe ($B_\parallel = 0$) showing differential resistance, dV/dI_b, as a function of current-bias I_b across the junction, while varying V_{dot} gate that crosses e-state and o-state. (c) Same as (a) except in $B_\parallel = 120$ (mT). (b) Differential resistance measurement of isolated dot-junction in the e-state field sweep. (d) Same as (b) except in the o-state.

correlated to voltage-bias degeneracy points in Fig. 4.2(a). At finite axial magnetic fields, $B_\parallel = 120$ mT, dV/dI_b measurement is shown in Fig. 4.2(c) of the dot-junction, where the degeneracy points can still be distinguished. Continuous $B_\parallel$ measurements in Figs. 4.2(b)-(d) show, how zero differential resistance evolve for different dot-junction charge occupancies (*e-state* and *o-state*, respectively).

4.5 Superconducting phase control

Opening the reference arm by setting $V_{Ref} = 0$ V connected the interferometer loop, yielding a switching current of 2 nA in the reference junction, compared to $\sim$ 1 nA in the dot-junction. In the configuration of Fig. 4.1(b), whenever the current bias I_b exceeded the total switching current of the interferometer a finite differential resistance, dV/dI_b, appeared across the interferometer. Figure 4.5(a) shows dV/dI_b for dc current bias $I_b = 2$ nA (with ac excitation 0.2 nA) as a function of V_{dot} and $B_\perp$ in the zeroth lobe, with $B_\parallel = 0$. To avoid hysteretic ef-
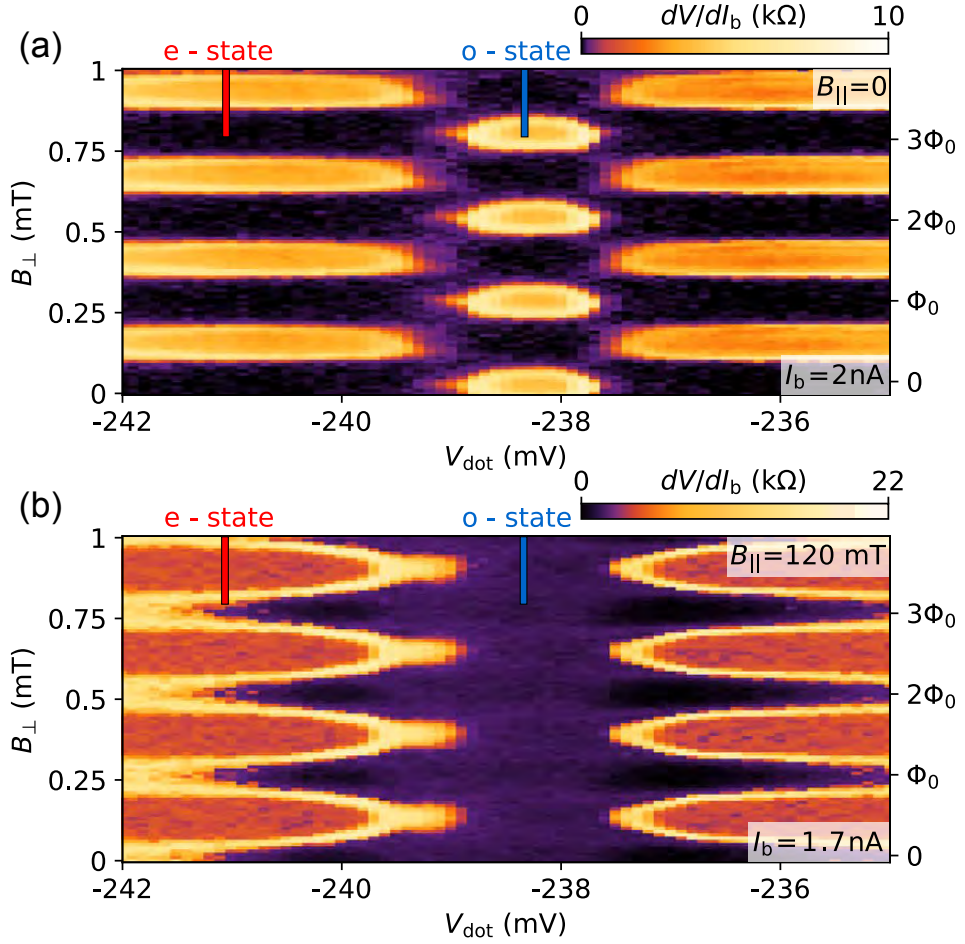
Figure 4.5: Differential resistance, dV/dI_b, of the interferometer as a function gate voltage, V_{dot}, controlling dot occupancy, and $B_\perp$, controlling flux through the interferometer. Current bias, I_b, was set to periodically exceed the total switching current of the interferometer. (a) The zeroth lobe ($B_\parallel = 0$) with $I_b = 2$ nA, showed a π phase shift in the o-state relative to the e-state, indicating a π-junction. (b) Same as (a) except in the first lobe ($B_\parallel = 120$ mT) with $I_b = 1.7$ nA, showing no phase shift as a function of V_{dot}.

fects, I_b was briefly set to zero then reset to 2 nA for each data point (pixel) in the two-dimensional plot. Figure 4.5(a) shows the periodic dependence of the zero-resistance state with magnetic flux through the interferometer, consistent with $\Delta B_\perp A = \Phi_0 = h/2e$, where A is the area of the interferometer [see micrograph in Fig. 4.1(c)]. As V_{dot} was swept from the e-state to the o-state, the phase of oscillation with $B_\perp$ shifted by $\Phi_0/2$, indicating that the dot-junction is a π-junction in the o-state relative to the e-state.

Figure 4.5(b) shows a similar plot of dV/dI_b as a function of $B_\perp$ and V_{dot}, now in the first lobe, taken at $B_\parallel = 120\,\text{mT}$, demonstrating the *absence* of a π phase shift for relative occupancies. The absence of π-junction behavior for topological dot-junctions is consistent with theoretical predictions [91–93]. Oscillations in dV/dI_b are less visible in the *o*-state in the first lobe [Fig. 4.5(b)] compared to the zeroth lobe [Fig. 4.5(a)]. This is because the switching current of the dot-junction was considerably larger in the *o*-state in first lobe, so that the total switching current of the interferometer barely exceeds the fixed bias $I_b = 2$ nA. This is more clearly seen by measuring dV/dI_b as function of a swept I_b, as shown in Fig. 4.6. Differential resistance dV/dI_b of the interferometer along cuts through the *e*-state and *o*-state of the dot-junction showed oscillatory patterns of switching and retrapping currents with applied flux, noting that I_b was stepped from negative to positive. Retrapping occurs at negative values of I_b. Similar data for the other devices are shown in Appendix B.4 and B.5. Phase plots at other fields for device 1 are shown in Fig. 4.7.

We draw attention to several features in Fig. 4.6: (i) There is a π phase shift between panels (a) and (c), indicating that in the zeroth lobe, the *o*-state forms a π-junction relative to the *e*-state. (ii) There is no π phase shift between panels (b) and (d), indicating that in the first lobe there is no relative π-junction upon changing dot occupancy. We do not observe a nontrivial phase shift in (d), noting that $B_\parallel$ is probably too small to induce a single-triplet crossing [108]. (iii) The absolute phase of oscillations as a function of $B_\perp$ is the same in all four panels, with only the *o*-state in the zeroth lobe shifted by π [panel (c)]. We note that phase was not corrected for a given $B_\parallel$. (iv) Retrapping currents in the zeroth lobe [panels (a,c)] are considerably smaller than switching currents, a consequence of underdamping and junction heating in the resistive state. Retrapping and switching currents are roughly the same in the first lobe, presumably due to subgap modes that both dampen junction dynamics and cool the junction through the leads. While these features warrant further study, we take this as possible indirect evidence for increased junction damping and thermal conductivity in the first lobe. (v) Finally, we observe that switching and retrapping currents in the *e*-state and the *o*-state are comparable in the zeroth lobe [panels (a,c,e)] whereas in the first lobe, switching currents are larger in the
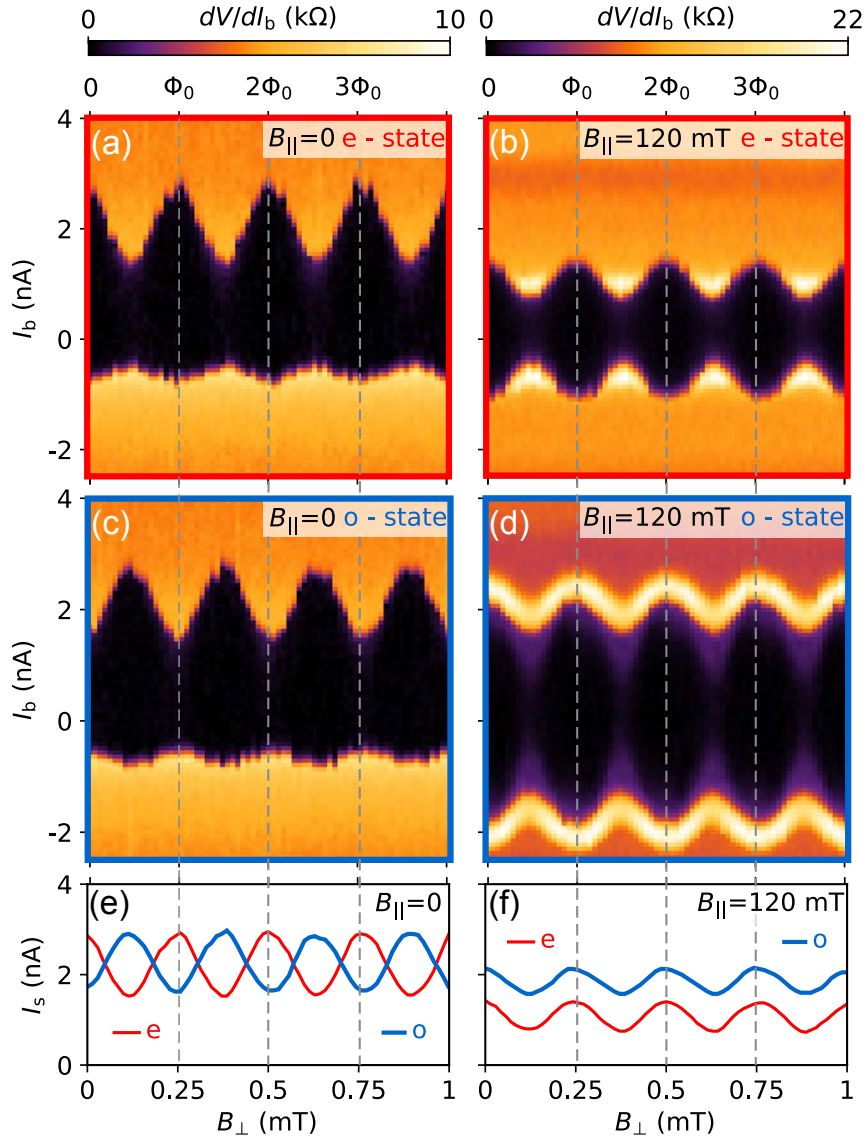
Figure 4.6: **Differential resistance,** dV/dI_b, **of the interferometer as a function of
bias current,** I_b, **and perpendicular magnetic field,** $B_\perp$. (a,c) in the zeroth lobe, along
cuts through the $e(o)$-state [red(blue) dashed line in Fig. 4.5(a)], showing relative π
phase shift, and (b,d) in the first lobe, along cuts through the $e(o)$-state [red(blue)
dashed line in Fig. 4.5(b)], showing absence of phase shift. Note in (a,c) that switching
currents exceed retrapping currents. (b,d) In the first lobe ($B_\parallel = 120$ mT), switching
and retrapping currents are comparable. (e) Relative phase shift of π between e-state
(red) and o-state (blue) in the zeroth lobe. (f) no phase shift between the e-state (red)
and o-state (blue) in the first lobe ($B_\parallel = 0$), where both phases align with the e-state
(red) in the zeroth lobe. Critical current in the o-state (blue) exceeds the e-state (red) in
the first lobe ($B_\parallel = 120$ mT).

o-state than in the *e*-state [see panels (b,d,f)], as anticipated form the isolated dot-junction data in Fig. 4.2, where the *o*-state showed enhanced conductance compared to the *e*-state in the first lobe. Dependences of critical current on gate voltage, spanning *e*- and *o*-states, for the zeroth and first lobes, showing enhanced critical current in the first lobe for the *o*-state, is shown in Appendix Fig. B.7.

We revisit the small feature at $B_\parallel \sim 46$ mT, interpreted above as Kondo-enhanced conductance at the closing of the zeroth lobe, now in the interferometer configuration. We observed enhanced critical current, $I_c \sim 1$ nA, and 0-junction behavior at that location, contrasting the π-junction behavior inside the zeroth lobe. The enhanced critical current is consistent with an estimate for an overdamped junction, $G_S/G_N \sim \exp(\hbar I_c/ek_B T)$ [73]. Taking $G_S/G_N \sim 2$ and temperature $T \sim 50$ mK yields $I_c \sim 1$ nA, close to the measured value, which we highlight in current-phase relation measurements in Fig. 4.7.
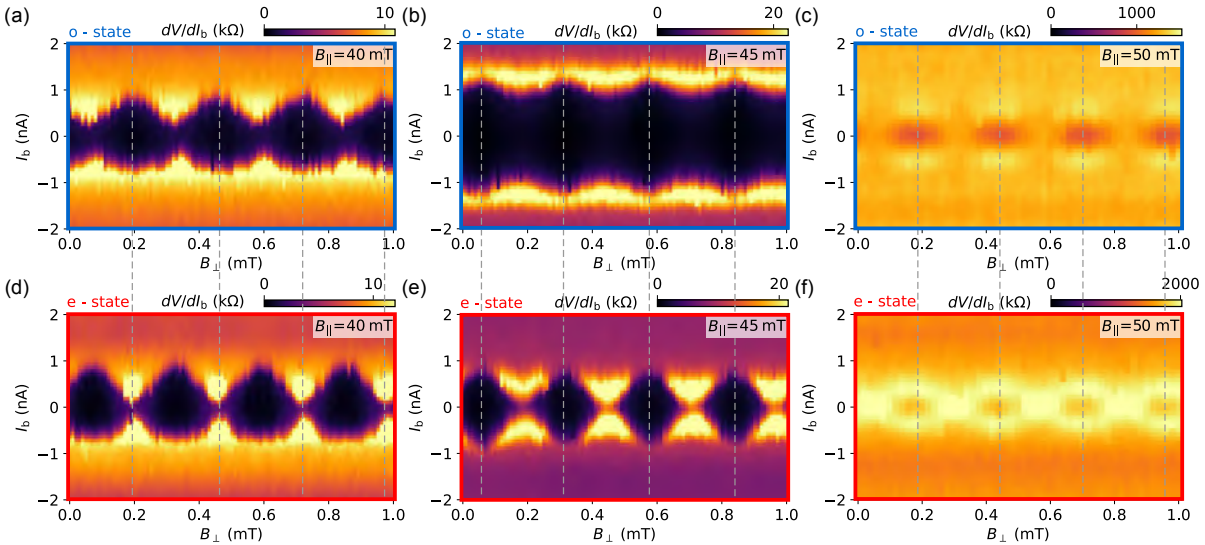
Figure 4.7: Differential resistance, dV/dI_b, as a function of current bias, I_b, and perpendicular field $B_\perp$ at different fixed axial fields, $B_\parallel$. (a,d) Within the first lobe, $B_\parallel = 40$ mT, for even and odd dot-junction occupancies. Note π phase shift between odd (a) and even (d) states. (b,e) On the bright spot, $B_\parallel = 45$ mT, at the closing of the zeroth lobe [see Fig. 4.2(c-d)]. Note that even and odd states are in phase. (c, f) Entering the destructive regime, $B_\parallel = 50$ mT, with suppressed coherence effect, even and odd occupancies are in phase.

4.6 0-π transition in a non-topological wire

We present other similar devices measured where 0-π transition is observed in both zeroth and first lobes but without strong zero bias peaks in the odd state of the quantum dot in first lobe.

Figure 4.8 shows both isolated dot-junction voltage-bias spectroscopy with reference arm closed and current-bias with reference arm open to probe the 0-π transition. The isolated dot-junction differential conductance, dV/dI_b, is measured as a function V_{dot} and voltage-bias in Fig. 4.8(a), with gate voltage range covering e-state and o-state marked in red and blue markers at $B_{||} = 0$. The same measurement is repeated in the first lobe ($B_{||} = 100$ mT) and is shown in Fig. 4.8(b). We note that in the first lobe we do not see any enhancement of zero-bias conductance in the o-state as previously seen in other main text device [see 4.2] as
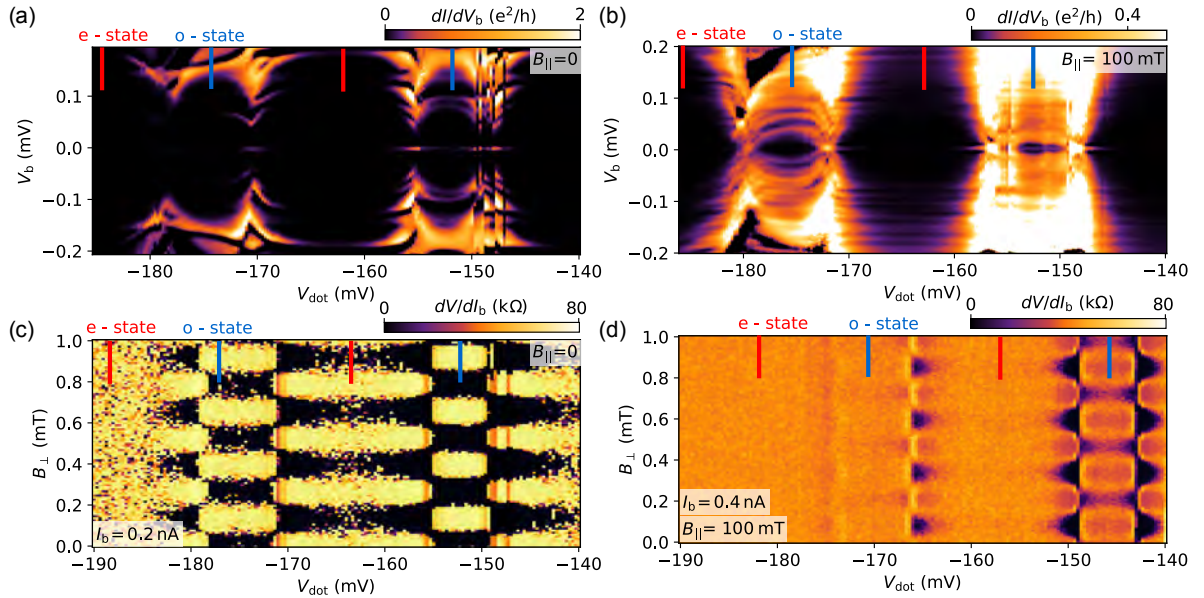
Figure 4.8: Other device measured preserving 0-π transition without zero-energy states in the first lobe. (a) In the zeroth lobe ($B_{||} = 0$) showing differential conductance, dI/dV_b, as a function of DC bias V_b across the junction. b) Same as (a) except in the first lobe ($B_{||} = 100$ mT). Compared to previous devices, no enhancement in conductance at zero-bias was observed in the o-state. (c) Differential resistance, dV/dI_b, in the zeroth lobe ($B_{||} = 0$) with fixed $I_b = 0.2$ nA, showed a π phase shift in the o-state relative to the e-state, indicating a π-junction. (d) Same as (c) except with fixed $I_b = 0.4$ nA in the first lobe ($B_{||} = 100$ mT), indicating a preserved π phase shift in the o-state relative to the e-state.

well presented in Appendix B.2 and B.3.

4.7 Conclusions

In summary, we have shown a novel means of probing topological superconductivity using quantum-dots in Josephson junction that are embedded into an interferometer. Using voltage-bias spectroscopy we identify a quantum-dot with zero energy states in the first superconducting lobe. Zero-bias conductance peak width suggests a non-Kondo resonance peak in the *o-state* as the axial-magnetic field is increased. Operating the device with the reference arm opened, we identify a π-junction in the zeroth lobe. In the first lobe, we find an absence of a π-junction, that could suggest hybridization of the confined spin with zero-energy modes in the leads. Finally, we show the presence of a π-junction in both zero and first lobes presumingly in a non-topological wire, where strong zero-bias conductance peak in the odd state is absent.

5

TOPOLOGICAL ISLANDS IN FULL-SHELL NANOWIRE INTERFEROMETERS

This chapter further explores hybrid InAs/Al with full-shell nanowire islands that are embedded into an interferometer. Voltage-controlled gate allows to form a superconducting island with finite charging energy and Coulomb blockade. We investigate two different island lengths on separate devices. External axial magnetic field evolution shows charge transition from $2e$ to $1e$ as predicted by the finite length of the topological island. With an open interferometer, the device shows no sign of supercurrent reversal at axial fields where the topological phase is expected, which is consistent with theoretical predictions [91]. Also, we find strong and weak coupling regimes reflected in unusual number of Coulomb peaks that appear in the topological regime.

5.1 Introduction

Recent experiments have shown that finite Majorana islands have a distinct signature, where Coulomb blockade peak spacing oscillates as function of axial-magnetic field. For topological islands with finite charging energy, E_C, Majorana wavefunction overlap amplitude should decrease exponentially as the island length increases [51, 56], which Ref [57] experimentally have shown. Other experiments by Ref [70] discovered that by using fully covered Al in InAs nanowires, one can achieve the topological phase relying on Little-Parks effect [71] without the need of tuning the density of nanowires, since the chemical potential is fixed by the geometry of the nanowire cross sectional dimensions. In addition, magnetic fields needed to reach the topological phase was found to be smaller by a factor of 10 compared to half-shell nanowire devices.

5.2 Experimental setup

In Ch.4 we have explored 1D systems that could host topological phases of matter at the ends of proximitized superconductor. Here we further investigate full-shell Al nanowires in a different device geometry, where finite charging energy Coulomb islands are formed using tunneling gates and axial-magnetic field tunes between trivial and topological phases. The devices are embedded into an interferometer geometry, similar to Ch. 4, and are shown in Fig. 5.1, with (a) showing the full interferometer device that can be operated in voltage and current-bias setups. Applying voltages to V_1 and V_{Ref} it is possible to switch on (current-phase-relation measurement) and off (voltage and current-bias of the island measurement) interferometer.

Two different island length devices were investigated: Device A, with 300 nm island as shown in Fig. 5.1(b); Device B, with 700 nm island shown in 5.1(c). In both devices charging energy of the island is subjected by using V_L and V_R voltage-controlled tunneling barriers. The charge offset of the island is controlled using V_g voltage gate as seen from Fig. 5.1(a). The ground state energy dispersion of the Coulomb blockaded islands is plotted in 5.1(d) for even and odd en-
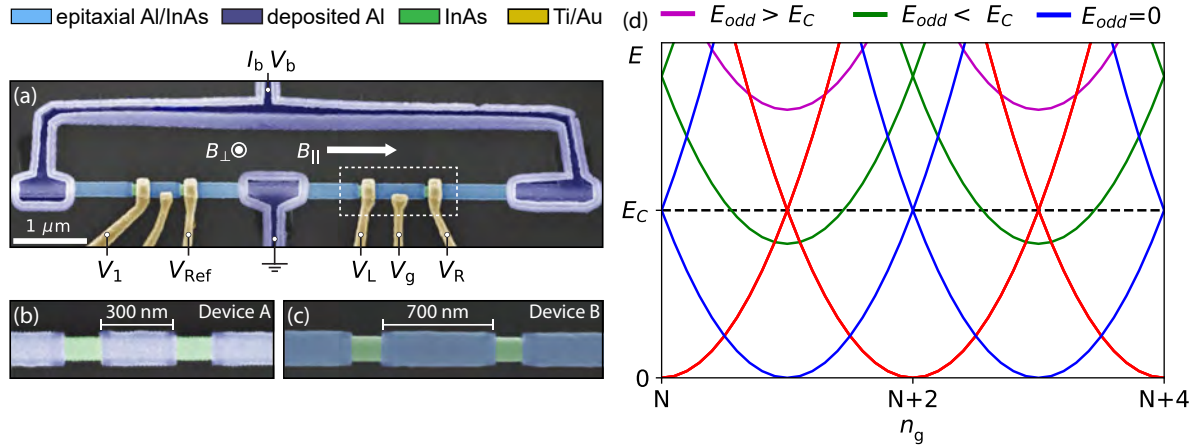
Figure 5.1: Full-shell Al island nanowire interferometers. (a) False-color electron micrograph of interferometer device with Majorana island defined shown in white dashed rectangle on the right side of the device and reference junction on the left with for phase control. Voltage controlled gates, V_1 and V_{Ref}, control reference arm of the interferometer which can be fully closed for voltage and current-bias measurements. External magnetic fields, $B_{||}$, and $B_{\perp}$ control the superconducting lobe structure (trivial and topological states) and flux through the interferometer loop, respectively. Voltage top-gates V_L, V_g and V_R define the Majorana island. (b) Different device with 300 nm island. (c) Another investigated device with 700 nm island. (d) Ground state energy dispersion parabolas of Coulomb blockaded islands for different charge occupation, plotted using Eq. 5.1.

ergy, E, parabolas using Eqs. 5.1.

$$E = \begin{cases} E_C(n - n_g)^2 + E_{odd} & if \ \ n = 1, 3, 5... \\ E_C(n - n_g)^2 & if \ \ n = 0, 2, 4... \end{cases} \tag{5.1}$$

The ground-state energy for odd parabolas, E_{odd}, is brought down to zero by applying an external magnetic field. At the degeneracy points within ground-state, charge transfer occurs through the island. For $E_{odd} > E_C$, charging of the island by 2e. As the magnetic field is increased, the lowest odd parabola comes down, below the charging energy, E_C, two new degeneracy points appear that transfer even and odd charge number as the offset, n_g, is changed. In the topological regime, where Zeeman field exceeds critical field Eq. 1.52, then degeneracy points have equal spacing in charge offset and transfer becomes 1e periodic for island lengths > 1μm.

5.3 Device-A

First interferometer device with 300 nm island is presented from 5.1(b), operating in voltage-bias setup, where the reference arm is closed by setting V_1 and V_{Ref} to -2 V. In this regime the only path of the current is through the right arm. Differential conductance, dI/dV_b, measurement is taken while fixing V_L and V_R gates to tunneling voltages, and changing V_g as a function of applied voltage-bias we get Coulomb blockade diamonds as seen in Fig. 5.2(a) at $B_{||} = 0$. Strong even-odd peak spacing is observed at $V_b = 0$ as V_g gate is changed, which could indicate $E_C > \Delta$. In Fig. 5.2(b) Coulomb blockade diamonds are taken again except in $B_{||} = 110$ mT, where almost 1e charge peak spacing is observed at $V_b = 0$ as the charge offset, V_g, is changed. To track the peak spacing evolution with an axial magnetic field, voltage-bias is set to zero and V_g is changed as a function of $B_{||}$, and it is shown in 5.2(c). Peak spacing analysis was done as described in Appendix C where individual Coulomb peaks are fitted to Lorentzian shape function and best-fit peak position is extracted.

$$L(n_g) = \frac{1}{2\pi} \frac{\sigma}{(n - n_g) + (1/2\sigma)^2},\tag{5.2}$$

where σ defines the full-width peak. Applying this analysis to multiple peaks and finding the averaged value for even and odd spacing Fig. 5.2(d) is produced. Following the same analysis as Ref [70] and discussed in Appendix C, energy splitting in the 1st lobe where the topological phase is expected, is calculated $E = 25$ μeV, which compares reasonably well with measured values in previous experiments [70].
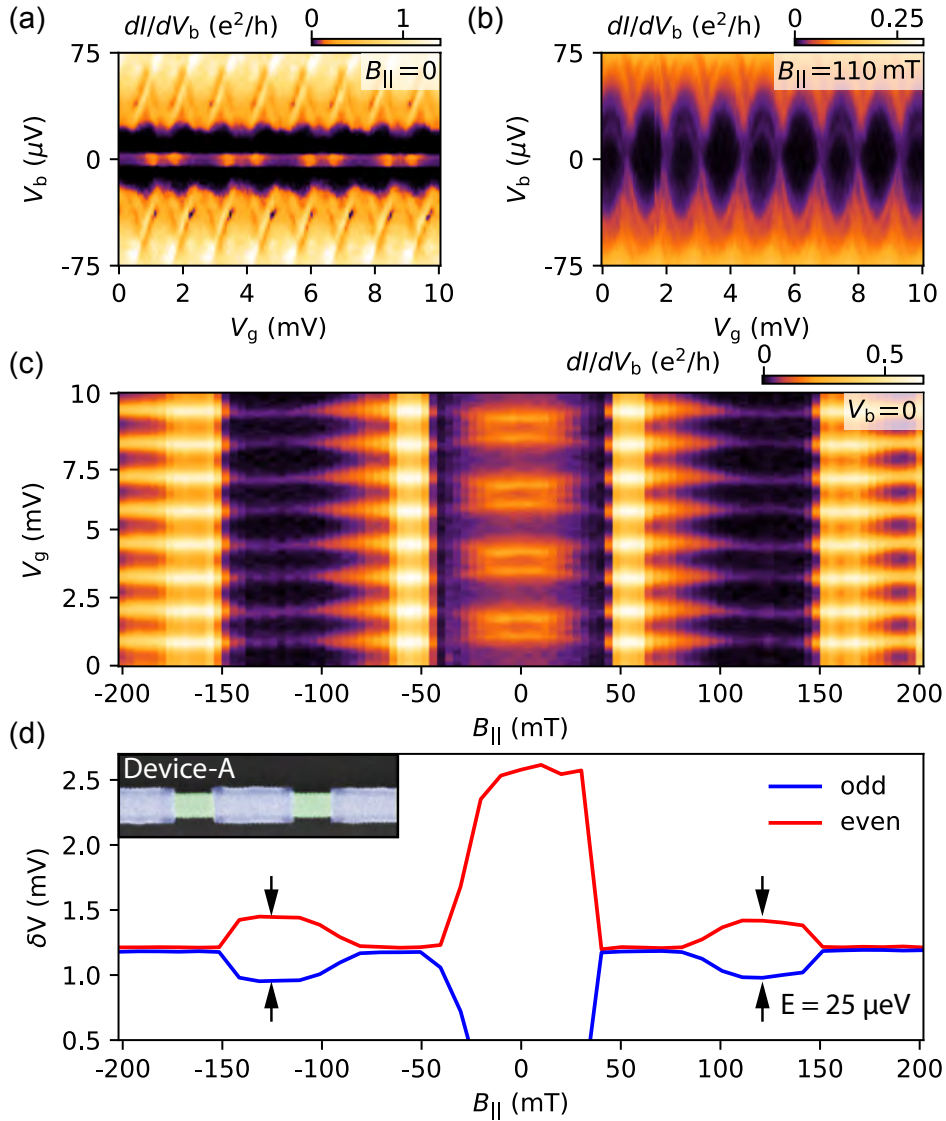
Figure 5.2: Device-A Coulomb blockade peak spacing evolution in $B_{\parallel}$. (a) Differential conductance, dI/dV_{b}, measurement of Coulomb blockade diamonds with strong even-odd effect at $V_{b} = 0$ and $B_{\parallel} = 0$. (b) Coulomb diamonds in the 1st superconducting lobe ($B_{\parallel} = 110$ mT) with finite even-odd spacing at $V_{b} = 0$. (c) Peak spacing evolution as a function of $B_{\parallel}$ at $V_{b} = 0$ with destructive regime around $B_{\parallel} = 50$ mT. (d) Peak spacing difference, δV, analysis between even and odd states as a function of $B_{\parallel}$, with finite energy splitting, $E = 25$ μeV, in δV at maximum of 1st lobe ($B_{\parallel} = 110$ mT).

5.3.1 Current-bias and phase control

Operating the interferometer device in current-bias setup is shown in
5.3(a)-(b) with reference arm still closed. Figure 5.3(a) shows differen-
tial resistance, dV/dI_b, measurement while biasing with current from
negative to positive, I_b, values as a function of charge offset, V_g, at
$B_{\parallel} = 0$. Confirmation of strong even-odd spacing now in switching cur-
rents is observed at zero field. As the axial magnetic field is increased
to $B_{\parallel} = 110$ mT, dV/dI_b measurement is taken again and it is shown in
5.3(b), where $I_b = 0$ cut in V_g reveals low resistance even-odd effect.

Turing on the interferometer, meaning setting V_1 and V_{Ref} to positive
voltages so that flux through the loop could be applied to control the
superconducting phase with flux. Figure 5.3(c) shows current-phase re-
lation while measuring differential resistance, dV/dI_b, as a function of
out-of-plane magnetic field, $B_{\perp}$, and current-bias, I_b, in the zeroth lobe
($B_{\parallel} = 0$) for fixed charge offset gate value in the *e-state*. Now setting V_g
to *o-state*, current-phase relation measurement is repeated, with *no* ob-
served phase offset compared to CPR in the *e-state*. Similar behavior is
observed at finite axial field ($B_{\parallel} = 110$ mT) and is shown in Figs. 5.3(d)-
(f), where an *absence* of a π shift is observed while changing charge
occupancy between *e-state* and *o-state*.
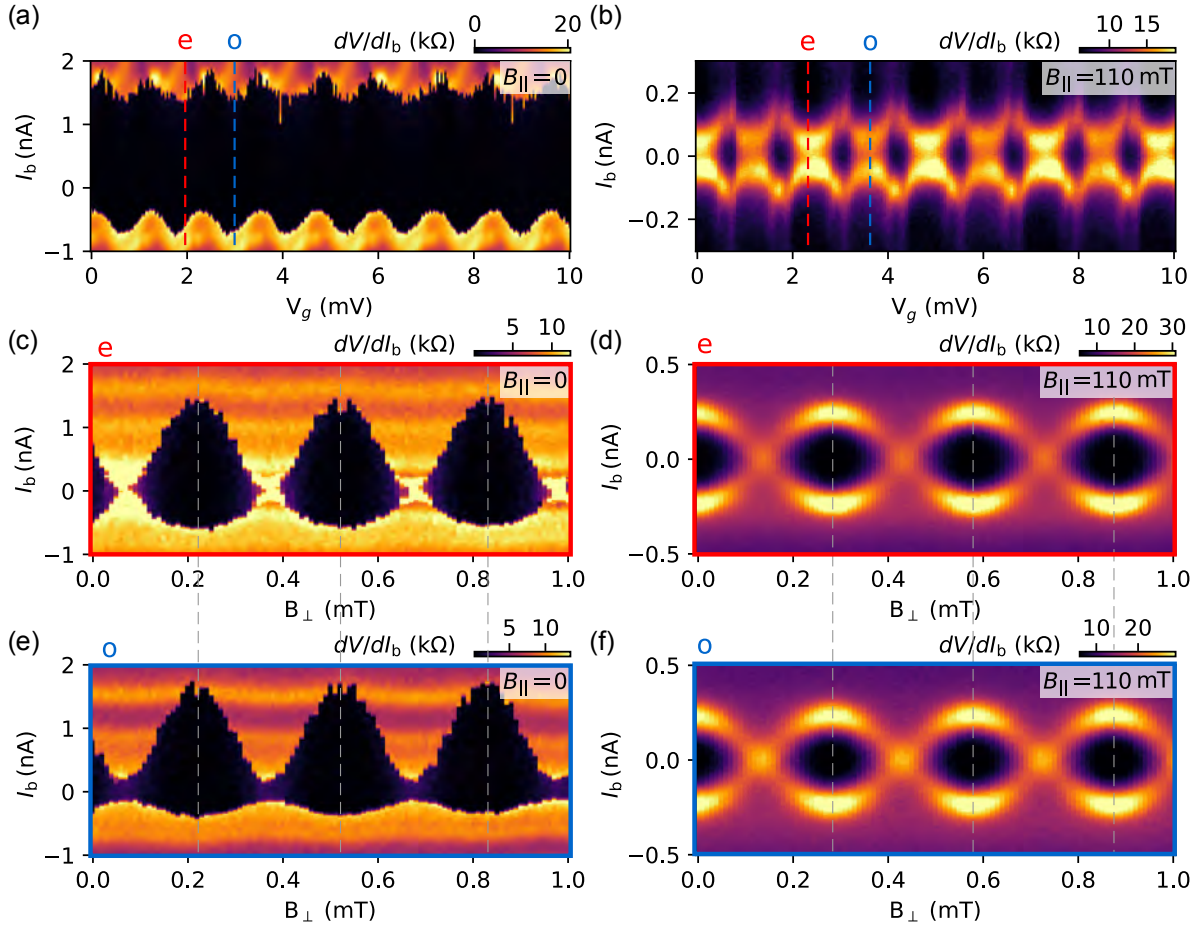
Figure 5.3: Device-A in current-bias with phase control in a Coulomb blockade. (a) Differential resistance, dV/dI_b, measurement in a Coulomb blockade with current-bias as a function of island gate, V_g at $B_\parallel = 0$. Strong seven odd spacing of switching current is seen (current biased from negative to positive values). (b) Same as (a) except done in the 1st lobe ($B_\parallel = 110$ mT), showing strong even-odd at zero current bias as a function of voltage gate, V_g. (c) Differential resistance measurement of current-bias, I_b, and out-of-plane field, $B_\perp$, with reference junction open for current-phase relationship, and voltage gate positioned in the e-state and $B_\parallel = 0$. (e) Same as (c) except positioned in the o-state. (d) Same as (c) except in the 1st lobe ($B_\parallel = 110$ mT). (f) Same as (e) except in the 1st lobe.

5.4 Device-B

S econd interferometer device-B with 700 nm island [see Fig. 5.1].
First, the interferometer left reference arm is closed and finite charging energy is subjected by using voltage-controlled gates. Figure 5.4 shows different coupling regimes in the 1st lobe. Ground-state energy dispersion is plotted for different coupling regimes where the lowest energy, E_{odd}, parabola has reached zero, representing the 1st superconducting lobe Coulomb blockaded island in the topological regime. We note that there are two distinct coupling regimes between the island and the left lead. We plot the energy dispersion for strong and weak couplings in Fig. 5.4(a)-(b), respectively. With voltage-controlled gate, V_L, positioned in a strong coupling regime we observe a double amount of Coulomb peaks of that expected in the topological regime. In Fig. 5.4(a), the usual expectation of Coulomb peaks ar highlighted in green circles, whereas the unusual extra peaks are highlighted in red/blue circles, for even and odd parabola degeneracy points, respectively. As the V_L voltage gate is set in the weak coupling regime, the following energy dispersion is plotted in 5.4(a), with only the green points visible, highlighting the conventional $1e$ peaks.

Differential conductance measurement is taken in a strong coupling regime in a Coulomb blockaded island in Fig. 5.4(c), at $V_b = 0$ as a function of charge offset ,V_g. Two distinct peak heights are observed and we associate the lower conductance peaks with green degeneracy points in 5.4(a). The higher conductance peaks are associated with red/blue degeneracy points. In the weak coupling regime, dI/dV is taken again at $V_b = 0$ as a function of V_g, where only green points in energy dispersion are visible in Fig. 5.4(d). In panels Fig. 5.4(e)-(f), dI/dV measurement shows the evolution of Coulomb peaks as a function of axial-magnetic field, $B_\parallel$. In both panels at $B_\parallel = 0$, the island is charged by $2e$ as the field is increased the peaks split in even-odd spacing, and for Fig. 5.4(e) (strong coupling regime) extra bright peaks, red/blue circles appear throughout the 1st lobe, whereas in Fig. 5.4(e) (weak coupling regime) only low conductance green circle peaks appear. We note that this unusual appearance of extra Coulomb peaks appear in the 1st lobe, to highlight it, out-of-plane magnetic field was applied to drive
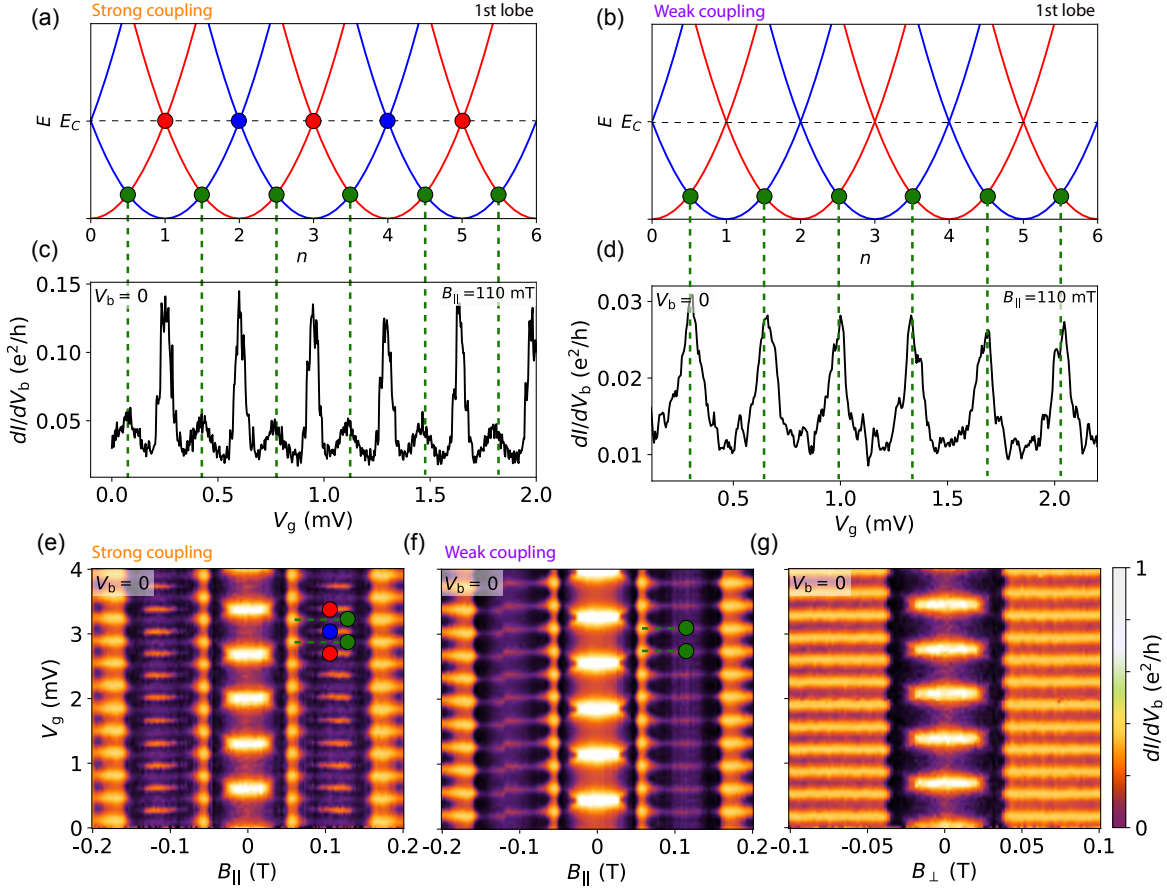
Figure 5.4: Device-B Coulomb peak spacing evolution in $B_\parallel$ with energy dispersion parabolas. (a) Energy parabolas as a function of charge offset, N_g, in a Coulomb blockaded island with smaller charging energy E_C compared to finite superconducting gap Δ (Equivalent to B=0). Degeneracy points (red) indicate $2e$ electron transport in the ground state. (b) Energy parabolas for $\Delta < E_C$ (Equivalent to increased $B_\parallel$). Degeneracy points (green) indicate even-odd electron transfer. (c) Parabolas represents the topological regime with green degeneracy points of $1e$ electron transport with addition strong coupling signatures of red/blue degeneracy points indicating poisoning effect. (d) Same as (c) except in the weak coupling regime with an absence of red/blue degeneracy points. (e) Differential conductance, dI/dV_b, measurement of $B_\parallel$ evolution at zero-bias, $V_b = 0$, as a function of voltage gate in the strong coupling regime. (f) Same as (e) except in the Weak coupling regime. (g) Conductance measurement as a function of out-of-plane field, $B_\perp$, and gate voltage.

the leads and the island to the normal state where the conventional $2e$ to $1e$ transition appears [see Fig. 5.4(g)]

We further study these unusual coupling regimes at $B_\parallel = 110$ mT for different tunneling barrier voltages on V_L in Fig. 5.5. dI/dV measurement at $B_\parallel = 110$ mT and $V_b = 0$ as a function of charge offset on
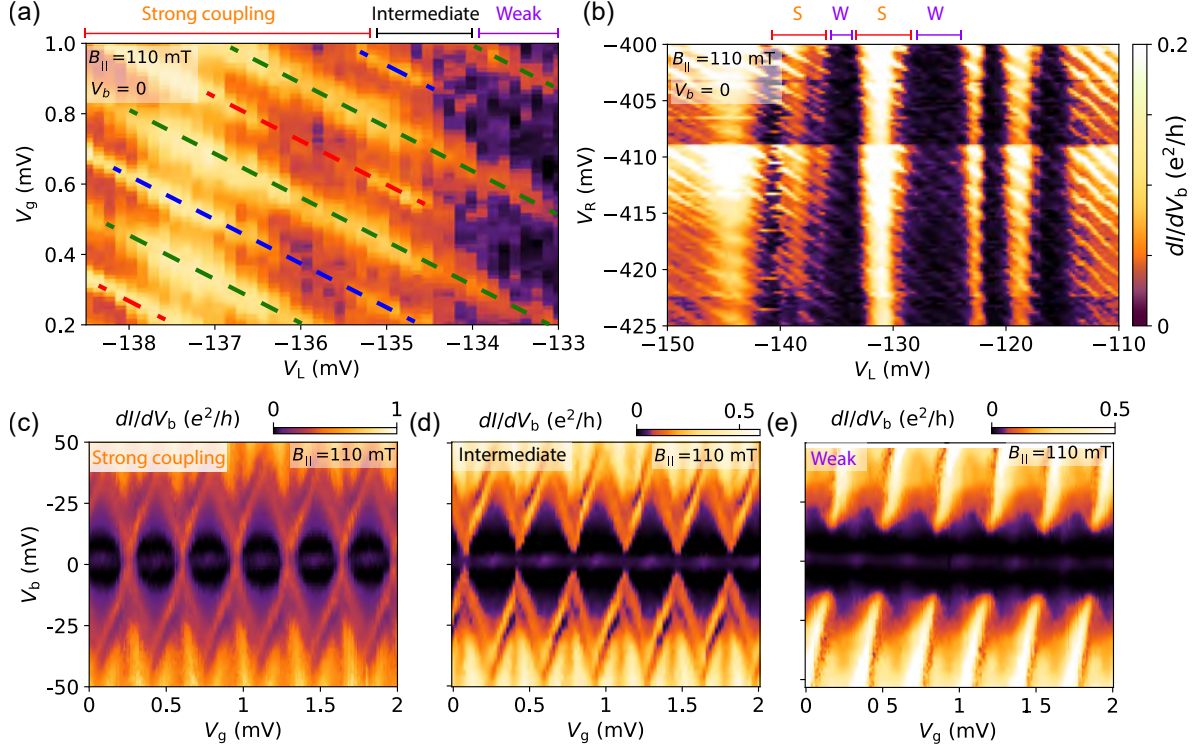
Figure 5.5: Strong and weak coupling regime tuning in the 1st lobe for Device-B. (a) Differential conductance, dI/dV_b, measurement in a Coulomb blockade as a function barrier voltage gate, V_L, and gate voltage V_g at zero-bias, V_b in the 1st lobe. Strong and weak coupling regimes are indicated. Strong coupling regime having double the Coulomb peaks compare to weak coupling. (b) Two barrier conductance measurement in the 1st lobe indicating strong and weak coupling regimes as the V_L voltage gate is changed. (c) Coulomb blockade diamonds in the strong coupling regime in at $B_{\parallel} = 110$ mT. (d) Same as (c) except in the intermediate coupling regime. (e) Same as (c) except in the weak coupling regime.

the island, V_g, and tunneling barrier V_L is shown in Fig. 5.5(a), where we identify three regimes: strong, intermediate, and weak couplings as the barrier voltage is changed. The color dashed lines represent degeneracy points in 5.4(a)-(b) circles. Two barrier gate, V_L and V_R, dI/dV map is shown in 5.5(b), where $V_b = 0$ and $B_{\parallel} = 110$ mT. We note big conductance resonances occurring as V_L is changed and at these points, we associate the strong coupling regimes, whereas in between we note the weak coupling regime. Panels (c)-(e) in Fig. 5.5(a) show Coulomb blockade diamonds for different couplings. For strong couplings, the high conductance peaks are the diamonds crossing zero bias and fain peaks are in between [(c)]. As the coupling is reduced the diamonds
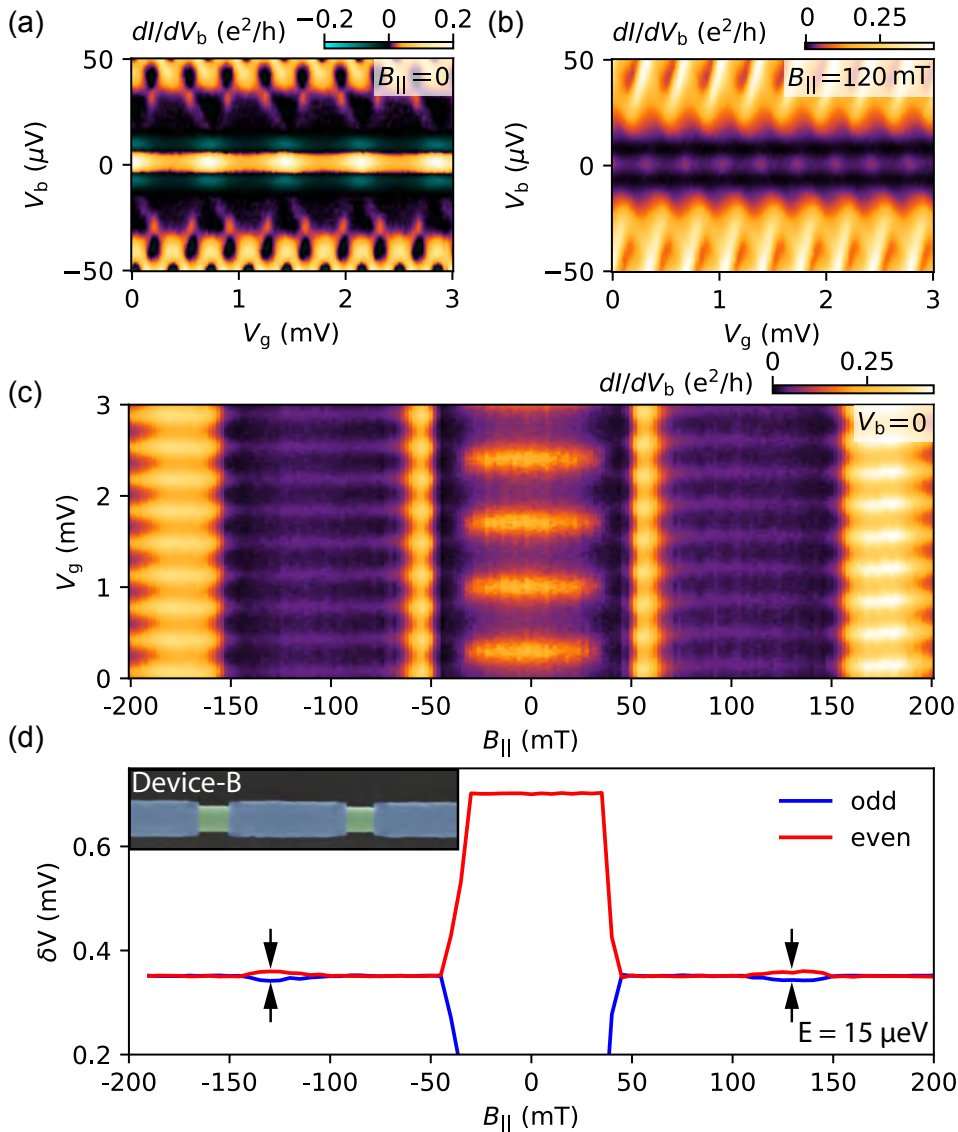
Figure 5.6: Device-B in weak coupling regime with Coulomb blockade peak spacing evolution in $B_\parallel$. (a) Differential conductance, dI/dV_b, measurement of Coulomb blockade diamonds with 2e charge Coulomb peaks at $V_b = 0$ and $B_\parallel = 0$. (b) Coulomb diamonds in the 1st superconducting lobe ($B_\parallel = 120$ mT) with almost perfectly 1e spaced peaks at $V_b = 0$. (c) Peak spacing evolution as a function of $B_\parallel$ at $V_b = 0$ with destructive regime around $B_\parallel = 50$ mT. (d) Peak spacing difference, δV, analysis between even and odd states as a function of $B_\parallel$, with finite energy splitting, $E = 15$ μeV, in δV at maximum of 1st lobe ($B_\parallel = 120$ mT).

move away from zero bias and only faint peaks are visible at zero bias [(d)]. For even smaller coupling regimes, diamonds move away even further from zero energies, leaving faint 1e supercurrent peaks [(e)].

In the weak coupling regime peak spacing analysis is done as a function axial magnetic field, $B_\parallel$. In Fig. 5.6(a) Differential conductance measurement of Coulomb blockade diamonds at $B_\parallel = 0$ show $2e$ peak spacing at $V_b = 0$. The same Coulomb diamonds are taken in the 1st lobe ($B_\parallel = 120$ mT) shown in Fig. 5.6(b), with discrete $1e$ spaced peaks. To highlight peak evolution in field, we set $V_b = 0$ and measure dI/dV as a function of $B_\parallel$ and charge offset on the island with voltage-controlled gate, V_g [see Fig. 5.6(c)]. The same peak spacing analysis is done here by fitting multiple peaks to Lorentzian fit to extract peak spacing and it is shown in 5.6(d), with finite even-odd spaced peak splitting converted to energy $E = 15\mu$eV in the 1st lobe. These results compare to recently reported finite topological full-shell islands [70].

5.4.1 Current-bias and phase control

Finally, we investigate the device in current-bias and with closed reference arm, by setting voltage gates V_1 and V_{Ref} to very negative values. Figure 5.7(a) shows differential resistance measurement, dV/dI, as a function of applied current-bias and charge offset, V_g at $B_\parallel = 0$. From switching currents, the $2e$ periodicity of the island can be inferred. By setting axial-magnetic field at $B_\parallel = 120$ mT, dV/dI measurement of Coulomb island is shown in 5.7(b), with switching current suggesting $1e$ periodicity.

With opened reference arm, phase control of the Coulomb island is done in Fig. 5.7(c) for *e-state* that is shown in (a), at $B_\parallel = 0$, by changing the out-of-plane magnetic field ($B_{\perp]}$). Figure 5.7(e) shows the same differential conductance measurement except done in *o-state*, with no clear phase shift between two charge states. We note that for 700 nm island and at $B_\parallel = 0$ we only observed $2e$ spaced coulomb peaks, therefore we emphasize that the convention used as *e/o* does not reflect the charge number on the island. In Figs. 5.7(d)-(f) the same phase scan are taken except now in the 1st lobe ($B_\parallel = 120$ mT), for two different charge states (*e-state* and *o-state*), with again no clear phase difference between the two.
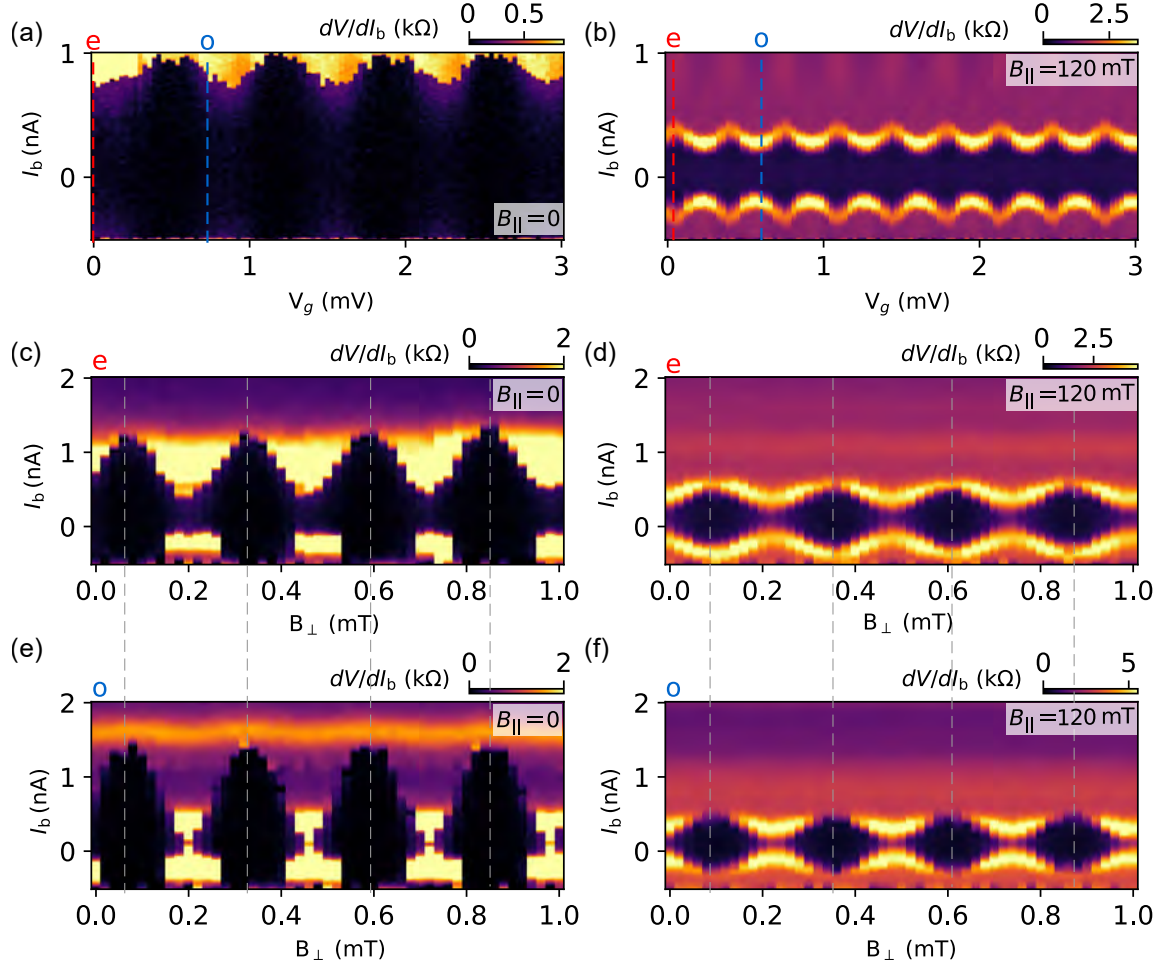
Figure 5.7: Device-B in Current-bias with phase control in Coulomb blockade. (a) Differential resistance, dV/dI_b, measurement in a Coulomb blockade with current-bias as a function of island gate, V_g at $B_\parallel = 0$. $2e$ spaced switching current is seen as a function of gate voltage, V_g, (current biased from negative to positive values). (b) Same as (a) except done in the 1st lobe ($B_\parallel = 110$ mT), showing double switching current peaks compared to zeroth lobe as a function of voltage gate, V_g. (c) Differential resistance measurement of current-bias, I_b, and out-of-plane field, $B_\perp$, with reference junction open for current-phase relationship, and voltage gate positioned in the e-state and $B_\parallel = 0$. (e) Same as (c) except positioned in the o-state. (d) Same as (c) except in the 1st lobe ($B_\parallel = 110$ mT). (f) Same as (e) except in the 1st lobe.

5.5 Conclusions

In summary, we have investigated topological islands embedded into an interferometer. Coulomb peak spacing evolution as a function of axial magnetic field suggest discrete zero energy state with energy splitting comparable to previously investigated Majorana islands in full-shell Al nanowires [70]. Current-phase relation of topological islands showed no π shift for different charge occupancy for both investigated islands, where theoretical prediction is in agreement to our observations, that no phase shift is expected [91, 93].

6

RADIO-FREQUENCY METHODS FOR MAJORANA-BASED QUANTUM DEVICES

This chapter explores radio frequency methods (RF) that are applied to semiconductor-superconductor nanowire systems designed to probe Majorana zero modes. Two approaches are presented: In the first, hybrid nanowire-based devices are part of a resonant circuit, allowing conductance to be measured as a function of several gate voltages $\sim$40 times faster than using conventional low-frequency lock-in methods. In the second, nanowire devices are capacitively coupled to a nearby RF single-electron transistor made from a separate nanowire, allowing RF detection of charge, including charge-only measurement of the crossover from $2e$ inter-island charge transitions at zero magnetic field to $1e$ transitions at axial magnetic fields above 0.6 T, where a topological state is expected. Single-electron sensing yields signal-to-noise exceeding 3 and visibility 99.8% for a measurement time of 1 μs.

6.1 Introduction

Solid-state quantum computation schemes that involve repeated measurement and feedback, including topological schemes [52, 53, 109, 110] with potentially long coherence times [50, 51], nonetheless require fast read-out of charge or current in order to operate on reasonable time scales [111]. For topological qubits based on Majorana modes in nanowires (NWs) with proximity-induced superconductivity, quasiparticle poisoning of Majorana modes constrains read-out times to microseconds or faster [112], as has already been demonstrated for superconducting [113–116] and spin qubits [117–120].

Here, we report the realization of radio-frequency (RF) reflectometry in various configurations of InAs nanowires (NWs) with epitaxial Al, fabricated to form single or coupled Majorana islands, with and without proximal NW charge sensors. The device geometries are inspired by recent theoretical proposals for demonstrating elementary topological qubit operations in these systems [52, 53, 109, 110]. Two approaches to fast measurements are investigated in detail. In the first, a resonator made from a cryogenic inductor and capacitor is coupled directly to the leads of the device [121–123], providing a conductance measurement similar to what is obtained with a low-frequency (LF) lock-in amplifier, though considerably faster. In the second, a similar resonator is capacitively coupled to a proximal NW charge sensor configured for both LF and RF charge read-out. The overall charge sensitivity is investigated as a function of the measurement time and is found to yield a signal-to-noise ratio (SNR) for single-charge detection exceeding 3 and a visibility of 99.8% for an integration time of 1 μs, with correspondingly higher values for longer integration times. Proximal NW charge sensors are found to be compatible with magnetic fields exceeding 1 T, the range needed to reach the topological regime [57–59, 62]. All measurements are carried out in a dilution refrigerator (Oxford Instruments Triton 400) a base temperature of approximately 20 mK, equipped with a 6-1-1 T vector magnet.

6.2 Experimental setup and techniques

The reflectometry signal is optimized by matching the circuit impedance Z, including the device resistance, R_{dev}, to the characteristic impedance of the transmission line, $Z_0 = 50\,\Omega$. Near matching, the reflection coefficient of the resonant circuit:

$$\Gamma = \frac{Z - Z_0}{Z + Z_0},\tag{6.1}$$

where it is sensitive to small changes in R_{dev} [124, 125]. To enable multiple simultaneous measurements, four RF resonant circuits with different discrete inductances in the range $L = 1.2$ - 4.7 μH are coupled to a single-directional coupler via a coupling capacitor, C. One such resonant circuit is depicted in Fig. 6.1(a). It consists of a ceramic-core chip inductor [126], a parasitic capacitance, C_P, from bond wires and on-chip metal electrodes, and the device, with R_{dev} tuned by the gate voltages. The parasitic capacitance is found to be unchanged over several cooldowns.

Low-frequency (LF) lock-in measurements of differential conductance $g = \mathrm{d}I/\mathrm{d}V|_{V_{bias}}$ of either the device or the sensor are carried out in a two-wire voltage-bias configuration using a transimpedance (current-to-voltage) amplifier [127] connected to the drain of the device, providing voltage input to a lock-in amplifier (Stanford Research SR830). The voltage bias consists of a dc component, V_{bias}, and a LF component in the range of 4 - 10 μV at frequencies below 200 Hz.

Reflectometry measurements of either the device or the sensor are performed as follows. A RF carrier at frequency f with amplitude V_{TX} is applied to the source lead following a series of attenuators at various temperature stages [Fig. 6.1(a)], giving a total of 21 dB of attenuation, with an additional 15 dB of attenuation from the directional coupler, mounted below the mixing chamber plate. After reflection from the device, the signal passes back through the directional coupler into a cryogenic amplifier (Caltech CITLF3; noise temperature T_n = 4 K from 10 MHz to 2 GHz) with +40 dB of gain. The output signal, V_{RX}, is then detected using one of three methods: (1) using a network analyzer to measure $S_{21} \equiv 20\log(V_{RX}/V_{TX})$ [Fig. 6.1(c)]; (2) using discrete analog components to demodulate by standard homodyne detection, followed
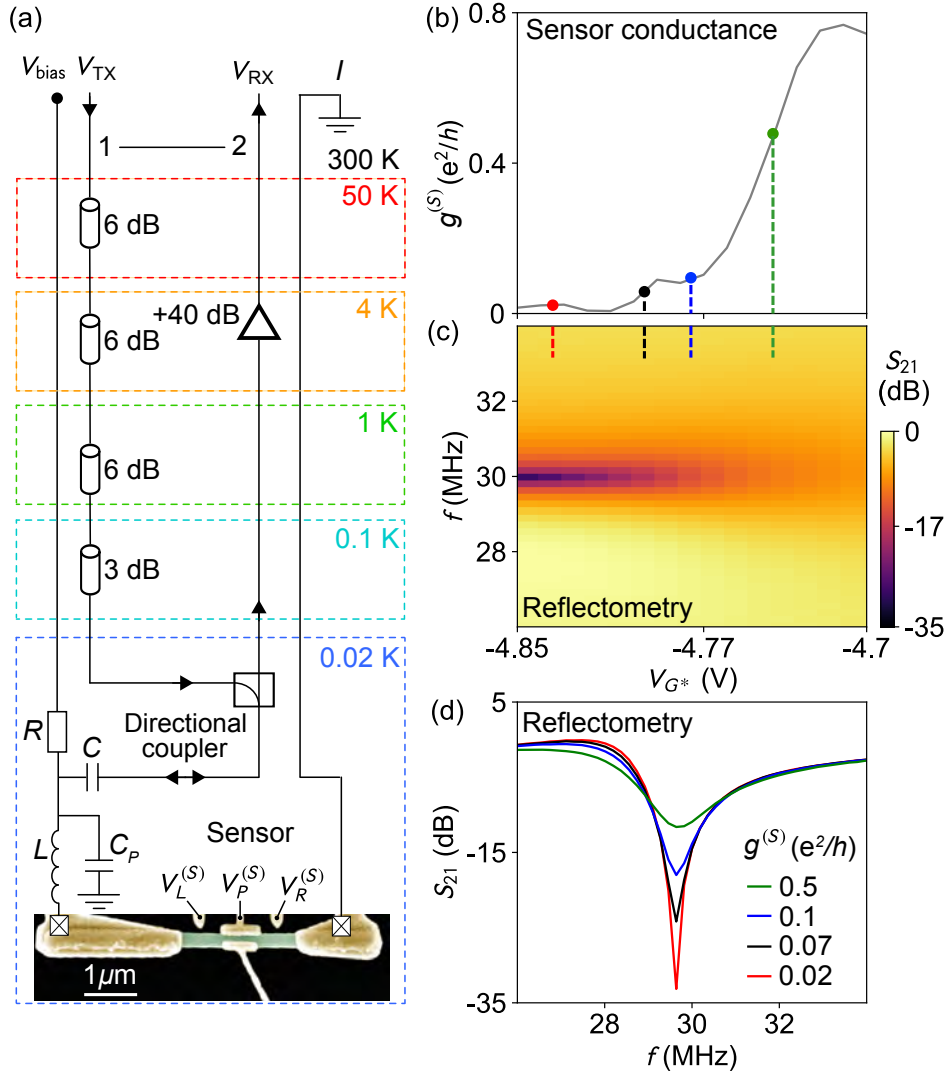
Figure 6.1: The rf charge-sensing setup. (a) A circuit diagram of a nanowire (sensor) embedded in a resonant circuit allowing conductance by measuring current $I(V_{\text{bias}})$ or reflectometry measurement (by measuring reflected signal V_{RX}), respectively (see the main text). (b) The sensor conductance, $g^{(S)}$, as a function of the sensor gate voltage, $V_{G*} = V_L^{(S)} = V_P^{(S)} = V_R^{(S)}$. (c) The scattering parameter, S_{21}, as a function of the carrier frequency f, and V_{G*} acquired simultaneously with (b). $S_{21}(f)$ develops a dip at $f_{\text{res}} \sim$ 30 MHz, indicating that the matching condition of the resonator is approached toward low sensor conductance. (d) Vertical cuts of (c) for the gate voltages indicated in (b). The on-resonance reflectometry signal acts as an alternative measure of $g^{(S)}$.

by a fast-sampling oscilloscope (for details see Appendix D); (3) using a RF lock-in amplifier (Zurich Instruments UHFLI [128]). Each method has its advantages. Method (1) is convenient for quickly determining if a change in device resistance has an effect on the circuit impedance, which shows up as a change in the magnitude of S_{21}. Method (2) provides fast acquisition of phase maps at different gate configurations, particularly if the device is tuned into the regime of small charging energies. For these applications, methods (2) and (3) are comparable. Method (3) has advantages in simultaneously measuring the phase and magnitude of the reflected signal and is used to quantify SNR of the proximal NW sensors and to detect charge occupancy of Majorana islands tuned to low barrier transmission.

Figure 6.1(b-d) show a comparison of the LF lock-in measurement and the reflectometry measurement, $S_{21}(f)$, of conductance $g^{(S)}$ of a charge sensor as it is pinched off using electrostatic gates. In the reflectometry measurement, V_{RX} varies rapidly near the resonance frequency $f_{res} \sim 30$ MHz, yielding a dip in $S_{21}(f)$ that depends on the common gate voltage. Line cuts of S_{21} at different values of V_{G*} are shown in Fig. 6.1(d). The depth of the resonance changes by approximately 21 dB as the sensor conductance, $g^{(S)}$, is decreased from 0.5 e^2/h to 0.02 e^2/h. In this case, an increasing R_{dev} moves the resonator impedance toward matching.

6.3   Conductance: LF lock-in versus RF reflectometry

Figure 6.2(a) shows a hybrid InAs/Al island (device A) defined by Ti/Au gates that wrap around the NW, isolated by HfO$_2$ dielectric. Al is removed from the NW ends with wet etch leaving a continuous Al segment, where gates L and R set the boundaries of the island. Gate voltages V_L and V_R control coupling of the island to the leads, while three additional gates tune the chemical potential and density on different parts of the island. Only the gate marked V$_{LP}$ in Fig. 6.2(a) is used, with the others fixed at zero volts. A dc voltage V_{bias} is applied to the left lead, while the right lead is connected to the rf circuit (L = 2.7 μH, f_{res} $\sim$ 52 MHz) using method (2), described above. Simultaneous LF and rf measurements of the pinch-off characteristic of the right barrier with the left barrier fixed at $V_L \sim 1$ V are shown in Fig. 6.2(b). At positive
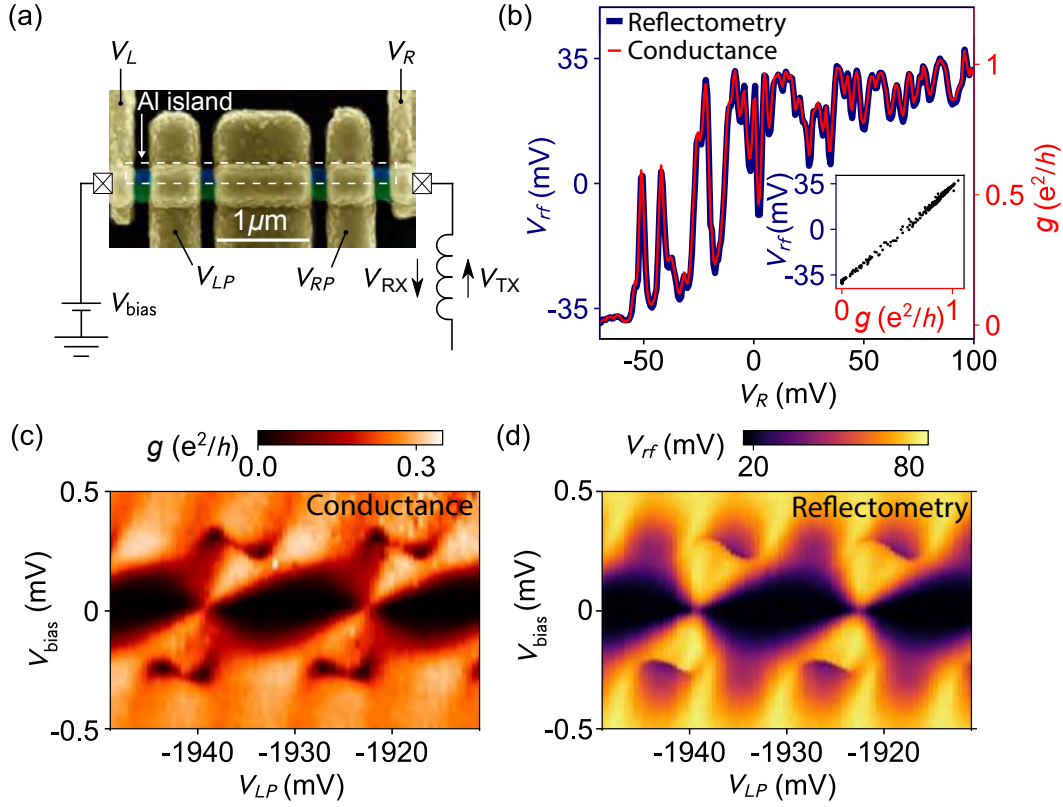
Figure 6.2: Conductance via lock-in versus lead reflectometry. device A. (a) A scanning electron micrograph of a top-gated InAs/Al nanowire device with the relevant gates labeled. The dashed white box indicates the Al island. (b) The zero bias pinch-off characteristic of the right barrier gate, V_R, as measured by conductance (red) and reflectometry (blue). The inset shows a parametric plot of the two traces. The coulomb-blockade diamonds are measured by conductance (c) and reflectometry (d). In both cases, the dependence on the plunger voltage V_{LP} is $1e$ periodic at high bias and $2e$ periodic at zero bias.

V_R, the right-hand side of the island is open and shows a positive de-modulated voltage V_{rf}, while at negative V_R, the right junction is closed and no current can flow through the island. Overall, V_{rf} is found to be proportional to g measured with an LF lock-in, as shown in the inset of Fig. 6.2(b).

Setting both barriers into the tunneling regime using V_L and V_R creates a Coulomb-blockaded island. A two-dimensional (2D) map of Coulomb diamonds as a function of V_{bias} and the left plunger gate, V_{LP}, is shown in Fig. 6.2(c,d). At finite bias, $V_{bias} \geq 0.2$ mV, above the super-conducting gap of Al, conductance oscillations with a period of half the

zero-bias period are found, characteristic of a superconducting island. At low bias, transport is via Cooper pairs, yielding 2e periodicity; at biases above the superconducting gap, 1e transport is available, halving the period.

6.4 Lead reflectometry

The similarity of the LF lock-in and RF reflectometry data exhibited in Figs. 6.2(c,d) indicates that RF reflectometry yields essentially equivalent results to LF conductance, although with a dramatic reduction of data-acquisition time. For instance, a 2D map of V_L versus V_{LP} consisting of 3000 × 1500 points [see Fig. 6.3] requires roughly 1 hour of acquisition time, including data processing. The acquisition of comparable data using LF lock-in methods with a 30 ms integration time would require 1500 × 3000 × 30 ms ∼ 38 hours to achieve a comparable SNR and resolution.
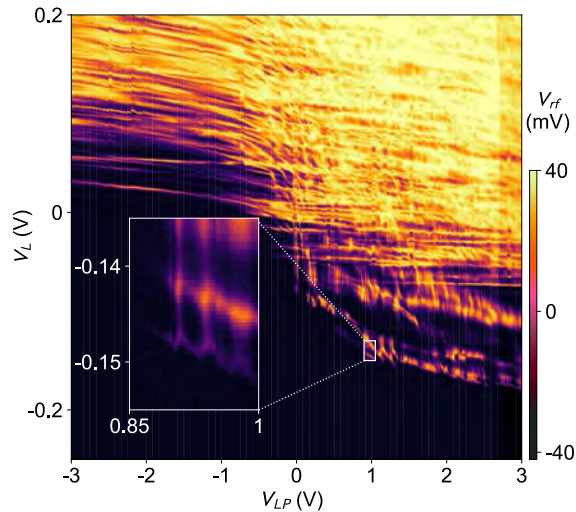
Figure 6.3: Fast high-resolution charge sensing measurement using lead reflectometry. Gate voltage map of left cutter, V_L, versus plunger gate, V_P, acquired with the lead sensing method in 1 h. The estimated time of to complete a 2D gate-gate measurement with comparable resolution using a conventional lock-in with 30 ms time constant would be ∼ 40 h.

6.5 Charge sensing

The charge sensing of a Majorana island is accomplished by placing a second NW (sensor wire), without a superconducting layer, next to the hybrid-NW Majorana device, and capacitively coupling the two NWs with a floating metallic gate [129]. Charge sensing complements conductance and is the basis of parity read-out in several theoretical proposals (e.g., Ref. [52]). The approach is similar to schemes used for spin qubit read-out [130–132]. In the context of topological qubits, one can generalize the idea used in spin qubits known as "spin-to-charge conversion," where a well-isolated quantum variable (spin) is read out projectively by mapping the relevant qubit state onto charge and then detecting charge [119, 120]. In a similar way, the parity of a Majorana island grounded via a trivial superconductor, a well-isolated quantum state, can be read out projectively as a charge state if the island is gated into isolation, forming a topological Coulomb island [52], a process that we denote *parity-to-charge conversion*.

6.5.1 Low frequency

A Majorana island formed from a gated segment of InAs/Al that gates L and R encapsulate, with extended leads made from the same wire (device B), is shown in Fig. 6.4(b). Regions with tunable carrier density and conductance, made by removing the Al shell, are aligned with electrostatic gates deposited in a subsequent lithography step. Local depletion of the charge carriers in these regions (tuned by gates L and R) creates two superconductor-insulator-superconductor tunnel junctions with a semiconductor-superconductor island in between. A T-shaped floating gate couples the superconducting island to the charge sensor NW, which was operated in the Coulomb blockade regime by depleting its barriers with gate voltage $V_L^{(S)}$ and $V_R^{(S)}$.

Low-frequency lock-in measurement of conductance through the InAs/Al NW island as a function of V_{bias} and compensated gate voltage V_P^* is shown in Fig. 6.4(a). Compensation means that whenever the device plunger voltage V_P is swept, the sensor plunger $V_P^{(S)}$ is also varied to prevent V_P from affecting the sensor charge state via capacitive
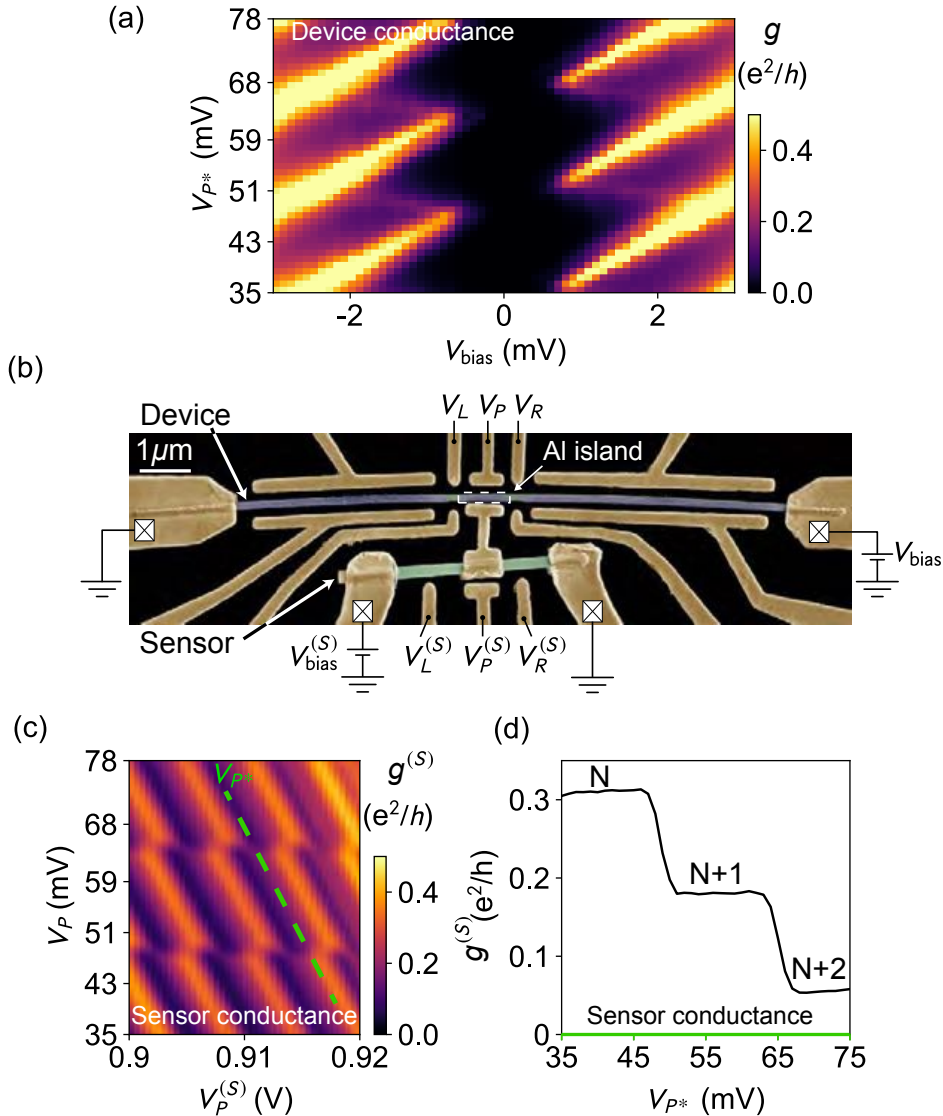
Figure 6.4: The charge sensing of a superconducting island using lock-in measurement of a remote charge sensor. device B. (a) Conductance through the InAs/Al nanowire device [blue in (b)] as a function of the bias voltage, V_{bias}, and the compensated plunger voltage, V_P^* (for explanation of compensation, see main text). (b) A false color scanning electron micrograph of a device with the relevant gates labeled. A T-shaped Ti/Au floating gate couples the superconducting island (white dashed box) (device) to a bare InAs nanowire (Sensor). (c) Sensor conductance $g^{(S)}$ at $V_{bias} = 0$, as a function of $V_P^{(S)}$ and V_P. (d) Cut along the green dashed line in (c). Distinct constant-conductance-value plateaus are indicated by the associated electron occupation of the Majorana island.

coupling, allowing the sensor to remain on a single Coulomb peak as V_P^* is swept. Compensation is illustrated in Fig. 6.4(c), where the green dashed line shows a compensated trajectory through the space of the two plunger voltages.

Coulomb blockade diamonds are visible in Fig. 6.4(a). The suppression of conductance for $|V_{\text{bias}}| < 0.4$ mV, independent of V_P^*, reflects the presence of a superconducting gap in both leads, and is consistent with the gap of Al, assuming the induced gap $\Delta_I \sim 0.2$ meV is roughly equal in the three NW segments. Charging energy $E_C \sim 0.7$ meV was extracted from Coulomb diamonds of Fig. 6.4(a). The large charging energy, $E_C/\Delta_I > 1$ is consistent with suppressed conductance of Cooper pairs at $V_{\text{bias}} = 0$ [133–135]. The large E_C results from the small capacitance between device island and the metal back-gate due to thick (500 nm) SiO_2. By comparison, device A had 200 nm of SiO_2, reducing the charging energy to below the induced gap, leading to $2e$ Cooper-pair transport between Coulomb valleys.

The sensor conductance, $g^{(S)}$, at zero DC bias, $V_{\text{bias}}^{(S)} = 0$, as a function of plunger gate voltages $V_P^{(S)}$ and V_P, is shown in Fig. 6.4(c). Conductance oscillations along the $V_P^{(S)}$ axis indicate that the sensor island is tuned into the Coulomb blockade regime, whereas discontinuities along V_P reflect charge transitions in the main hybrid device. We emphasize that charge transitions are *not visible* in zero-bias conductance of the device [Fig. 6.4(a)] but *are visible* as plateaus in sensor conductance $g^{(S)}$ as the device charge changes by two between adjacent Coulomb valleys [Fig. 6.4(c,d)].

6.5.2 Radio frequency

A double-Majorana-island (white dashed boxes indicate Al islands) device motived by Ref. [52] (device C) is shown in Fig. 6.5(a). Near the main device, two bare InAs NWs, capacitively coupled to each of the islands via floating gates, serve as independent charge sensors of the two islands. Each sensor is part of an independent RF circuit, with $L_1 = 3.3$ μH ($f_{\text{res}} \sim 60$ MHz) and $L_2 = 4.7$ μH ($f_{\text{res}} \sim 40$ MHz). Data acquisition used method (3), described above. Gates V_L, V_M, and V_R were each set to the tunneling regime. Voltages applied to plunger gates *LP* and *RP*
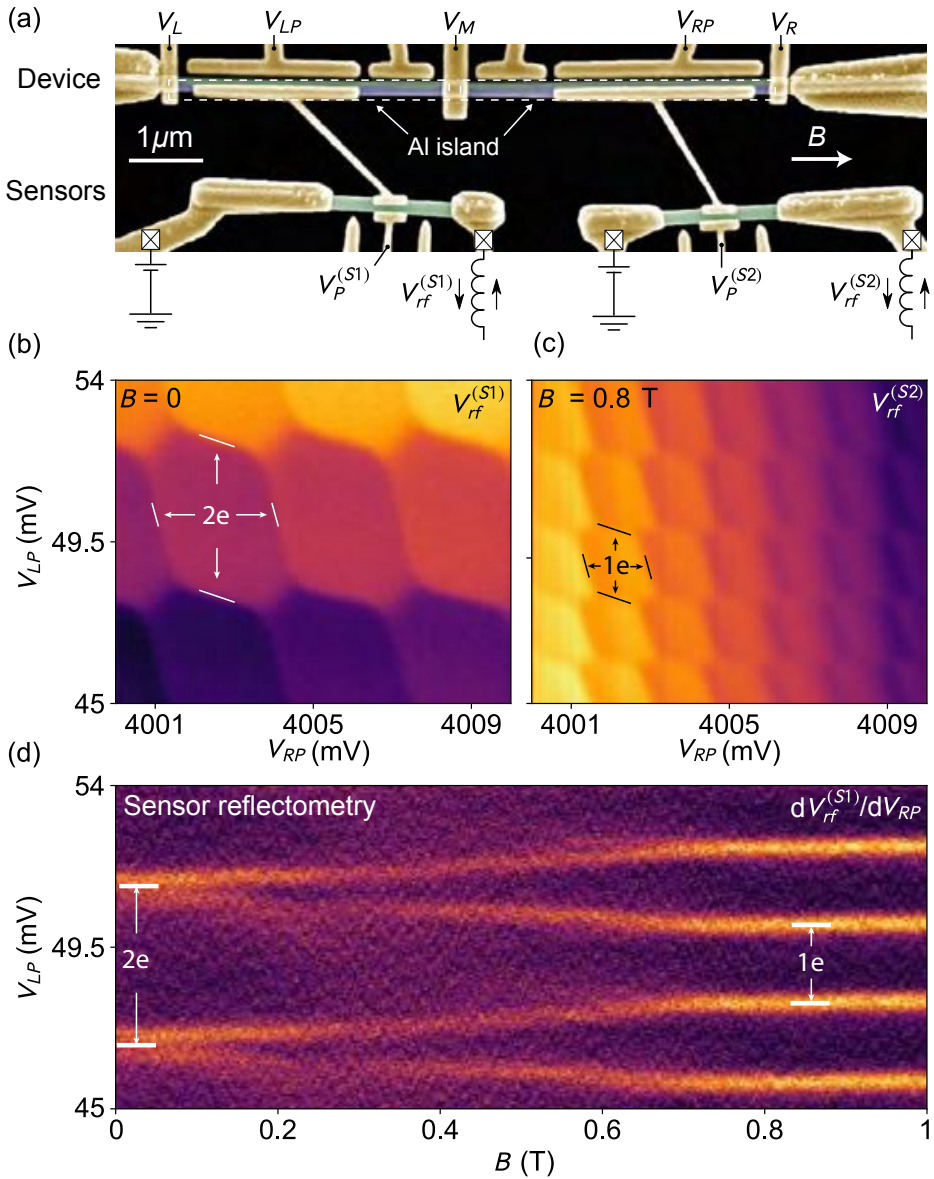
Figure 6.5: RF charge sensing of double Majorana island. device C. (a) Scanning electron micrograph of the device measured (white dashed boxes indicate Al islands). Voltage tunable tunnel barriers are labeled as V_L, V_M and V_R. Island plunger gates are labeled as V_{LP} and V_{RP} for the left and right island respectively. (b) $2e$-$2e$ periodic superconducting double-island charge stability diagram measured at $B = 0$ by RF charge sensing with a right sensor. (c) $1e$-$1e$ periodic double-island charge stability diagram measured at $B = 0.8$ T with a left sensor. (d) Charge occupancy of the right island (controlled by V_{RP}) evolution as a function of B. The color map shows the measured RF demodulated signal from the right sensor ($V_{rf}^{(S2)}$) and is differentiated along the V_{RP} axis. Periodicity change from $2e$ to $1e$ in V_{RP} direction is observed as B is increased.

affect both the carrier density in the semiconductor and the charge offset of each island. Fig. 6.5(b) shows the charge sensing signal of a 2e-2e periodic superconducting double-island at $B = 0$, measured using the right charge sensor (S2), with a plane subtracted to remove cross-coupling of the plungers to the three barrier gates, V_L, V_M and V_R. Periodic 1e-1e double-island plane-fitted data, measured using the left charge sensor (S1) at finite magnetic field ($B = 0.8$ T) parallel to NW axis, is shown in Fig. 6.5(c). A hexagonal pattern, characteristic of a double-island devices, is readily seen at both zero field and $B = 0.8$ T [Fig. 6.5(b,c)]. Magnetic field B evolution of the right 2e periodic island into the 1e periodic island regime, with the left island tuned into a Coulomb valley, is shown in Fig. 6.5(d). The data is differentiated along V_{LP} to improve visibility of the charge transitions.

Previous works [57, 136] investigated nearly 1e periodic island charge occupancy, consistent with an emerging topological phase, using conductance. Using reflectometry and charge instead has the advantage of not require electron transport through the device itself. As seen from Fig. 6.5(d), sensing is consistent with these previous transport studies [57]. We will not focus on peak spacing and motion here, to keep the focus on measurement methods.

6.5.3   *Fast charge measurement and signal-to-noise ratios in 1*e *regime*

The signal-to-noise ratio (SNR) for detecting the transfer of a single electron between islands of the double-island device in Fig. 6.5(a) was investigated as a function of measurement time using the pulsed gate sequence shown in Fig. 6.6(a). Measurements were done in an applied axial magnetic field $B = 0.6$ T, where the charge-stability diagram shows 1e-1e hexagons. However, in contrast to the tuning in Fig. 6.5(c), V_L and V_R were set to isolate the double-island, with negligible coupling to the source and drain. Only inter-island transitions [white and red dashed lines in Fig. 6.6(a)] were measurable in this configuration.

A cyclic pulse sequence was applied to gates LP and RP using an arbitrary waveform generator (Tektronix 5014c), placing the system in three configurations, Initialization (I) for 150 μs, Preparation (P) for 200 μs, and Measurement (M) for a range of times from 1 μs to 50 μs [see Fig. 6.6(a) inset]. The preparation position and duration were chosen

to yield roughly equal populations of relaxed and exited populations, which also depended sensitively on the inter-island barrier gate voltage, V_M. Results of the measurement, integrated over the measurement time, were then binned to form histograms showing the distinguishability of N and $N+2$ charge-difference states ($N = N_L - N_R$ is the charge difference, where N_L and N_R are the occupancies of the left and right islands). Note that the number of cycles used to gather histogram statistics does not affect the distinguishability of the two states. More cycles yield a convergence of the histogram to a stable, smooth bimodal distribution. On the other hand, distinguishability of the two populations is affected by the duration at the measurement (M) point. We note that only during the measurement point (M) readout was done by triggering the waveform digitizer card.

The resulting histogram after 10^8 cycles was fit with a sum of two gaussians:

$$A_N e^{-(V_{rf}^{(S2)} - \mu_N)^2/2\sigma_N^2} + A_{N+2} e^{-(V_{rf}^{(S2)} - \mu_{N+2})^2/2\sigma_{N+2}^2}, \tag{6.2}$$

where A, μ, σ are the amplitudes, means, and standard deviations of the N and $N+2$ charge differences. Measured distributions and best fits to Eq. 6.2 for measurement times $\tau = 1\,\mu s$ and $\tau = 5\,\mu s$ are shown in the Fig. 6.6(b). Separation of the two peaks, ΔV, reflects the sensitivity of the charge sensor, while peak widths σ_N and σ_{N+2} result from measurement noise. We define $SNR = \Delta V/\sigma$, where $\sigma^2 = \sigma_N^2 + \sigma_{N+2}^2$. Note that Eq. 6.2 does not include relaxation from N to $N+2$ during the measurement. A more complicated form that includes relaxation during measurement was investigated in Ref. [137]. In the present case, where τ is much shorter than the charge relaxation time, as set by V_M, Eq. 6.2 is valid. The measured SNR as a function of measurement time τ is shown in Fig. 6.6(c) (left axis). SNR > 3 with an integration time of 1 μs was achieved.

Figure 6.6(c) shows that SNR increased with measurement time, τ, as expected. The simplest model of this dependence, assuming uncorrelated noise [118], is $SNR(\tau) = [\Delta V/\sigma(1\,\mu s)][(\tau + \tau_0)/1\,\mu s]^{1/2}$. By using fit parameter $\Delta V = 175.3$ mV, $\tau_0 = 1.5\,\mu s$ and $\sigma(1\,\mu s) = 74.8$ mV, the model yields the curve shown in Fig. 6.6(c), which compares well with the experimentally measured $SNR(\tau)$ in the range 1 - 10 μs.
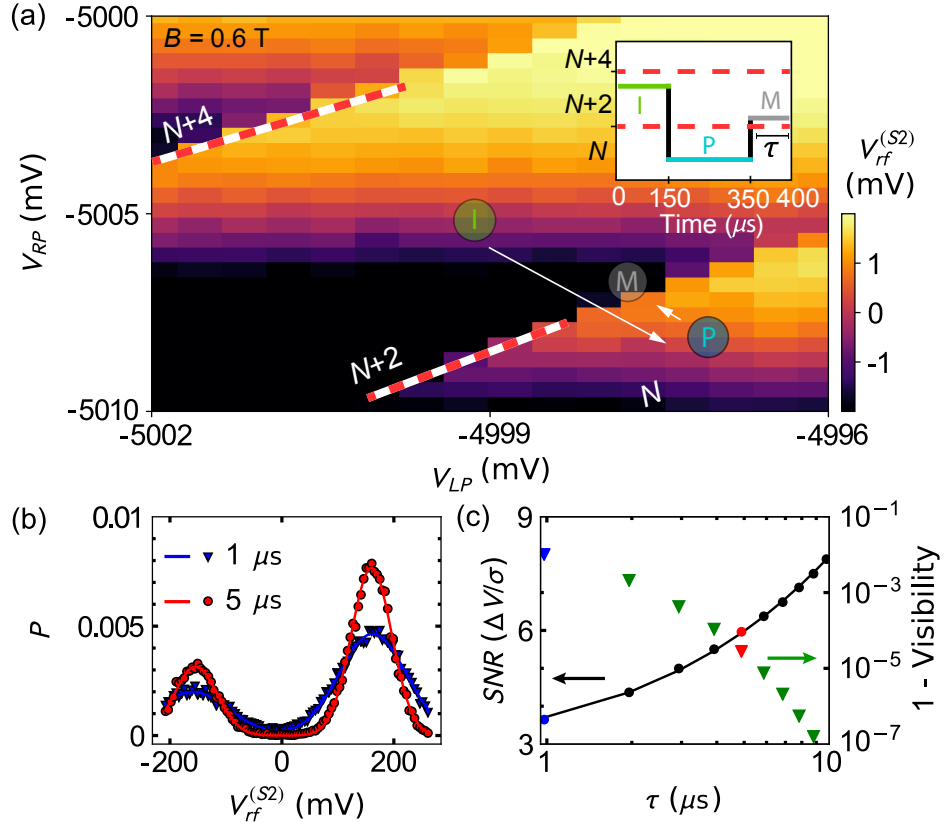
Figure 6.6: Charge sensitivity and signal-to-noise ratio. device C. (a) 1e-1e periodic double-island charge stability diagram at $B = 0.6$ T measured using the right proximal charge sensor. Main device was configured such that tunneling to the left/right lead reservoirs is negligible. Only the inter-island transitions are visible with red and white dashed lines. The relative charge occupancy of the islands is marked as N, $N+2$ and $N+4$. The pulse sequence used to characterize signal-to-noise ratio is shown in the inset (see main text and Supplementary Material B for description), with positions I, M and P indicated on the charge stability diagram that pulsed gates LP and RP move the system to different gate space positions for a given amount of time. (b) Probability of single shot readout outcomes (P) of demodulated voltage signal $V_{rf}^{(S2)}$ for two different measurement times: $\tau = 1$ μs (blue) and $\tau = 5$ μs (red), at the measurement point (M) showing a bimodal relative charge state distribution. c) Signal-to-noise ratio (left axis) at the measurement point (M) together with theory fit. Extracted visibility (right axis) from the double gaussian fits (see main text) as a function of measurement time.

6.5.4 Visibility extraction

Another quantity that characterizes the quality of detection is the visibility, V, defined as the probability of correctly identifying excited and ground states (N and $N + 2$) and is expressed as $V = F_N + F_{N+2} - 1$, where F_N and F_{N+2} are the fidelities calculated following [137]. The resulting dependence of visibility on measurement time, $V(\tau)$, is shown in Fig. 6.6(c), where again effect of relaxation during measurement is neglected. We find $V(1\,\mu s) = 0.998$. These results are comparable to previously reported charge detection studies [138–142].

The extraction of signal-to-noise ratio (SNR) and visibility was accomplished with the following pulse sequence cycle [Fig. 6.6(a) inset]. The pulse sequence starts with a fixed amplitude voltage pulse on gates RP (positive voltage pulse) and LP (negative voltage pulse) bringing the system to a point I for a duration of $\tau_I = 150\,\mu$s for initialization into a relative charge state $N+2$. Then, the gates LP (positive voltage pulse) and RP (negative voltage pulse) bring the system into a relative charge N state (point P) for a time $\tau_P = 200\,\mu$s. Finally, gates LP (negative voltage) and RP (positive voltage) bring the system close to intra-island degeneracy point M (between N and $N+2$ relative charge states) which we denote as measurement position. V_{TX} excitation was controlled with microwave switch (ZASWA-2-50DR+), in order to avoid disturbances in the system during the manipulation phase (I and P). The readout was performed only at the measurement point (M) by triggering the ATS9360, 12 bit waveform digitizer card for a total time duration of $\tau = 50\,\mu$s. To build statistics $N_{\text{cycles}} = 10^8$ experimental runs of the pulse sequence were performed. From histograms of $V_{rf}^{(S2)}$ measurements (with 2 mV bin size), the probability, $P_{V_{rf}^{(S2)}}$ of singe-shot outcomes can be estimated for each value of measurement time τ.

For the sake of simplicity, all denoted V_{rf} here will refer to demodulated voltage with the right charge sensor ($V_{\text{rf}}^{(S2)}$). Visibility is defined as [137]:

$$V = F_N + F_{N+2} - 1 \tag{6.3}$$

where F_N and F_{N+2} are the fidelities of relative charge state N and

$N + 2$, respectively. Fidelity of a charge state N is defined by $F_N = 1 - erf(N)$, where $erf(N)$ is an error of having a pure N charge state. $N + 2$ state fidelity is similarly expressed as $F_{N+2} = 1 - erf(N + 2)$. This error is calculated by cumulative normal distribution function for the two charge states:

$$erf = \begin{cases} \int_{V_T}^{\infty} n_N dV_{rf}, & for\ N \\ \int_{-\infty}^{V_T} n_{(N+2)} dV_{rf}, & for\ N + 2 \end{cases} \qquad (6.4)$$

where V_T is the threshold voltage calculated by two mean Gaussian fit peak position $[(\mu_N + \mu_{N+2})/2]$. The probability density for relative charge state (n_N and n_{N+2}) is expressed:

$$n = \begin{cases} e^{(V_{rf} - \mu_N)^2/2\sigma_N^2}/\sqrt{2\pi}\sigma_N, & for\ N \\ e^{(V_{rf} - \mu_{N+2})^2/2\sigma_{N+2}^2}/\sqrt{2\pi}\sigma_{N+2}, & for\ N + 2 \end{cases} \qquad (6.5)$$

Minimizing the function of two errors $[erf(N)$ and $erf(N + 2)]$ and then inserting found fidelities we calculate the visibility:

$$V = 1 - erf(N) + 1 - erf(N + 2) - 1 \qquad (6.6)$$

This yields a visibility $V = 99.8\%$ for an integration time of $1\ \mu s$.

6.6 Conclusions

In summary, we have investigated RF charge sensing and readout of various InAs/Al nanowire devices relevant for Majorana qubits. Two readout types were studied: First, resonant circuits were directly coupled to the device lead, yielding an improvement in measurement time by a factor of 40 compared to conventional lock-in measurements. Second, charge sensing via a second nanowire capacitively coupled via floating gate to the device allowed charge occupancy in the device to read-out non-invasively and even when visible transport is suppressed through the device.

As an application, we followed the evolution of Coulomb charging from $2e$ periodicity to $1e$ periodicity as an axial magnetic field was increased from 0 to 0.6 T, complementing previous conductance measurement of Majorana signatures, without needing to run current through the device. Sensor quality as a function of measurement time was investigated using a pulse sequence that cycled the charge occupancies of the islands. Signal to noise ratio exceeding 3 can be achieved for integration times of 1 μs with visibility $V = 99.8\%$. Presented results show that rf resonant circuits, both directly coupled to the device, or to proximal capacitive sensors, can be used for fast and detailed characterization that conventional low-frequency techniques are not able to provide.

7

DISPERSIVE SENSING IN HYBRID INAS/AL NANOWIRES

Dispersive charge sensing is realized in hybrid semiconductor-superconductor nanowires in gate-defined single- and double-island device geometries. Signal-to-noise ratios (SNRs) were measured both in the frequency and time domain. Frequency-domain measurements were carried out as a function of frequency and power and yield a charge sensitivity of $1 \cdot 10^{-3}$ e$/\sqrt{\text{Hz}}$ for an ~11 MHz measurement bandwidth. Time-domain measurements yield $SNR > 1$ for 20 μs integration time. At zero magnetic field, photon-assisted tunneling was detected dispersively in a double-island geometry, indicating coherent hybridization of the two superconducting islands. At an axial magnetic field of 0.6 T, subgap states are detected dispersively, demonstrating the suitability of the method to sensing in the topological regime.

7.1 Introduction

Readout of quantum systems on timescales short compared to coherence or relaxation times is typically performed by one of a few schemes: (i) the device is incorporated into a resonant circuit, allowing state-dependent changes in the damping or shift of the resonance to be measured, [118, 144–146] (ii) the quantum state is converted to charge, which is then detected by a nearby electrometer, [124, 125, 147, 148] or (iii) a state-dependent capacitive coupling to the system results in a frequency shift in the coupled resonant circuit that depends on the quantum state, [149, 150] the latter referred to as dispersive readout. In the context of topological qubits, several proposals for non-locally encoding fermion parity in Majorana zero modes have been made [53, 56, 151–153]. Some proposals use parity-to-charge conversion for readout [56], while others use state-dependent hybridization of the Majorana mode with an ancillary system, leading to a dispersive readout signal [53, 152].

Integrating readout circuitry into an existing electrostatic gate or ohmic contact is useful for reducing device footprint and lead count [150, 154–165, 165]. In this case, dispersive readout is performed by monitoring state-dependent shifts in the resonance frequency $f_R = (LC_{tot})^{-1/2}$ of an LC circuit connected to a gate, where f_R is detuned from the qubit transition frequency. The total capacitance, C_{tot}, comprises geometric capacitance, C_g (including parasitic contributions), quantum capacitance, C_Q, and tunnel capacitance, C_T [149, 166]. When the quantum system consists of a Coulomb island tunnel coupled to a reservoir, C_Q arises from continuous charge transitions, and is proportional to the curvature of energy with respect to the confining gate voltage [54]. The maximum magnitude of C_Q occurs at gate voltages corresponding to charge degeneracy, with opposite signs for ground and first excited states. C_T is significant when the energy relaxation rate exceeds f_R. The dependence of f_R on C_Q provides the quantum state selectivity of the dispersive shift. Monitoring phase or magnitude of the signal reflected from the resonant circuit thus allows readout of the quantum state of the system.

Recent work on gate-based dispersive sensing has addressed semiconducting nanowires (NWs) [167, 168] and semiconductor quantum

dots coupled to subgap states in semiconductor-superconductor NWs at zero magnetic field [169]. Beyond qubit readout, dispersive sensing has been used to allow rapid tuning of quantum devices, yielding complementary information to conventional transport approaches [170].

In this chapter, we explore dispersive charge sensing in an epitaxial semiconductor-superconductor (InAs/Al) nanowire device configured to form either a single or double island depending on gate voltages. Since both proximity-induced superconductivity and high magnetic fields are needed for realizing the topological regime, we have focussed particular attention on operation at magnetic fields compatible with topological superconductivity. At zero field, we extract a signal-to-noise ratio (SNR) of a gate-based dispersive sensor as a measure of its sensitivity. Time-domain measurements gave SNR > 1 for integration times $> 20\ \mu$s, as described in detail below. Applying a continuous
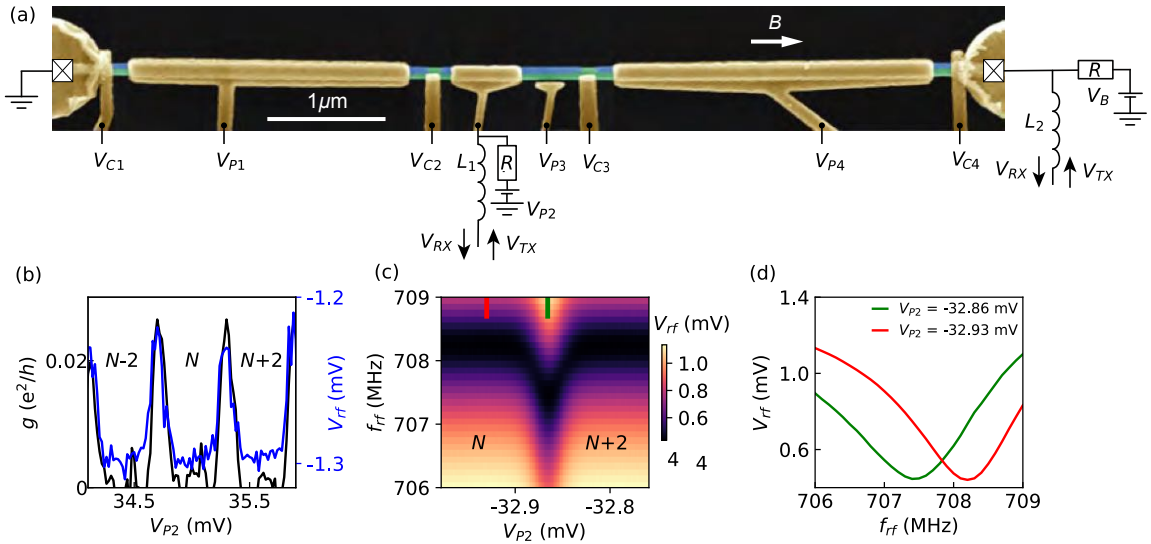
Figure 7.1: Half-shell Al nanowire device with dispersive readout signal. (a) Scanning electron micrograph of the nanowire device together with the relevant electrostatic gates labeled. (b) Coulomb blockade oscillations of superconducting single-island defined between gates C2 and C3 as a function of plunger gate voltage V_{P2} recorded in conductance g via lock-in transport (black) and dispersive lead sensing V_{rf} (blue) showing close matching. (c) Lead sensor signal V_{rf} as a function of electrostatic plunger gate voltage V_{P2} tuning the superconducting island over the Coulomb degeneracy as a function of readout frequency f_{rf}. (d) Line cuts from (c) on- (green) and off- (red) Coulomb degeneracy. Dispersive shift in frequency can be observed as the island is tuned over the degeneracy.

microwave drive to a nearby gate induces photon assisted tunneling (PAT) [171, 172], indicating coherent hybridization of the two islands.

7.2 Experimental setup and initial checks

The device, shown in Fig. 7.1(a), is based on an InAs/Al NW with 7 nm of epitaxial Al grown on three facets of the hexagonal cross section [46]. Following deposition of individual wires on a Si/SiO$_2$ substrate, three 100 nm segments of Al were removed by wet etching to provide tunable tunnel barriers. An insulating layer of HfO$_2$ was then deposited over the wire and electrostatic gates labeled C1, C2, C3 and C4 were deposited, creating three segments of lengths $\sim 2.5\,\mu$m, $1\,\mu$m, and $3.5\,\mu$m, separated by gate-voltage-controlled barriers of InAs only (see Supplementary material for fabrication details). The detector gate, labeled P2, and the right ohmic contact were bonded to superconducting spiral inductors [161] fabricated on a separate sapphire chip to form a resonant circuit that was capacitively coupled to a conventional radio-frequency (rf) reflectometry detection chain. Each resonator was also connected to bias resistors, allowing DC voltages to be applied to the gates. Data from two devices (D1 and D2) are presented. All measurements were made in a dilution refrigerator with base temperature ~ 20 mK equipped with a vector magnet (see Appendix E for measurement details).

We initially consider zero magnetic field. Electrostatic gates C2 and C3 were set to the tunneling regime, forming a superconducting single island. A comparison of conductance measured via low-frequency transport using a lock-in amplifier versus reflectometry from the right ohmic contact is shown in Fig. 7.1(b). The conductance, g, around zero bias showed Coulomb blockade (CB) peaks as a function of plunger voltage V_{P2}. Finite bias conductance measurements yielded a charge energy of $E_C = 60\ \mu$eV. CB oscillations had a period of two electron (2e) charge. This is expected for $\Delta > E_C$, where $\Delta \sim 180\ \mu$eV is the induced superconducting gap, and indicates low average quasiparticle poisoning. Figure 7.1(c) shows the ohmic reflectometer response as a function of plunger voltage V_{P2} and rf readout frequency f_{rf}, see Supplementary material for details. The resonance shows a state-dependent shift when crossing the island degeneracy [Fig. 7.1(d)]. As shown later, PAT

was observed at a frequencies ≥ 11 GHz, i.e., highly detuned from the readout resonators, indicating a state-dependent dispersive interaction between the resonator and the device.

In a lithographically similar device (D2), the gate sensor sensitivity at zero magnetic field was evaluated in a superconducting single-island regime, the island had charging energy $E_C = 105$ μeV. A nearby gate [P3 in Fig. 7.1(a)] was modulated with a sinusoidal signal of fixed frequency (f_M) and amplitude V_M [124, 150, 160]. Positioning the island gate V_{P2} on the side of a CB peak amplitude modulates the island charge, and thereby the readout resonance, inducing sidebands that are symmetrically detuned by f_M from the carrier frequency, f_{rf}.

7.3 Signal-to-noise characterization

Figure 7.2(a) shows the signal reflected from the detector gate P2 recorded with a spectrum analyser with Δf = 13.4 Hz resolution bandwidth. Around the resonance frequency (~ 438 MHz) two sidebands are observed at $f_M = \pm 12$ kHz. For the analysis that follows the upper sideband was chosen. Signal-to-noise ratio (SNR) is given by the ratio of the height of the sideband to the noise floor in a given bandwidth. The SNR dependence on the rf carrier power P_{rf} (before $\sim$40 dB attenuation) is shown in Fig. 7.2(b). An initial increase in SNR up to around $P_{rf} = -35$ dBm is observed followed by a decrease for larger power. This turnaround behavior can be explained by the trade off between lifetime and power-induced broadening [157]. Figure 7.2(c) shows the SNR dependence on the f_{rf} for a fixed $P_{rf} = -35$ dBm. A maximum SNR was observed at $f_{rf} \sim 435$ MHz. The full-width half-maximum of the SNR as a function of f_{rf} indicates an approximate resonator bandwidth of ~ 12.2 MHz.

With P_{rf} and f_{rf} set to maximize SNR [see Figs. 7.2(b, c)], a detection bandwidth of ~ 11 MHz was determined [150] by measuring the modulation frequency f_M at which SNR decreased by 3 dB, as shown in Fig. 7.2(d). We next evaluate the charge sensitivity $S \equiv \Delta q (2\Delta f)^{-1/2} 10^{-\text{SNR}/20}$, measured in the time domain, [173] taking spectral resolution $\Delta f = 13.4$ Hz and SNR ~ 15 as a typical value for optimal detection parameters [see Figs. 7.2(b,c)]. The effective charge change induced by modulation at amplitude $V_M = 30$ mV$_{pp}$ was
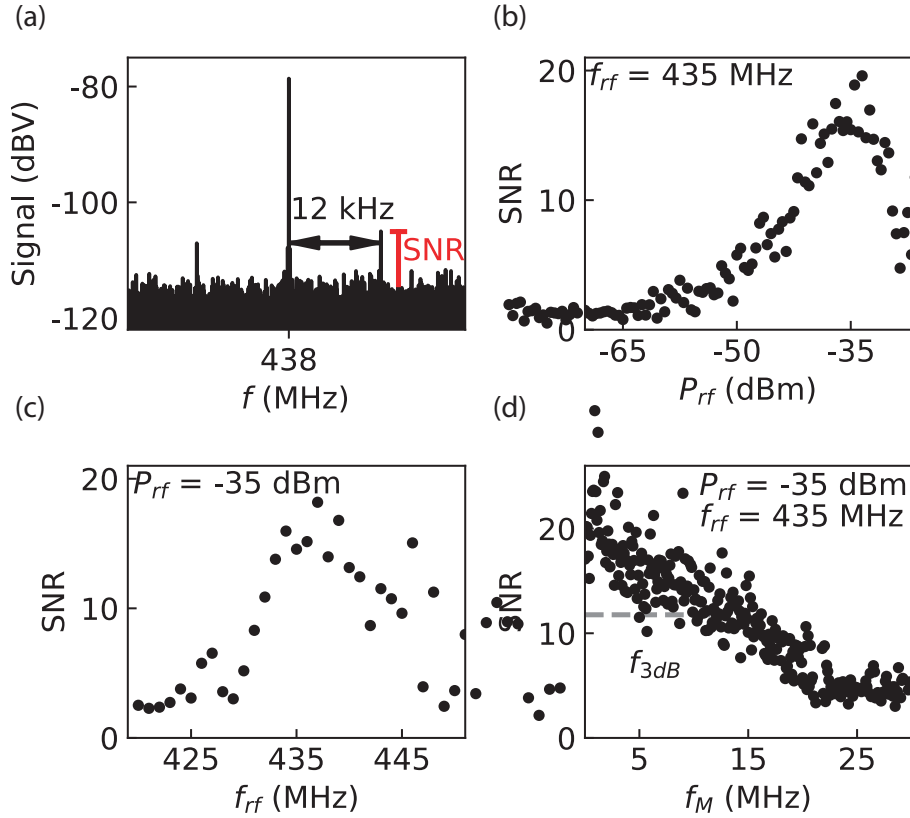
Figure 7.2: Signal-to-noise ratio extraction for different carrier frequencies and powers. (a) Spectrum reflected from the detector gate P2 under gate-modulation as described in the main text, two sidebands symmetrically detuned from resonance were observed. (b) Signal-to-noise ratio dependence on carrier power P_{rf} and (c) on carrier frequency f_{rf}. (d) Signal-to-noise ratio as a function of modulation frequency f_M. The 3 dB frequency, $\sim 11\,\text{MHz}$, indicates the bandwidth of the measurement.

$\Delta q = e(30\,\text{mV}_{pp}/950\,\text{mV}_{pp}) \sim 0.03e$, found by comparing the amplitude of V_M (30 mV$_{pp}$) to the amplitude needed to sweep over a full CB peak spacing (950 mV$_{pp}$). The factor $1/\sqrt{2}$ accounts for the power collected from both sidebands. The resulting charge sensitivity was $S \sim 1 \cdot 10^{-3} e/\sqrt{\text{Hz}}$.

The time needed to obtain a particular SNR at optimal values $f_{rf} = 438\,\text{MHz}$ and $P_{rf} = -40\,\text{dBm}$ was determined by comparing the difference, δV, in signal V_{rf} on and off a CB peak with the noise of the measurement, which decreased with increasing signal averaging. In the single-island regime, gate P2 was pulsed on and off a CB peak with amplitude equivalent to $\sim 0.3e$ at a repetition frequency of 2 kHz. In-phase
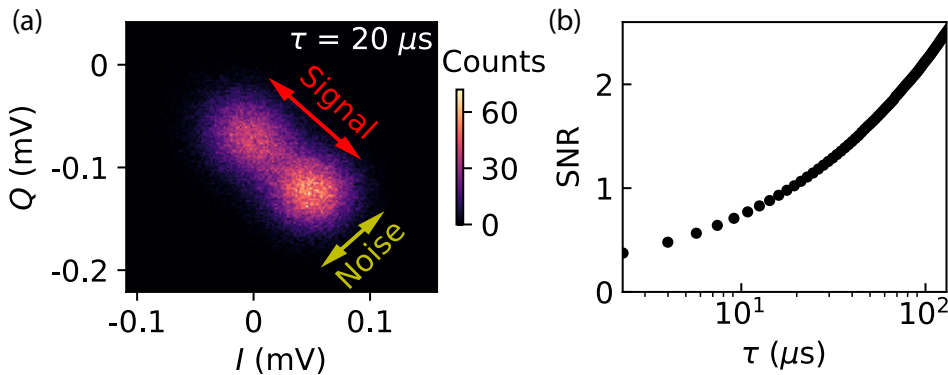
Figure 7.3: SNR for increasing integration times. (a) Two distinguishable states indicated in in-phase (I) and quadrature (Q) plane together with "Signal" δV defined as a separation between two IQ space maxima and "Noise" 2σ as induced broadening of the two maxima. (b) Signal-to-noise ratio ($\delta V/2\sigma$) as a function of integration time τ.

(I) and quadrature (Q) components were recorded with time constant 500 ns, averaged over an integration time τ, and plotted in the complex I - Q plane. Figure 7.3(a) shows an example with $\sim 1.1 \times 10^4$ points averaged for $\tau = 20\,\mu$s each. SNR(τ) was found by fitting to two 2D Gaussians, yielding signal δV and noise, 2σ. The time-domain SNR, given by $\delta V/2\sigma(\tau)$ is shown in Fig. 7.3(b). SNR ~ 1 is reached for integration time $\tau \sim 20\,\mu$s.

7.4 Dispersive sensing in Coulomb blockade

Figure 7.4(a) shows V_{rf} measured using a dispersive sensor on gate P2 [see Fig. 7.1(a)] rather than an ohmic contact. Coulomb diamonds were observed with the device configured as single island at $B = 0$. Each measured point in Fig. 7.4 was averaged 100 times, yielding a measurement time of 60 μs per point. At high bias, $V_B > 0.2$ mV, the period of Coulomb oscillations was halved compared to low bias, indicating that low-bias transport was predominantly carried by Cooper pairs. Figure 7.4(b) shows the phase response of the demodulated signal. The readout frequency was chosen to optimize the $1e$ charge transitions leading to a non-monotonic response for $2e$ charge transitions that had a larger capacitive shift of the resonator. The estimated gate sensor geometric capacitance $C_{\text{g}} = e/\delta V_{\text{g}} \sim 0.55$ F, where δV_{g} is a gate space periodicity of the island plunger P2. This makes $C_{\text{g}} \sim 0.4 C_{\Sigma}$ using the
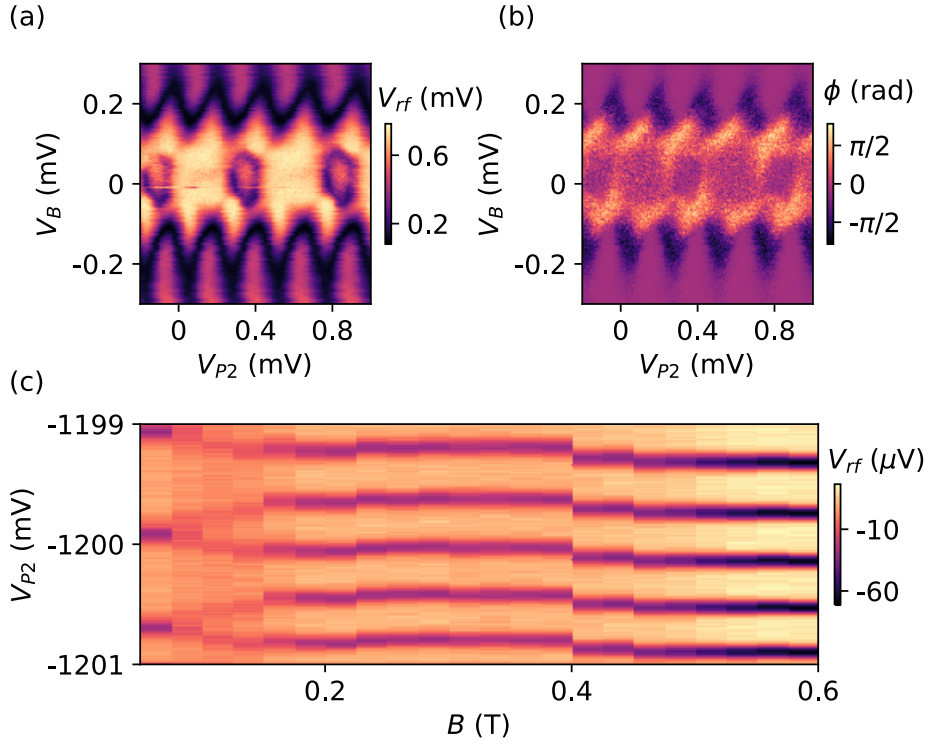
Figure 7.4: Gate-based sensing in Coulomb blockade and in field. (a) Gate P2 sensing of Coulomb blockaded superconducting single-island recorded in magnitude V_{rf} (a) and phase ϕ (b) of the demodulated signal as a function of island plunger voltage V_{P2} and bias V_B. (c) Coulomb blockade evolution from $2e$ to $1e$ periodic regime as a function of parallel to the nanowire axis magnetic field B and island plunger voltage V_{P2} (line average along V_{P2} axis subtracted).

normal-state charging energy of the island.

Application of a parallel magnetic field, B, induced subgap states in the nanowire and an evolution from $2e$ to $1e$ periodic CB oscillations, as shown in Fig. 7.4(c), where an average V_{rf} was subtracted at each field. $1e$ periodic CB oscillations correspond to a state at zero-energy in the superconducting gap, [57] though not necessarily a discrete state. To keep maximum detection contrast at each magnetic field value the readout frequency was adjusted to compensate for changing kinetic inductance of the resonator. The jump at $B \sim 0.4$ T was likely due to electrostatic background charges in the NW environment. The detected signal did not degrade at magnetic field ranges compatible with tuning into a topological state in similar wires [58].

The gate voltage V_{P2} for Fig. 7.4(c) was selected based on the appear-

ance of a discrete state in the spectrum at high magnetic field whereas the Fig. 7.4(a) is at zero magnetic field where sub-gap states are not present. Previous studies [58] have shown that in hybrid InAs/Al nanowires the potential should be tuned to induce a discrete state in the sub-gap spectrum of the nanowire.

The lifetime of the excited state was too short to measure directly, but could be estimated using PAT in a double-dot configuration. At zero field, the $2e$-periodic double-dot charge stability diagram as a function of voltages V_{P2} and V_{P4} takes on a familiar honeycomb pattern [121, 174, 175] as seen in Fig. 7.5(a). The gate sensor detected two types of transitions: internal, between the two islands, and external, to the left superconducting lead. Transitions to the right normal lead could also be discerned, though with less visibility. Spectroscopy was performed by irradiating the sample with microwaves of frequency f_d. When f_d was comparable to or larger than the tunneling rate of Cooper pairs across the junction, $hf_d > E_J$, where E_J is the Josephson energy, characteristic PAT features were observed in the charge stability diagram [174] as seen in Fig. 7.5(b). As usual [172, 175, 176], PAT signatures appear as parallel features along the detuning axis. To quantify the interdot coupling, f_d was swept with the system tuned using P4 to cross the interdot charge transitions when gate P2 was also swept. The resulting 2D plot, shown in Fig. 7.5(c) reveals the emergence of PAT features above 11.3 GHz, placing a rough lower bound on E_J. This extends our previous work on PAT in hybrid double-dot systems [172] to the technique of dispersive readout.

Finally, we note that the detection sensitivity presented here is comparable to previous reports of gate-based sensing. For example, using similar inductors, Colless *et. al* report charge sensitivity $6.3 \cdot 10^{-3}$ e/$\sqrt{\text{Hz}}$ with 10 MHz detection bandwidth, compatible with our result [150]. However, we do not reach the highest sensitivities realized using gate-based sensing in nanowire transistors [157, 162] ($37 \cdot 10^{-6}$ e/$\sqrt{\text{Hz}}$ and $1.3 \cdot 10^{-6}$ e/$\sqrt{\text{Hz}}$ respectively), rf-quantum point contacts [145] ($2 \cdot 10^{-4}$ e/$\sqrt{\text{Hz}}$) or rf-SETs [141, 144] with typical sensitivities $1 \cdot 10^{-5}$ e/$\sqrt{\text{Hz}}$. Latest results from silicon spin qubits using gate sensing [156] reach sensitivity $4.1 \cdot 10^{-4}$ e/$\sqrt{\text{Hz}}$ with an estimated SNR = 6 for 1 μs integration time. In our case, sensitivity could be fur-
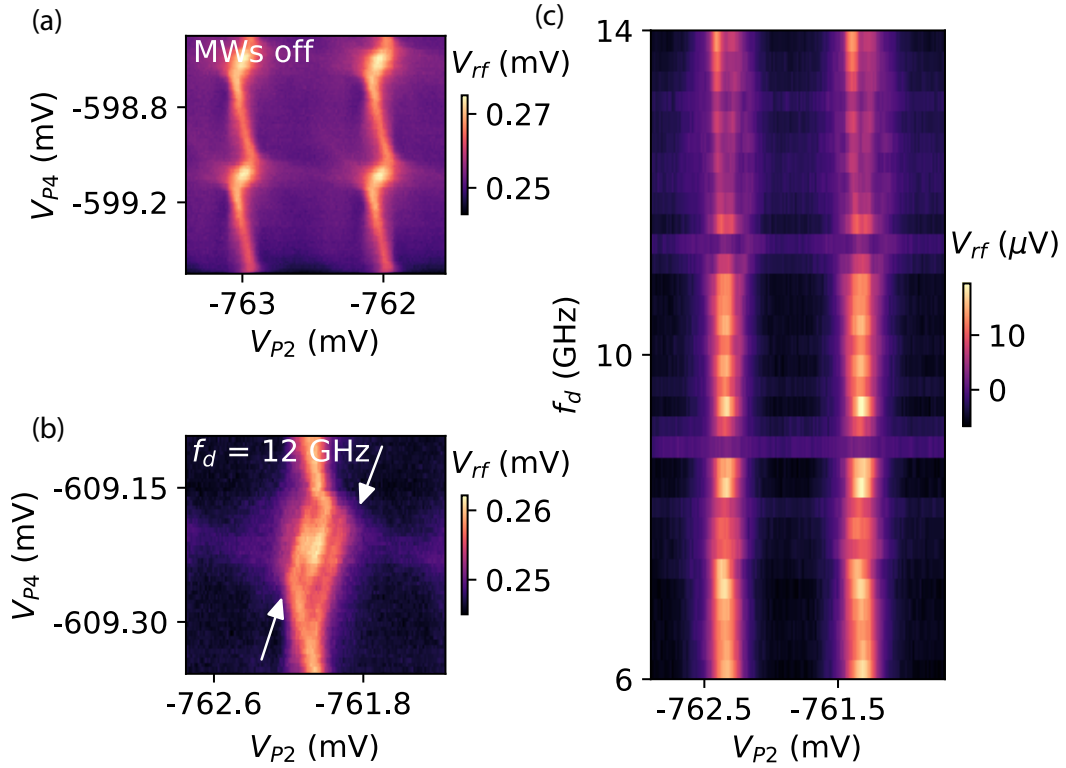
Figure 7.5: Photon-assisted tunneling in double quantum dot. (a) $2e$ periodic charge stability diagram as a function of right (V_{P4}) and middle plunger (V_{P2}) voltages. (b) Microwave induced photon assisted tunneling transitions between two charge states in a double-island at zero magnetic field. (c) Energy dispersion of the double-island energy levels measured as a function of the plunger voltage V_{P2} and microwave drive frequency f_d.

ther improved by for example decreasing the parasitic capacitance. The results will be useful in employing gate and lead-based dispersive sensing in topological qubit experiments without the requirement of fabricating nearby electrometers.

7.5 Conclusions

In summary, gate and lead-based dispersive sensing techniques were applied to Coulomb blockaded single- and double-islands in hybrid semiconductor-superconductor InAs/Al nanowires. Characterization of gate sensing, using sideband modulation, at zero magnetic field, as a function of readout parameters, yielded charge sensitivities of the order of $1 \cdot 10^{-3}$ e$/\sqrt{\text{Hz}}$, with a detection bandwidth of ~ 11 MHz. In time-domain measurements, SNR of 1 was achieved for an integration time of 20 μs. Dispersive readout of photon assisted tunneling indicated coherent hybridization of two superconducting islands gave an estimate for the Josephson coupling between islands, $E_J \sim 11.3$ GHz. Magnetic field compatibility of the gate sensor up to 0.6 T was demonstrated, compatible with tuning into the topological regime.

A

FABRICATION RECIPES

This Appendix presents all the fabrication recipes that were used for the creation of quantum devices in this thesis. First, presenting the full-shell Al nanowire interferometer device fabrication from Ch. 4 and Ch. 5. Secondly, half-shell charge sensing device fabrication from Ch. 3, 6 and 7 are introduced.

Spin	Adhesion promoter (AR300 80 new) 4000 rpm for 1 min
Post-bake	Bake chip on 185°C hot plate for 2 min
Acetone rinse	Place the chip in Room T beaker acetone for 5 min
Spin	Double EL6 4000 rpm for 1 min
Post-bake	Bake chip on 115°C hot plate for 1 min

Table A.1: Full-shell interferometer fabrication. Resist preparation for wet etching regions on the nanowire.

E-beam	Dose coefficient 0.24, WF - 300 μm, dot size - 60k
Development	Rinse MIBK(1:3) for 1 min
IPA rinse	Rinse in IPA for 20 s
N dry	Blowdry with nitrogen gun

Table A.2: **Full-shell interferometer fabrication**. Electron-beam lithography for etching regions and development.

Ashing	Oxygen plasma cleaning for 1 min
Post-bake	Bake chip on 125°C hot plate for 30 s
MF321 Developer	Room T etchant with magnetic stir, etching for 1 min
MQ rinse	Rinse in MQ for 10 s
Fresh MQ rinse	Fresh rinse in MQ for 40 s
N dry	Blowdry with nitrogen gun
Resist strip	Place the chip in Room T beaker acetone for 5 min

Table A.3: **Full-shell interferometer fabrication**. Selective Al etching on the nanowires.

To insure that the interferometers superconducting loop withstands moderate magnetic fields $<$ 200 mT, it is important to have thin Al loop with leads. That is why the polymer resistant ramp structure was developed to ensure a continuous thin (25 nm) *ex-situ* deposited Al loop. Steps were taken to make smooth polymer resist ramps in Table. A.4.

To inspect if resist ramps have a continues profile next to nanowire, atomic force microscope was used on test sample nanowires in Fig. A.1 (a)-(b). From AFM profile cuts it can be seen that ramps made close to the nanowire have relatively smooth profile, which means thin Al can be deposited next to the nanowire uninterpreted. However, from AFM images, one can see relatively high side walls, these were originated as a consequence from Kauffman milling procedure that is in later fabrication steps. Side walls are most likely a mixture of SiO_2 and polymer
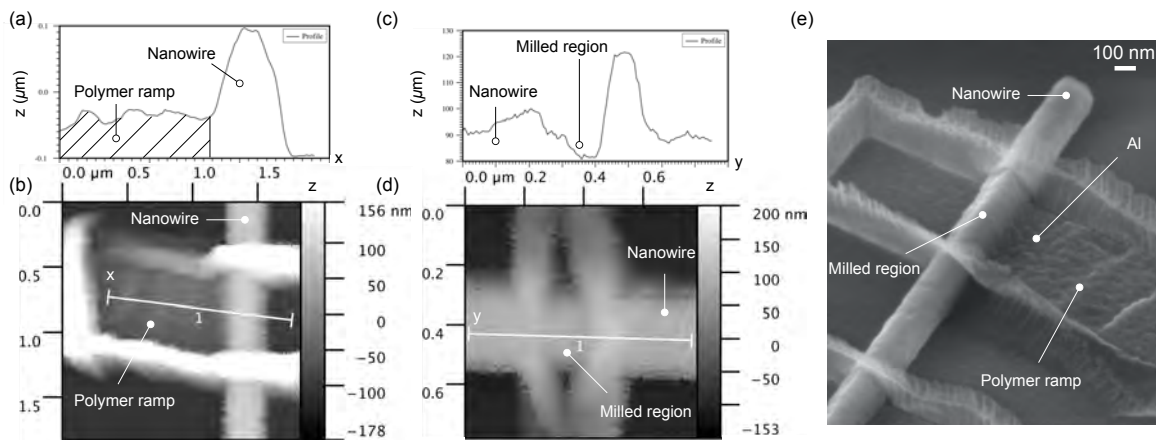
Figure A.1: Polymer resist ramps on test full-shell nanowires with AFM profile cuts.
(a) AFM profile along x cut in (b) transverse to the full-shell nanaowire, showing a un-interrupted polymer profile. (c) AFM profile cut along the nanowire, highlights the Kauffman milled region necessary removal of an oxide layer from the full-shell Al nanowire to have low resistance Ohmic contact. (e) Scanning-electron micrograph of test full-shell nanowire with polymer ramp close to nanowire and deposited a contin-ues thin (25 nm) of Al.

resist, which seems not to affect the overall performance of the interfer-ometers to current knowledge.

Spin	PMMA resist (A6) 4000 rpm for 1 min
Post-bake	Bake chip on 115°C hot plate for 1 min
Design	Exposing rectangle frame with dimensions 1 μm^2 and 0.5 μm width
E-beam	Dose coefficient 0.4, WF - 300 μm, dot size - 60k
Development	Rinse MIBK(1:3) for 1 min
IPA rinse	Rinse in IPA for 20 s
N dry	Blowdry with nitrogen gun
Ashing	Oxygen plasma cleaning for 1 min
Post-bake	Bake chip on 185°C hot plate for 1 min
Design	Rectangle 2 μm^2 covering the previous exposed shape
Cross-link w/ E-beam	Dose coefficient 12, WF - 300 μm, dot size - 60k
Acetone strip	Rinse in acetone for 2 min

Table A.4: Full-shell interferometer fabrication. Resist polymer smooth ramps for thin Al loop with leads.

Spin	PMMA resist (A6) 4000 rpm for 1 min
Post-bake	Bake chip on 115°C hot plate for 1 min
Design	Exposing loop 8 μm^2 and 0.2 μm width, that are connected to bond pad meanders to control as leads
E-beam	Dose coefficient 0.4, WF - 300 μm, dot size - 60k
Development	Rinse MIBK(1:3) for 1 min
IPA rinse	Rinse in IPA for 20 s
N dry	Blowdry with nitrogen gun
Ashing	Oxygen plasma cleaning for 1 min
AJA milling	Kaufman milling, 4.5min 1mTorr flow
AJA deposition	25 nm of Al deposition with 0.3 Å/s rate
Lift-off	Removing resist with NMP beaker heted 55°C for 1 h
IPA rinse	Rinse in IPA for 20 s
N dry	Blowdry with nitrogen gun

Table A.5: Full-shell interferometer fabrication. Al loop with leads deposition and milling.

Spin	Resist (EL4) 4000 rpm for 1 min
Post-bake	Bake chip on 115°C hot plate for 1 min
Spin	Double PMMA resist (A2) 4000 rpm for 1 min
Post-bake	Bake chip on 115°C hot plate for 1 min
Design	Exposing rectangle with dimensions covering the device 20 μm^2
E-beam	Dose coefficient 0.53, WF - 300 μm, dot size - 60k
Development	Rinse MIBK(1:3) for 1 min
IPA rinse	Rinse in IPA for 20 s
N dry	Blowdry with nitrogen gun
Ashing	Oxygen plasma cleaning for 1 min
ALD system	Degas on 95°C for 8h with 68 cycles $\approx$ gives 7 nm of oxide thickness
Lift-off	Scratch on the edges of the chip followed by resist removal with NMP beaker heted 65°C for 2 h
IPA rinse	Rinse in IPA for 20 s
N dry	Blowdry with nitrogen gun

Table A.6: Full-shell interferometer and half-shell device fabrication. Atomic layer deposition, preparation for top-gates.

Spin	PMMA resist (A6) 4000 rpm for 1 min
Post-bake	Bake chip on 115°C hot plate for 1 min
Design	Exposing gates 0.2 μm^2 and 0.2 μm width, that are connected to bond pad meanders to control as gates
E-beam	Dose coefficient 0.4, WF - 300 μm, dot size - 60k
Development	Rinse MIBK(1:3) for 1 min
IPA rinse	Rinse in IPA for 20 s
N dry	Blowdry with nitrogen gun
Ashing	Oxygen plasma cleaning for 1 min
AJA deposition	5 nm of Ti deposition with 0.6 Å/s rate
AJA deposition	200 nm of Au deposition with 1.5 Å/s rate
Lift-off	Removing resist with NMP beaker heted 55°C for 1 h
IPA rinse	Rinse in IPA for 20 s
N dry	Blowdry with nitrogen gun

Table A.7: Full-shell interferometer and half-shell device fabrication. Ti/Au top-gate deposition.

Spin	PMMA resist (A4) 4000 rpm for 1 min
Post-bake	Bake chip on 115^oC hot plate for 1 min
E-beam	Exposing etching regions, dose coefficient 0.4, WF - 300 μm, dot size - 60k
Development	Rinse MIBK(1:3) for 1 min
IPA rinse	Rinse in IPA for 20 s
N dry	Blowdry with nitrogen gun
Ashing	Oxygen plasma cleaning for 1 min
Transene D	Etchant placed in beaker heated to 55^oC chip immersed for 5 s followed by MQ rinse

Table A.8: Half-shell Al nanowire device fabrication. Selective Al etching on the nanowires.

B

QUANTUM-DOT PARITY EFFECTS

B.1 Other devices

We present measurements of two other devices, denoted devices 2 and 3. The device in the main text is device 1. Micrographs of devices 2 and 3 are shown in Fig. B.1(a,b). The micrograph of device 2 was taken before final gate deposition so that the bare etched junctions are visible. The active elements used in this experiment were the same for all devices. In contrast to device 1, however, devices 2 and 3 do not have additional junctions (uncolored gates in Fig. 1 of the main text) that were open during measurements. All devices were fabricated using the procedure described in the main text, using nanowires from the same growth batch with $\sim$ 130 nm InAs diameter core and a 30 nm Al-shell.

The axial magnetic field, $B_\parallel$ was used to control flux winding in the Al-shell. Perpendicular magnetic field, $B_\perp$ was used for phase measurements. V_{dot} was used to control the occupancy of a quantum dot formed close to depletion in the dot-junction. We first describe the results of voltage-bias measurements, and then current-bias measurements in these devices.
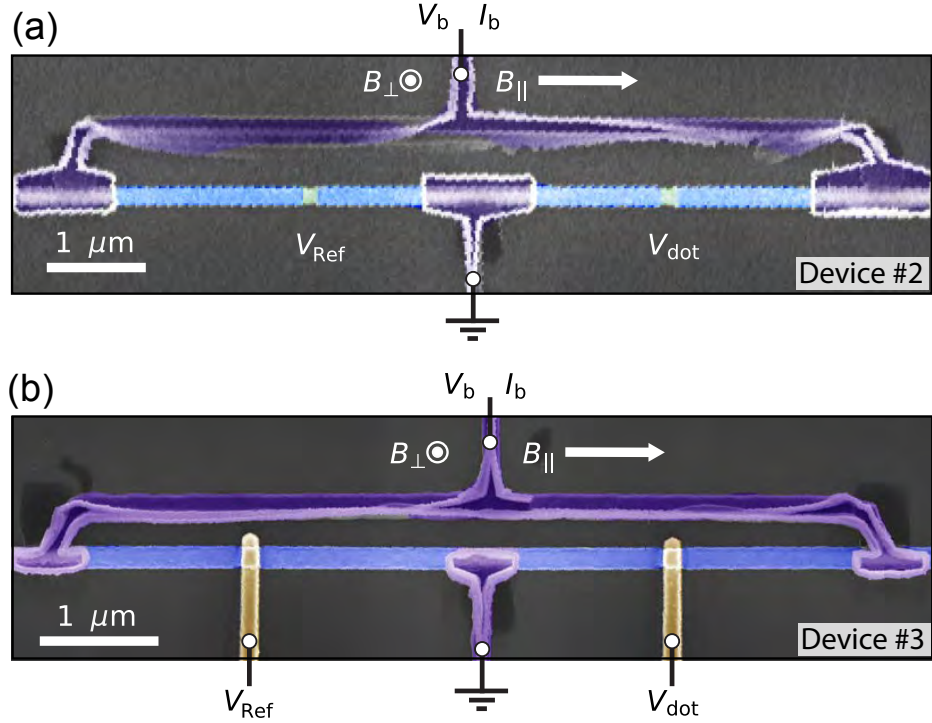
Figure B.1: False-color scanning electron micrographs of other measured devices. (a) Device 2 with two controllable junctions V_{Ref} and V_{dot}. Micrograph was taken before gate deposition, allowing regions of etched Al shell to be seen. (b) Device 3 micrograph, taken after fabrication of the gates, controlled by V_{Ref} and V_{dot}. For both devices axial $B_{\parallel}$ and out-of-plane $B_{\parallel}$ magnetic fields are independently controlled.

B.2 Voltage-bias measurements

Voltage-bias spectroscopy for both devices 2 and 3 on the dot-junction was performed by closing the reference arm of the interferometer by setting $V_{\text{Ref}} = -2\,\text{V}$.

Figure B.2 shows voltage-bias measurements of the differential conductance for device 2. First, in the zeroth lobe ($B_{\parallel} = 0$), Fig. B.2(a) shows differential conductance, dI/dV_{b}, as a function of the DC bias, V_{b}, and V_{dot}. Two enhancements of the zero-bias conductance were observed at the charge transition points of a quantum dot formed in the junction. Figure B.2(b) shows conductance in the same range of V_{dot} in the first lobe at $B_{\parallel} = 110\,\text{mT}$; a significant enhancement of the zero-bias conductance peak was observed in the Coulomb valley, we assigned this valley as the dot o-state based current-bias measurements presented below. Figure B.2(c) shows conductance as a function of $B_{\parallel}$
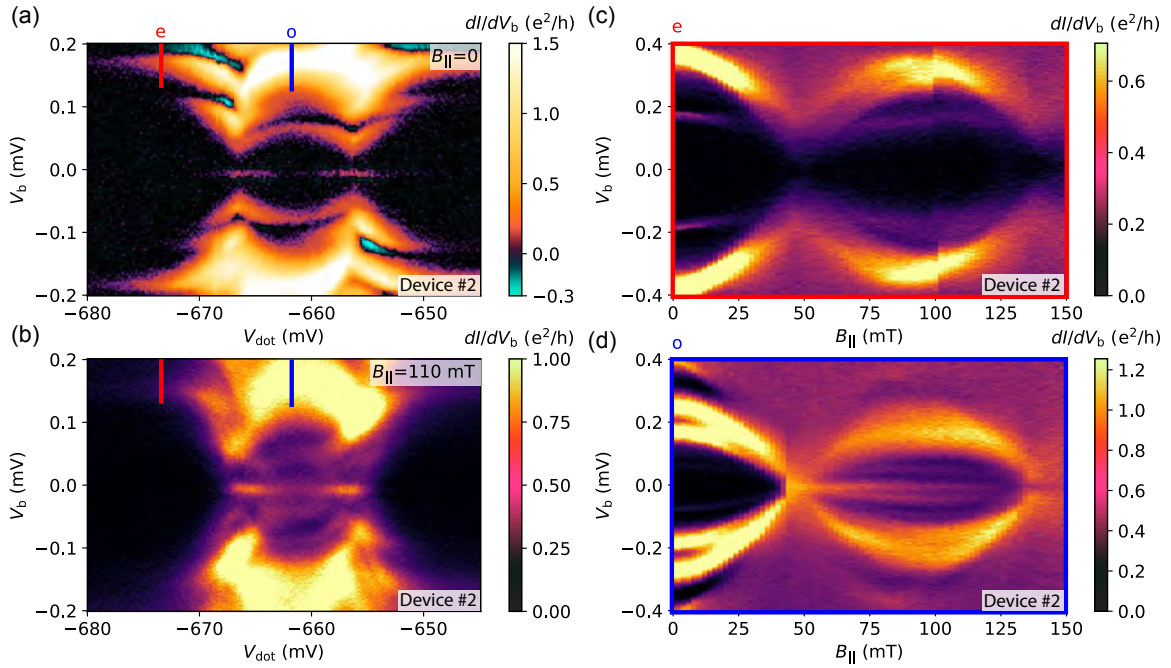
Figure B.2: Voltage-bias measurement of isolated dot-junction of device 2 with reference arm closed. (a) Differential conductance dI/dV_b as a function of voltage-bias, V_b, and V_{dot} at $B_\| = 0$. Even (e) and odd (o) dot occupancies are indicated with red and blue markers. (b) The same voltage range of V_{dot} gate indicating the same quantum-dot with two charge occupancies (e, o) at $B_\| = 110$mT. (c) Differential resistance measurement of axial magnetic field, $B_\|$, evolution as a function of voltage-bias in the even dot occupancy (d) Similar measurement as panel (c) for the o-state Coulomb valley.

in the e-state, demonstrating the closing of the superconducting gap by the Little-Parks effect. In contrast to the e-state, the o-state (Fig. B.2(d)) showed a strong enhancement of the zero-bias conductance in the first lobe, in a similar manner to device 1 in the main text.

Figure B.3 shows voltage-bias measurements for device 3. Charge transitions are observed at $V_{dot} \sim 184$ mV in both the zeroth (Fig. B.3(a)) and the first lobe (Fig. B.3(b)). In device 3 the gate voltage separation between the charge transitions was significantly smaller; therefore, while the conductance is higher in the first lobe it was not possible to unambiguously compare the behaviors in the e-state and the o-state valleys.

B.3 Current-bias measurements

Current-bias spectroscopy measurements of the differential resistance, dV/dI_b, for all devices was performed with the reference arm in a multi-
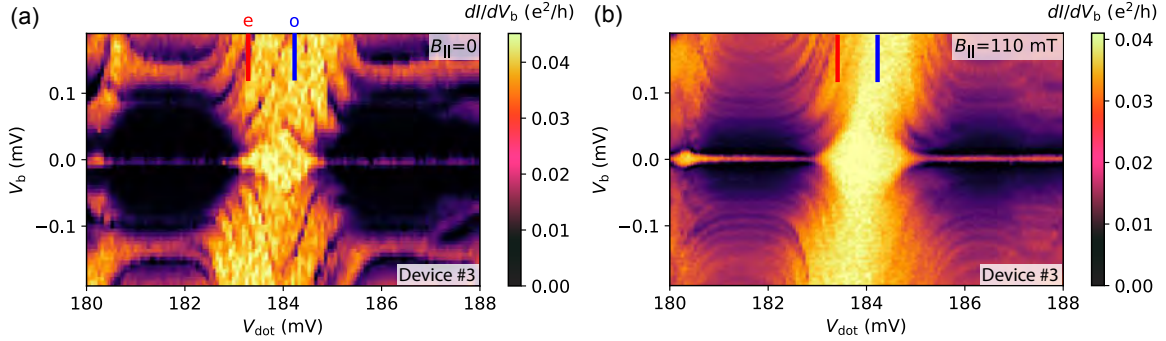
Figure B.3: Voltage-bias measurement of isolated dot-junction in Device 3 with reference arm closed. (a) Differential conductance dI/dV_b as a function of voltage-bias V_b and $vdot$, red and blue markers indicate even and odd dot occupancies, respectively. (b) Similar as panel (a) in the first lobe at $B_{\parallel} = 110$mT.

channel transmitting regime, controlled using V_{Ref}, so that $B_{\perp}$ primarily changes the phase across the dot-junction.

Figures B.4(a,b) show current-bias measurements of the differential resistance, dV/dI_b, for device 2 in the zeroth lobe as a function of V_{dot} and $B_{\perp}$, at the V_{dot} positions indicated for the e and o-states, respectively, in Fig. B.2(a). Similarly, Figs. B.4(c,d) show dV/dI_b in the first lobe at the same gate voltages, in the e and o-states. We review our conclusions based on these data below.

Figure B.5(a) shows current-bias measurements of dV/dI_b for device 3 in the zeroth lobe as a function of V_{dot} and $B_{\perp}$, with a fixed DC current-bias of 5 nA, where the DC current-bias was reset to zero before each pixel was acquired. At the voltage where the charge transition crosses zero energy, we observed a π shift of the supercurrent phase. This can be seen by comparing the phase of switching current oscillations between the e-state (Fig. B.5(b)) and the o-state (Fig. B.5(c)), at the V_{dot} positions indicated in Fig. B.3. In the first lobe, the π shift was absent as seen by comparing the e-state (Fig. B.5(d)) and the o-state (Fig. B.5(e)).

Reviewing the key observations relating to the switching current in device 1 we found that devices 2 and 3 reproduced the following behavior:

(i) In the zeroth lobe, a π phase shift between the e-state and the o-state was observed; for device 2 compare Figs. B.4(a,b), for device 3 compare Figs. B.5(b,c).
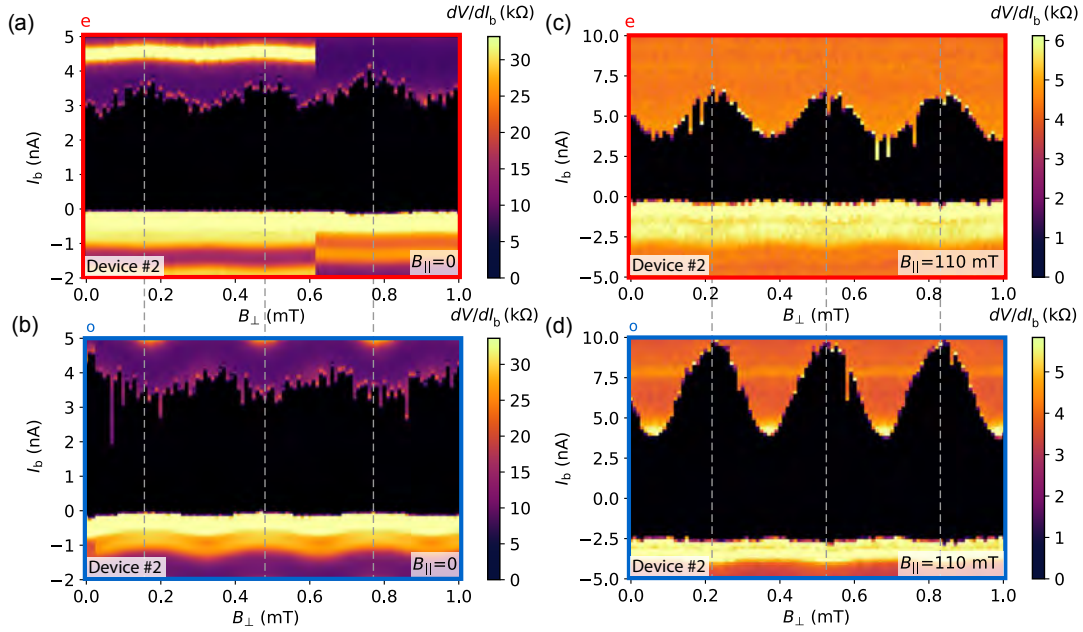
Figure B.4: Differential resistance, dV/dI_b**, of device 2 as a function of bias current,** I_b**, and perpendicular magnetic field,** $B_\perp$. (a,b) in the zeroth lobe, along cuts through the $e(o)$- state [red(blue) line in Fig. B.2(a)], showing relative π phase shift, and (c,d) in the first lobe, along cuts through the $e(o)$-state [red(blue) dashed line in Fig. B.2(b)], showing absence of phase shift. Note that in the zeroth lobe ((a) and (b)) the magnitude of the oscillations in switching current are similar; however, in the first lobe the magnitude of the oscillations in the o-state (d) is significantly larger than in the e-state (c).

(ii) In the first lobe, no phase shift between the e-state and the o-state was observed; for device 2 compare Figs. B.4(c,d), for device 3 compare Figs. B.5(d,e).

(iii) The absolute phases of critical current oscillations are aligned for both lobes and parities, with a π phase shift for the o-state in the zeroth lobe; for device 2 see Fig. B.5(b), and for device 3 see Fig. B.4(b).

(iv) The amplitude of the oscillatory component of the switching current is larger for the o-state than for the e-state; for device 2 compare Figs. B.4(b,d), for device 3 compare Figs. B.5(d,e).
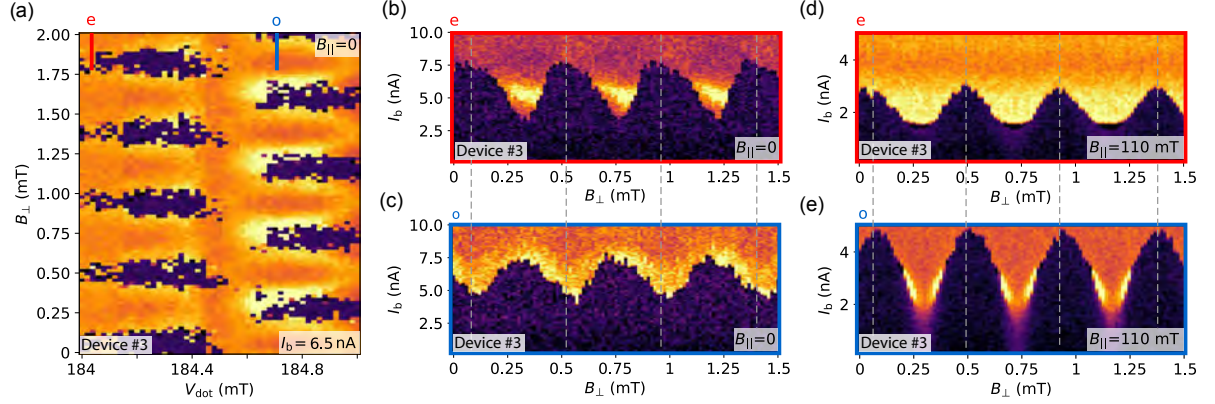
Figure B.5: Differential resistance, dV/dI_b**, of device 3 as a function of bias current,** I_b**, and perpendicular magnetic field,** $B_\perp$. (a) dV/dI_b as a function of V_{dot} and $B_\perp$ at fixed DC bias $I_b = 6.5\,nA$, the current is reset to zero before each pixel is acquired; a π phase shift in the zero-resistance state is observed crossing from the e-state to the o-state. (b,c) in the zeroth lobe, along cuts through the $e(o)$- state [red(blue) line in Fig. B.5(a)], showing relative π phase shift, and (d,e) in the first lobe, along cuts through the $e(o)$-state [red(blue) dashed line in Fig. Fig. B.5(a)], showing absence of phase shift. In the zeroth lobe ((b) and (c)) the magnitude of the oscillations in switching current are similar; however, in the first lobe the magnitude of the oscillations in the o-state (e) is significantly larger than in the e-state (d).

B.4 Main device
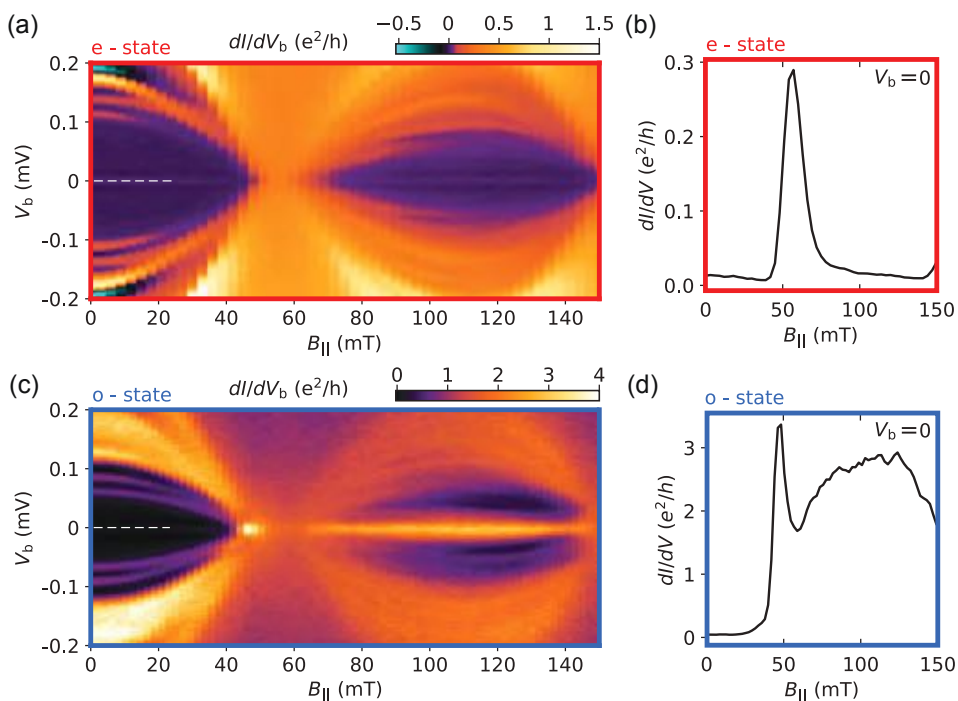
Figure B.6: Voltage-bias spectroscopy as a function of axial-field evolution for even and odd quantum dot occupancies.
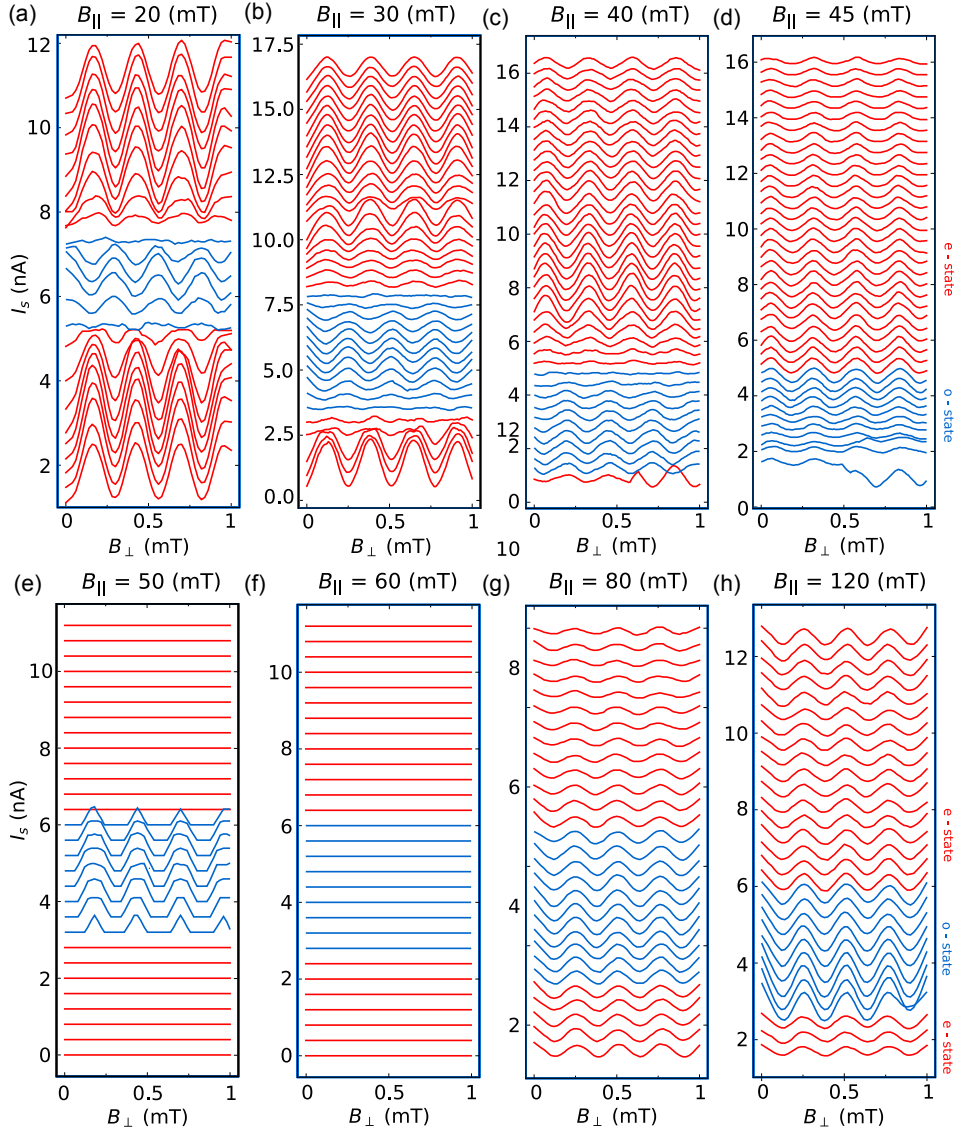
Figure B.7: Switching currents (I_s) across dot-junction charge occupancies (even-odd-even) with V_{dot} at different axial magnetic fields $B_{\parallel}$. Each curve offset by 0.4 nA. (a) Switching currents at $B_{\parallel} = 20$ mT crossing even (red), odd (blue) and back to even (red). A π-shift is visible between even and odd states. (b) Same as (a) only at $B_{\parallel} = 30$ mT. (c) Same as (b) only at $B_{\parallel} = 40$ mT. (d) Switching currents at $B_{\parallel} = 45$ mT where the bright conductance peak was observed [see Fig. 4.2(d)], with no π-shift between even and odd charge occupancy. (e) Switching currents at $B_{\parallel} = 50$ mT with finite current phase amplitude only in the odd state, with insets showing $B_{\perp}$ as a function of applied current bias. (f) Switching currents at $B_{\parallel} = 60$ mT with no $B_{\perp}$ modulation of current phase amplitude. (g) Switching currents at $B_{\parallel} = 80$ mT with no π shift between the even and odd states. (h) Same as (g) only at $B_{\parallel} = 120$ mT with no π shift between the even and odd states. In addition, increase in current-phase amplitude modulation in the odd state relative to even state is observed.

C

COULOMB PEAK SPACING ANALYSIS

Coulomb blockade of a Majorana island has been proven to be useful tool in identifying finite length dependence of zero-energy modes in topological islands with finite charging energy. If Majorana zero-modes are living on the ends of a nanowire, then the wavefunction overlap will cause a finite energy splitting. Changing the charge offset on the island one can tunnel through individual charges on/off the island. At $B_\parallel = 0$, Cooper pair transport occurs with $2e$ charge at zero applied voltage. As the axial magnetic field is increased $2e$ degeneracy point peaks split in even-odd spacing, where now single electron transport is possible, because the lowest E_{odd} energy charge parabola is below the charging energy, E_C. Continuing to increase the axial field, the E_{odd} comes all the way down to zero energy and $1e$ spacing of charges can be seen from Coulomb blockade peaks.

Since our devices consist of a finite island length, topological nature of such structures will be highlighted in even-odd peak spacing difference:

$$\delta V = < \Delta_{even} > - < \Delta_{odd} >, \qquad (C.1)$$

with $< \Delta_{even} >$ and $< \Delta_{odd} >$ being mean peak spacing value in the

even and odd states [70] and is expressed:

$$< \Delta_{even} > = \frac{\sum_{k=0,2,4...}^{k_{max}} (p_{j+k} - p_{i+k})}{k_{max}} \tag{C.2}$$

$$< \Delta_{odd} > = \frac{\sum_{k=0,2,4...}^{k_{max}} (p_{i+k} - p_{j+k})}{k_{max}} \tag{C.3}$$

where i - even and j - odd number. Extracted mean peak spacing values were done of more than 20 consecutive $1e$ peaks (k_{max}). In Fig. C.1(a) differential conductance measurement of a Coulomb blockaded island at $B_{\parallel} = 0$ and $V_b = 0$ as a function of V_g, where $2e$ peaks can be identified. Multiple Lorentzian fit is applied to individual peak to find peak position and even peak spacing can be found, $< \Delta_{even} >$. As the axial magnetic field is increased to destructive regime $B_{\parallel} = 50$ mT, double amount of peaks are observed compared to $B_{\parallel} = 0$, with double amount of Lorentzian fits to find $< \Delta_{even} >$ and $< \Delta_{odd} >$ spacings.

The energy splitting amplitude is found by:

$$A = \mu + < \delta V >, \tag{C.4}$$

where μ is the lever arm found from Coulomb blockade diamonds from FIg. 5.2(a)-(b) and Fig. 5.6(a)-(b).
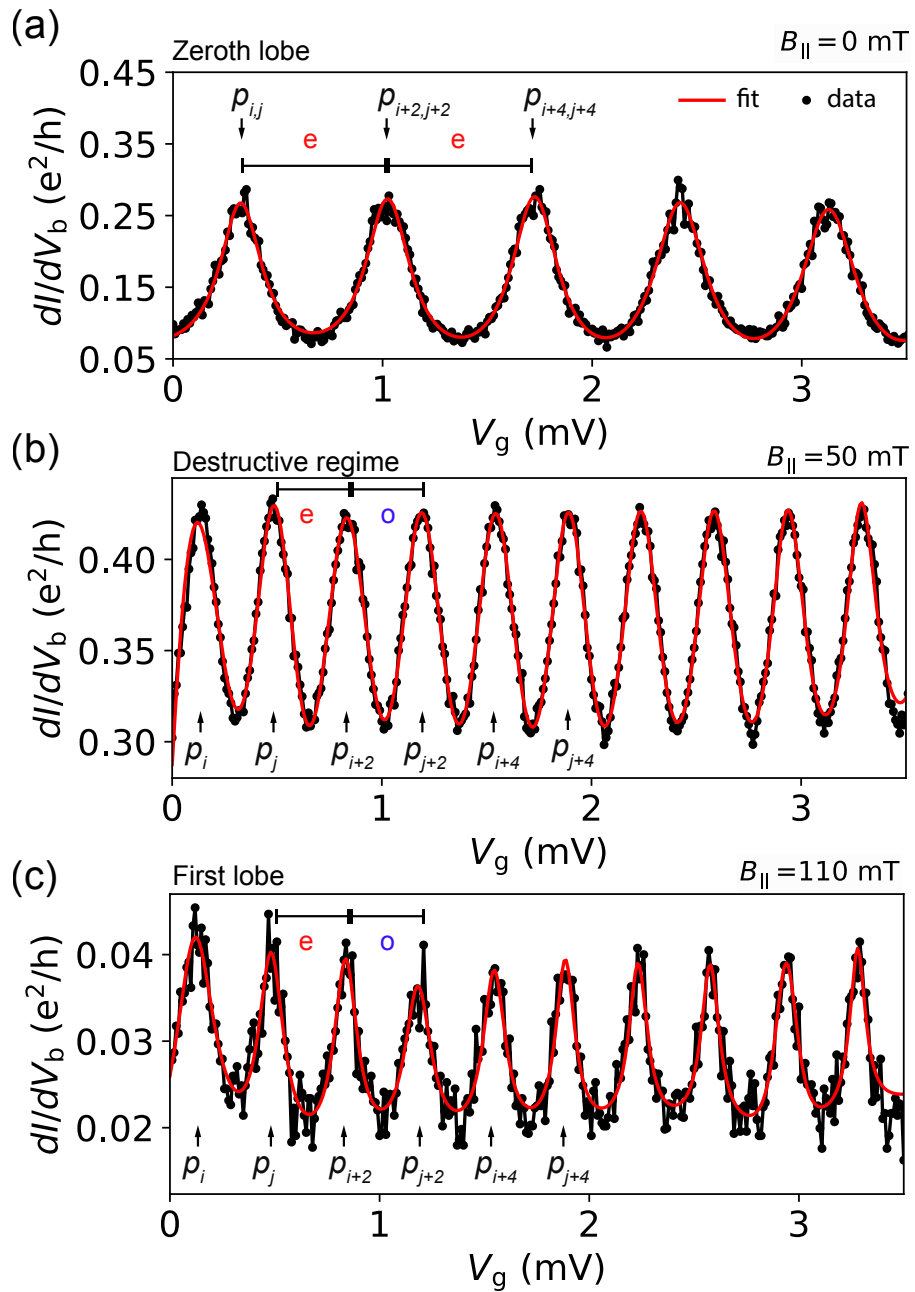
Figure C.1: Peak spacing extraction for different axial magnetic fields.

D

HIGH FREQUENCY MEASUREMENT TECHNIQUES

Reflectometry measurements presented in Fig. 2 and Fig. 6 were performed with the customized demodulation circuit presented in Fig. 7. Below we list other electronic equipment used in the experiments.
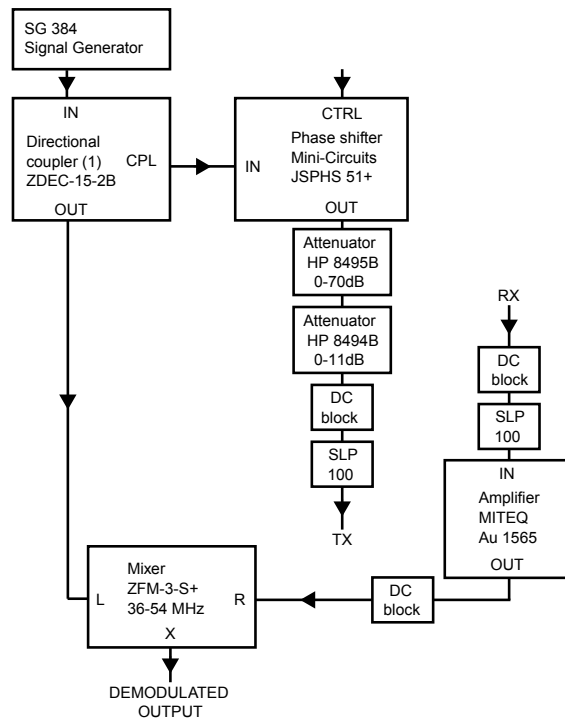
Figure D.1: Block diagram of demodulation circuit.

1. Demodulation unit used for reflectometry measurements in Fig. 6.5 and Fig. 6.6: Zurich Instruments, Ultrafast Lock-in Amplifier (600 MHz) [128]

2. Current-to-voltage converter: University of Basel, Electronics Lab, Low Noise/High stability I/V converter, SP 983 with IF3602

3. Voltage sources: 48-channel QDAC, custom digital-to-analog converters, QDevil ApS [177]

4. Lock-in: Stanford Research SR830 DSP Lock-in amplifier

5. Waveform generator: Keysight 33500B

6. Arbitrary waveform generator: Tektronix 5014 C, 1.2 GS/s

7. Vector network analyser: Rohde & Schwarz - ZVB8

8. Directional coupler: Minicircuits ZEDC-15-2B (1 MHz - 1 GHz)

9. Microwave switch Minicircuits ZASWA-2-50DR+ (DC - 5 GHz)

10. Cryogenic 4 K amplifier: Caltech Weinreb CITLF3

11. Digitizer: AlazarTech ATS9360 - 12 bit, 1.8 GS/s

E

DISPERSIVE SENSING

The resonant circuit, is made out of off-chip superconducting Nb on Al$_2$O$_3$ spiral inductor [161] in series with the distributed parasitic capacitance that includes a TiAu gates. Gates are bonded with 25 μm diameter Al (1% Si) bond wires. To reduce parasitic capacitances and maximize sensitivity we tried to minimize the bond wire length. The sample is loaded in a box which is surrounded with Eccosorb microwave absorbent material in order to minimize the effects due to stray radiation. Measurements were performed in an Oxford Instruments Triton 400 dilution refrigerator with a base electron temperature of $T \sim 20$ mK and a 6-1-1 T vector magnet. The table E.1 summarizes the resonant circuit parameters of two measured devices.

	L_1 (nH)	L_2 (nH)	f_1 (MHz)	f_2 (MHz)	$Q_{l,1}$	$Q_{l,2}$
Device 1	105	150	780	710	95	240
Device 2	420	310	440	510	50	60

Table E.1: Summary of inductor values used for two measured devices together with the bare resonance frequencies and loaded quality factors.

For reflectometry measurements a commercially available high frequency demodulation unit (Zurich Instruments UHFLI) was used. The RF carrier (frequency f_{rf}, amplitude V_{TX}) generated at room temperature was sent through high frequency coax line, followed by 21 dB of

distributed attenuators with a further 15 dB attenuation from the directional coupler (Minicircuits ZEDC-15-2B) mounted below the mixing chamber plate. The signal reflected from the rf circuit was amplified by approximately +40 dB with 4K amplifier (Caltech CITLF3). The amplified signal (amplitude V_{RX}) is detected at room temperature using homodyne detection inside of ZI lock-in with phase and magnitude information available for further processing. For microwave spectroscopy measurements in Fig. 4 the signal generator Rohde & Schwarz, RS SMB100A was used.

When transport measurements were performed the current I through the NW island was measured by connecting a current amplifier (Low Noise/High stability I/V converter, SP 983 IF3602) to the drain electrode of the device, while applying a voltage bias to the source electrode. Total voltage bias is the sum of a DC (V_B and a small AC voltage (excitation voltages in the range of 4 - 10 μV with excitation frequencies below 150 Hz). This allows the measurement of differential conductance, $g \equiv dI/dV_B$, by conventional lock-in detection (Stanford Research Systems SR830). The DC gates are connected to twisted pairs with a low pass cut-off frequency of ~ 1 kHz at base temperature. During the rf measurements the DC bias is set to zero unless stated otherwise. We note that the experimental setup resembles the one reported in detail in Ref. [55]. All data was acquired with the modular data acquisition framework QCoDeS.

[1]   H. Kamerlingh Onnes. Further experiments with liquid helium. C. on the change of electric resistance of pure metals at very low temperatures, etc. IV. the resistance of pure mercury at helium temperatures. *Comm. Phys. Lab. Univ. Leiden*, 120B, (1911).

[2]   L. D. Landau. The Theory of a Fermi Fiquid. *Zh. Eksp. Teor. Fiz.*, 30:1058, (1956).

[3]   Erkki Thuneberg. Introduction to Landau's Fermi Liquid Theory. *Department of physical sciences University of Oulu*, (2009).

[4]   R. P. Feynman, R. B. Leighton, and M. L. Sands. The Feynman lectures on physics. *Reading, Mass: Addison-Wesley Pub.*, (1963).

[5]   F. London and H. London. The electromagnetic equations of the supraconductor. *Proceedings of the Royal Society A: Mathematical, Physical and Engineering Sciences*, 149:866, (1935).

[6]   Leon N. Cooper. Bound Electron Pairs in a Degenerate Fermi Gas. *Phys. Rev.*, 104:1189–1190, (1956).

[7]   P. De Gennes. Superconductivity Of Metals And Alloys. *New York: Benjamin*, (1993).

[8]   G. E. Blonder, M. Tinkham, and T. Klapwijk. Transition from metallic to tunneling regimes in superconducting microconstric-

REFERENCES

tions: Excess current, charge imbalance, and supercurrent conversion. *Phys. Rev. B*, 25.7:4515–4532, (1982).

[9] Henri Juhani Suominen. Two-dimensional semiconductor-superconductor hybrids. *PhD thesis, University of Copnehagen, Center for Quantum Devices*, (2017).

[10] Y. V. Nazarov and Y. M. Blanter. Quantum Transport. Introduction to Nanoscience. *Cambridge University Press*, (2009).

[11] B. D. Josephson. Possible new effects in superconductive tunnelling. *Phys. Rev. Lett.*, 7(2):251–253, (1962).

[12] A. Barone and G. Paternó. Physics and Applications of the Josephson Effect. *John Wiley Sons, Inc., New York*, (1982).

[13] K.K. Likharev. Dynamics of Josephson Junctions and Circuits. *Gordon and Breach, New York*, (1986).

[14] I. O. Kulik. Macroscopic Quantization and the Proximity Effect in S-N-S Junctions. *Sov. Phys. JETP*, 30:966, (1969).

[15] Bascom S. Deaver and William M. Fairbank. Experimental evidence for quantized flux in superconducting cylinders. *Phys. Rev. Lett.*, 7:43–46, (1961).

[16] R. Doll and M. Näbauer. Experimental proof of magnetic flux quantization in a superconducting ring. *Phys. Rev. Lett.*, 7:51–52, (1961).

[17] S. M. Frolov. Current-phase relations of Josephson junctions with ferromagnetic barriers. *PhD thesis, University of Illinois at Urbana-Champaign*, (2005).

[18] D. B. Szombati. Superconducting InSb nanowire devices. *PhD thesis, TU Delft Kouwenhoven Lab*, (2017).

[19] T. Young. On the theory of light and colours (The 1801 Bakerian Lecture). *Philosophical Transactions of the Royal Society of London*, 92:12–48, (1801).

130

[20] M. Tinkham. Introduction to superconductivity. *Courier Corporation*, (2004).

[21] L. N. Bulaevskii, V. V. Kuzii, and A. A. Sobyanin. Superconducting system with weak coupling to the current in the ground state. *JETP Lett.*, 25:290, (1977).

[22] I. Kulik. Magnitude of the Critical Josephson Tunnel Current. *Sov. Phys. JETP*, 22:841, (1966).

[23] L. I. Glazman and K. A. Matveev. Resonant Josephson current through Kondo impurities in a tunnel barrier. *JETP Lett.*, 49:659, (1989).

[24] F. Siano and R. Egger. Josephson Current through a Nanoscale Magnetic Quantum Dot. *Phys. Rev. Lett.*, 93:047002, (2004).

[25] Jorden A. van Dam, Yuli V. Nazarov, Erik P. A. M. Bakkers, Silvano De Franceschi, and Leo P Kouwenhoven. Supercurrent reversal in quantum dots. *Nature (London)*, 442(7103):667–670, (2006).

[26] H. Ingerslev Jørgensen, T. Novotný, K. Grove-Rasmussen, K. Flensberg, and P. E. Lindelof. Critical Current 0-π Transition in Designed Josephson Quantum Dot Junctions. *Nano Lett.*, 7(8):2441–2445, (2007).

[27] D. B. Szombati, S. Nadj-Perge, D. Car, S. R. Plissard, E. P. A. M. Bakkers, and L. P. Kouwenhoven. Josephson φ_0-junction in nanowire quantum dots. *Nat. Phys.*, 12:568–572, (2016).

[28] A. I. Larkin and Y. N. Ovchinnikov. Nonuniform state of superconductors. *Sov. Phys. JETP*, (1965).

[29] Peter Fulde and Richard A. Ferrell. Superconductivity in a strong spin-exchange field. *Phys. Rev.*, 135:A550–A563, (1964).

[30] P. W. Anderson. Localized magnetic states in metals. *Phys. Rev.*, 124:41–53, (1961).

REFERENCES

[31] D. J. Thouless, M. Kohmoto, M. P. Nightingale, and M. den Nijs. Quantized hall conductance in a two-dimensional periodic potential. *Phys. Rev. Lett.*, 49:405–408, (1982.

[32] C. L. Kane and E. J. Mele. Quantum spin hall effect in graphene. *Phys. Rev. Lett.*, 95:226801, (2005).

[33] C. L. Kane and E. J. Mele. Z_2 topological order and the quantum spin hall effect. *Phys. Rev. Lett.*, 95:146802, (2005).

[34] P. A. M. Dirac. The quantum theory of the electron. *Proc. R. Soc. Lond. A*, 117, (1928).

[35] E. Majorana. Teoria simmetrica dell'elettrone e del positrone, (a symmetric theory of electrons and positrons). *Nuovo Cim.*, 14, (1937).

[36] Martin Leijnse and Karsten Flensberg. Introduction to topological superconductivity and Majorana fermions. *Semiconductor Science and Technology*, 27(12):124003, (2012).

[37] Liang Fu and C. L. Kane. Superconducting Proximity Effect and Majorana Fermions at the Surface of a Topological Insulator. *Phys. Rev. Lett.*, 100:096407, (2008).

[38] Yuval Oreg, Gil Refael, and Felix von Oppen. Helical Liquids and Majorana Bound States in Quantum Wires. *Phys. Rev. Lett.*, 105:177002, (2010).

[39] Roman M. Lutchyn, Jay D. Sau, and S. Das Sarma. Majorana fermions and a topological phase transition in semiconductor-superconductor heterostructures. *Phys. Rev. Lett.*, 105(7):07701, (2010).

[40] A. Yu Kitaev. Unpaired Majorana fermions in quantum wires. *Physics-Uspekhi*, 44(10S):131–136, (2001).

[41] D. A. Ivanov. Non-abelian statistics of half-quantum vortices in p-wave superconductors. *Phys. Rev. Lett.*, 86:268–271, (2001).

[42] Anindya Das, Yuval Ronen, Yonatan Most, Yuval Oreg, Moty Heiblum, and Hadas Shtrikman. Zero-bias peaks and splitting in an Al–InAs nanowire topological superconductor as a signature of Majorana fermions. *Nat. Phys.*, 8:887–895, (2012).

[43] Christoph W. Groth, Michael Wimmer, Anton R. Akhmerov, and Xavier Waintal. Kwant: a software package for quantum transport. *N. J. of Phys.*, 16(6):063065, (2014).

[44] Sven Albrecht. Quasiparticle dynamics and exponential protection in Majorana islands. *PhD thesis, University of Copnehagen, Center for Quantum Devices*, (2016).

[45] R. S. Wagner and W. C. Ellis. VAPOR-LIQUID-SOLID MECHANISM OF SINGLE CRYSTAL GROWTH. *Appl. Phys. Lett.*, 4:89, (1964).

[46] P. Krogstrup, N. L. B. Ziino, W. Chang, S. M. Albrecht, M. H. Madsen, E. Johnson, J. Nygård, C. M. Marcus, and T. Sand-Jespersen. Epitaxy of semiconductor–superconductor nanowires. *Nat. Mater.*, 14(4):400–406, (2015).

[47] Damon J. Carrad, Martin Bjergfelt, Thomas Kanne, Martin Aagesen, Filip Krizek, Elisabetta M. Fiordaliso, Erik Johnson, Jesper Nygård, and Thomas Sand-Jespersen. Shadow epitaxy for in situ growth of generic semiconductor/superconductor hybrids. *Advanced Materials*, 32(23):1908411, (2020).

[48] Willy Chang, Sven M. Albrecht, Thomas Sand-Jespersen, Ferdinand Kuemmeth, Peter Krogstrup, Jesper Nygård, and Charles Marcus M. Hard gap in epitaxial semiconductor–superconductor nanowires. *Nat. Nanotech.*, 10:232–236, (2015).

[49] Morten Kjaergaard. Proximity induced superconducting properties in one and two dimensional semiconductors. towards topological states of matter. *PhD thesis, University of Copnehagen, Center for Quantum Devices*, (2015).

[50] Jason Alicea. New directions in the pursuit of Majorana fermions in solid state systems. *Rep. Prog. Phys.*, 75(7):076501, (2012).

REFERENCES

[51] Jason Alicea, Yuval Oreg, Gil Refael, Felix von Oppen, and Matthew P. A. Fisher. Non-Abelian statistics and topological quantum information processing in 1D wire networks. *Nat. Phys.*, 7:412, (2011).

[52] David Aasen, Michael Hell, Ryan V. Mishmash, Andrew Higginbotham, Jeroen Danon, Martin Leijnse, Thomas Sand-Jespersen, Joshua A. Folk, Charles M. Marcus, Karsten Flensberg, and Jason Alicea. Milestones Toward Majorana-Based Quantum Computing. *Phys. Rev. X*, 6:031016, (2016).

[53] Torsten Karzig, Christina Knapp, Roman M. Lutchyn, Parsa Bonderson, Matthew B. Hastings, Chetan Nayak, Jason Alicea, Karsten Flensberg, Stephan Plugge, Yuval Oreg, Charles M. Marcus, and Michael H. Freedman. Scalable designs for quasiparticle-poisoning-protected topological quantum computation with Majorana zero modes. *Phys. Rev. B*, 95:235305, (2017).

[54] K. D. Petersson, C. G. Smith, D. Anderson, P. Atkinson, G. A. C. Jones, and D. A. Ritchie. Charge and Spin State Readout of a Double Quantum Dot Coupled to a Resonator. *Nano Lett.*, 10(8):2789–2793, (2010).

[55] Davydas Razmadze, Deividas Sabonis, Filip K. Malinowski, Gerbold C. Ménard, Sebastian Pauka, Hung Q. Nguyen, David M.T. van Zanten, Eoin C.T. O'Farrell, Judith Suter, Peter Krogstrup, Ferdinand Kuemmeth, and Charles M. Marcus. Radio-frequency methods for majorana-based quantum devices: Fast charge sensing and phase-diagram mapping. *Phys. Rev. Appl.*, 11:064011, (2019).

[56] David Aasen, Michael Hell, Ryan V. Mishmash, Andrew Higginbotham, Jeroen Danon, Martin Leijnse, Thomas Sand-Jespersen, Joshua A. Folk, Charles M. Marcus, Karsten Flensberg, and Jason Alicea. Milestones Toward Majorana-Based Quantum Computing. *Phys. Rev. X*, 6(3):031016, (2016).

[57] S. M. Albrecht, A. P. Higginbotham, M. Madsen, F. Kuemmeth, T. Sand-Jespersen, J. Nygård, P. Krogstrup, and C. M. Marcus. Ex-

ponential protection of zero modes in Majorana islands. *Nature*, 531(7593):206–209, (2016).

[58] M. T. Deng, S. Vaitiekėnas, E. B. Hansen, J. Danon, M. Leijnse, K. Flensberg, J. Nygård, P. Krogstrup, and C. M. Marcus. Majorana bound state in a coupled quantum-dot hybrid-nanowire system. *Science*, 354(6319):1557–1562, (2016).

[59] V. Mourik, K. Zuo, S. M. Frolov, S. R. Plissard, E. P. A. M. Bakkers, and L. P. Kouwenhoven. Signatures of Majorana fermions in hybrid superconductor-semiconductor nanowire devices. *Science*, 336(6084):1003, (2012).

[60] B. van Heck, T. Hyart, and C. W. J. Beenakker. Minimal circuit for a flux-controlled Majorana qubit in a quantum spin-Hall insulator. *Physica Scripta*, T164:014007, (2015).

[61] A. P. Higginbotham, S. M. Albrecht, G. Kirsanskas, W. Chang, F. Kuemmeth, P. Krogstrup, T. Sand-Jespersen, J. Nygård, K. Flensberg, and C. M. Marcus. Parity lifetime of bound states in a proximitized semiconductor nanowire. *Nat. Phys.*, 11(12):1017–1021, (2015).

[62] Hao Zhang, Chun-Xiao Liu, Sasa Gazibegovic, Di Xu, John A. Logan, Guanzhong Wang, Nick van Loo, Jouri D. S. Bommer, Michiel W. A. de Moor, Diana Car, Roy L. M. Op het Veld, Petrus J. van Veldhoven, Sebastian Koelling, Marcel A. Verheijen, Mihir Pendharkar, Daniel J. Pennachio, Borzoyeh Shojaei, Joon Sue Lee, Chris J. Palmstrøm, Erik P. A. M. Bakkers, S. Das Sarma, and Leo P. Kouwenhoven. Quantized Majorana conductance. *Nature*, 556:1476–4687, (2018).

[63] C. W. J. Beenakker. Quantum transport in semiconductor-superconductor microjunctions. *Phys. Rev. B*, 46:12841–12844, 1992.

[64] D. Razmadze, E. C. T. O'Farell, P. Krogstrup, and C. M Marcus. Quantum-Dot Parity Effects in Trivial and Topological Josephson Junctions. *arXiv:2005.11848*, (2020).

REFERENCES

[65] A. Yu Kitaev. Fault-tolerant quantum computation by anyons. *Ann. Phys. (Amsterdam)*, 303:2–30, (2003).

[66] Chetan Nayak, Steven H. Simon, Ady Stern, Michael Freedman, and Sankar Das Sarma. Non-abelian anyons and topological quantum computation. *Rev. Mod. Phys.*, 80:1083–1159, (2008).

[67] P. San-Jose, J. Cayao, and E. Prada. Majorana bound states from exceptional points in non-topological superconductors. *Sci. Rep.*, 6:21427, (2016).

[68] Jorge Cayao, Elsa Prada, Pablo San-Jose, and Ramón Aguado. SNS junctions in nanowires with spin-orbit coupling: Role of confinement and helicity on the subgap spectrum. *Phys. Rev. B*, 91:024514, (2015).

[69] R. M. Lutchyn, E. P. A. M. Bakkers, L. P. Kouwenhoven, P. Krogstrup, C. M. Marcus, and Y. Oreg. Majorana zero modes in superconductor–semiconductor heterostructures. *Nat. Rev. Mat.*, 3:52–68, (2018).

[70] S. Vaitiekėnas, G. W. Winkler, B. van Heck, T. Karzig, M. T. Deng, K. Flensberg, L. I. Glazman, C. Nayak, P. Krogstrup, R. M. Lutchyn, and C. M. Marcus. Flux-induced topological superconductivity in full-shell nanowires. *Science*, 367(6485), (2020).

[71] W. A. Little and R. D. Parks. Observation of quantum periodicity in the transition temperature of a superconducting cylinder. *Phys. Rev. Lett.*, 9:9–12, (1962).

[72] M. R. Buitelaar, T. Nussbaumer, and C. Schönenberger. Quantum Dot in the Kondo Regime Coupled to Superconductors. *Phys. Rev. Lett.*, 89:256801, (2002).

[73] Mahn-Soo Choi, Minchul Lee, Kicheon Kang, and W. Belzig. Kondo effect and Josephson current through a quantum dot between two superconductors. *Phys. Rev. B*, 70:020502, (2004).

[74] Eduardo J. H. Lee, Xiaocheng Jiang, Ramón Aguado, Georgios Katsaros, Charles M. Lieber, and Silvano De Franceschi. Zero-bias

anomaly in a nanowire quantum dot coupled to superconductors. *Phys. Rev. Lett.*, 109:186802, (2012).

[75] K. Grove-Rasmussen, H. Ingerslev Jørgensen, and P. E. Lindelof. Kondo resonance enhanced supercurrent in single wall carbon nanotube Josephson junctions. *N. J. Phys.*, 9(5):124–124, (2007).

[76] T. Sand-Jespersen, J. Paaske, B. M. Andersen, K. Grove-Rasmussen, H. I. Jørgensen, M. Aagesen, C. B. Sørensen, P. E. Lindelof, K. Flensberg, and J. Nygård. Kondo-Enhanced Andreev Tunneling in InAs Nanowire Quantum Dots. *Phys. Rev. Lett.*, 99:126603, (2007).

[77] A. Eichler, M. Weiss, S. Oberholzer, C. Schönenberger, A. Levy Yeyati, J. C. Cuevas, and A. Martín-Rodero. Even-Odd Effect in Andreev Transport through a Carbon Nanotube Quantum Dot. *Phys. Rev. Lett.*, 99:126602, (2007).

[78] C. Buizert, A. Oiwa, K. Shibata, K. Hirakawa, and S. Tarucha. Kondo Iniversal Scaling for a Quantum Dot Coupled to Superconducting Leads. *Phys. Rev. Lett.*, 99:136806, (2007).

[79] C. Karrasch, A. Oguri, and V. Meden. Josephson current through a single Anderson impurity coupled to BCS leads. *Phys. Rev. B*, 77:024517, (2008).

[80] A. Eichler, R. Deblock, M. Weiss, C. Karrasch, V. Meden, C. Schönenberger, and H. Bouchiat. Tuning the Josephson current in carbon nanotubes with the Kondo effect. *Phys. Rev. B*, 79:161407, (2009).

[81] Y. Kanai, R. S. Deacon, A. Oiwa, K. Yoshida, K. Shibata, K. Hirakawa, and S. Tarucha. Electrical control of Kondo effect and superconducting transport in a side-gated InAs quantum dot Josephson junction. *Phys. Rev. B*, 82:054512, (2010).

[82] Romain Maurand, Tobias Meng, Edgar Bonet, Serge Florens, Laëtitia Marty, and Wolfgang Wernsdorfer. First-Order $0-\pi$

Quantum Phase Transition in the Kondo Regime of a Superconducting Carbon-Nanotube Quantum Dot. *Phys. Rev. X*, 2:011009, (2012).

[83] W. Chang, V. E. Manucharyan, Thomas Sand-Jespersen, J. Nygård, and C. M. Marcus. Tunneling Spectroscopy of Quasiparticle Bound States in a Spinful Josephson Junction. *Phys. Rev. Lett.*, 110:217005, (2013).

[84] Rok Žitko, Jong Soo Lim, Rosa López, and Ramón Aguado. Shiba states and zero-bias anomalies in the hybrid normal-superconductor Anderson model. *Phys. Rev. B*, 91:045441, (2015).

[85] V. Meden. The Anderson–Josephson quantum dot—a theory perspective. *J. Phys. Condens.*, 31(16):163001, (2019).

[86] J. C. Estrada Saldaña, R. Žitko, J. P. Cleuziou, E. J. H. Lee, V. Zannier, D. Ercolani, L. Sorba, R. Aguado, and S. De Franceschi. Charge localization and reentrant superconductivity in a quasiballistic InAs nanowire coupled to superconductors. *Sci. Adv.*, 5(7), (2019).

[87] A. Kadlecová, M. Žonda, V. Pokorný, and T. Novotný. Practical Guide to Quantum Phase Transitions in Quantum-Dot-Based Tunable Josephson Junctions. *Phys. Rev. Appl.*, 11:044094, (2019).

[88] R. Delagrange, R. Weil, A. Kasumov, M. Ferrier, H. Bouchiat, and R. Deblock. 0-π quantum transition in a carbon nanotube Josephson junction: Universal phase dependence and orbital degeneracy. *Phys. Rev. B*, 93:195437, (2016).

[89] Z. Gao, W. J. Gong, S. F. Zhang, G. Y. Yi, and Y. S. Zheng. Tunable fractional Josephson effect in the topological superconducting junction with embedded quantum dots. *Europhys. Lett.*, 109(4):40010, (2015).

[90] Alberto Camjayi, Liliana Arrachea, Armando Aligia, and Felix von Oppen. Fractional Spin and Josephson Effect in Time-Reversal-Invariant Topological Superconductors. *Phys. Rev. Lett.*, 119:046801, (2017).

[91] Constantin Schrade and Liang Fu. Andreev or Majorana, Cooper finds out. *arXiv1809.06370*, (2018).

[92] Oladunjoye A. Awoga, Jorge Cayao, and Annica M. Black-Schaffer. Supercurrent detection of topologically trivial zero-energy states in nanowire junctions. *Phys. Rev. Lett.*, 123:117001, (2019).

[93] J. Schulenborg and K. Flensberg. Absence of supercurrent sign reversal in a topological junction with a quantum dot. *Phys. Rev. B*, 101:014512, (2020).

[94] Meng Cheng, Michael Becker, Bela Bauer, and Roman M. Lutchyn. Interplay between Kondo and Majorana Interactions in Quantum Dots. *Phys. Rev. X*, 4:031051, (2014).

[95] Gabriel Sellier, Thilo Kopp, Johann Kroha, and Yuri S. Barash. π junction behavior and Andreev bound states in Kondo quantum dots with superconducting leads. *Phys. Rev. B*, 72:174502, (2005).

[96] R. Allub and C. R. Proetto. Hybrid quantum dot–superconducting systems: Josephson current and Kondo effect in the narrow-band limit. *Phys. Rev. B*, 91:045442, (2015).

[97] Eric M. Spanton, Ming Tang Deng, Saulius Vaitiekėnas, Peter Krogstrup, Jesper Nygård, Charles M. Marcus, and Kathryn A. Moler. Current-phase relations of few-mode InAs nanowire Josephson junctions. *Nat. Phys.*, 13:1177, (2017).

[98] A. Zazunov, R. Egger, T. Jonckheere, and T. Martin. Anomalous Josephson Current through a Spin-Orbit Coupled Quantum Dot. *Phys. Rev. Lett.*, 103:147004, (2009).

[99] Liang Fu and C. L. Kane. Josephson current and noise at a superconductor/quantum-spin-hall-insulator/superconductor junction. *Phys. Rev. B*, 79:161408, (2009).

[100] M. Veldhorst, C. G. Molenaar, C. J. M. Verwijs, H. Hilgenkamp, and A. Brinkman. Optimizing the Majorana character of SQUIDs

with topologically nontrivial barriers. *Phys. Rev. B*, 86:024509, (2012).

[101] Silvano De Franceschi, Leo Kouwenhoven, Christian Schönenberger, and Wolfgang Wernsdorfer. Hybrid superconductor–quantum dot devices. *Nat. Nano.*, 5(10):703–711, (2010).

[102] A. Martín-Rodero and A. Levy Yeyati. Josephson and Andreev transport through quantum dots. *Advances in Physics*, 60(6):899–958, (2011).

[103] B. I. Spivak and S. A. Kivelson. Negative local superfluid densities: The difference between dirty superconductors and dirty Bose liquids. *Phys. Rev. B*, 43:3740–3743, (1991).

[104] A. V. Rozhkov, Daniel P. Arovas, and F. Guinea. Josephson coupling through a quantum dot. *Phys. Rev. B*, 64:233301, (2001).

[105] E. Vecino, A. Martín-Rodero, and A. Levy Yeyati. Josephson current through a correlated quantum level: Andreev states and π junction behavior. *Phys. Rev. B*, 68:035105, (2003).

[106] F. W. J. Hekking, L. I. Glazman, K. A. Matveev, and R. I. Shekhter. Coulomb blockade of two-electron tunneling. *Phys. Rev. Lett.*, 70:4138–4141, (1993).

[107] Yong-hui Zhang, Steffen Kahle, Tobias Herden, Christophe Stroh, Marcel Mayor, Uta Schlickum, Markus Ternes, Peter Wahl, and Klaus Kern. Temperature and magnetic field dependence of a Kondo system in the weak coupling regime. *Nat. Comm.*, 4:2110, (2013).

[108] Constantin Schrade, Silas Hoffman, and Daniel Loss. Detecting topological superconductivity with φ_0 Josephson junctions. *Phys. Rev. B*, 95:195421, (2017).

[109] Sagar Vijay and Liang Fu. Teleportation-based quantum information processing with Majorana zero modes. *Phys. Rev. B*, 94:235446, (2016).

[110] S. Plugge, A. Rasmussen, R. Egger, and K. Flensberg. Majorana box qubits. *N. J. Phys.*, 19:012001, (2017).

[111] Markus Reiher, Nathan Wiebe, Krysta M. Svore, Dave Wecker, and Matthias Troyer. Elucidating reaction mechanisms on quantum computers. *Proc. Nat. Academ. Sci.*, 114(29):7555–7560, (2017).

[112] Diego Rainis and Daniel Loss. Majorana qubit decoherence by quasiparticle poisoning. *Phys. Rev. B*, 85:174533, (2012).

[113] John M. Martinis, S. Nam, J. Aumentado, and C. Urbina. Rabi Oscillations in a Large Josephson-Junction Qubit. *Phys. Rev. Lett.*, 89:117901, (2002).

[114] A. Wallraff, D. I. Schuster, A. Blais, L. Frunzio, R.-S. Huang, S. Kumar, S. M. Girvin, and R. J. and Schoelkopf. Strong coupling of a single photon to a superconducting qubit using circuit quantum electrodynamics. *Nature*, 431:162–167, (2004).

[115] A. Wallraff, D. I. Schuster, A. Blais, L. Frunzio, J. Majer, M. H. Devoret, S. M. Girvin, and R. J. Schoelkopf. Approaching Unit Visibility for Control of a Superconducting Qubit with Dispersive Readout. *Phys. Rev. Lett.*, 95:060501, (2005).

[116] L. Casparis, T. W. Larsen, M. S. Olsen, F. Kuemmeth, P. Krogstrup, J. Nygård, K. D. Petersson, and C. M. Marcus. Gatemon Genchmarking and Two-Qubit Operations. *Phys. Rev. Lett.*, 116:150505, (2016).

[117] D. J. Reilly, J. M. Taylor, J. R. Petta, C. M. Marcus, M. P. Hanson, and A. C. Gossard. Suppressing Spin Qubit Dephasing by Nuclear State Preparation. *Science*, 321(5890):817–821, (2008).

[118] C. Barthel, M. Kjærgaard, J. Medford, M. Stopa, C. M. Marcus, M. P. Hanson, and A. C. Gossard. Fast sensing of double-dot charge arrangement and spin state with a radio-frequency sensor quantum dot. *Phys. Rev. B*, 81:161308, (2010).

[119] J. R. Petta, A. C. Johnson, J. M. Taylor, E. A. Laird, A. Yacoby, M. D. Lukin, C. M. Marcus, M. P. Hanson, and A. C. Gossard. Coherent

REFERENCES

Manipulation of Coupled Electron Spins in Semiconductor Quantum Dots. *Science*, 309(5744):2180–2184, (2005).

[120] R. Hanson, L. P. Kouwenhoven, J. R. Petta, S. Tarucha, and L. M. K. Vandersypen. Spins in few-electron quantum dots. *Rev. Mod. Phys.*, 79:1217–1265, (2007).

[121] M. Jung, M. D. Schroer, K. D. Petersson, and J. R. Petta. Radio frequency charge sensing in InAs nanowire double quantum dots. *Appl. Phys. Lett.*, 100(25):253508, (2012).

[122] M. D. Schroer, M. Jung, K. D. Petersson, and J. R. Petta. Radio Frequency Charge Parity Meter. *Phys. Rev. Lett.*, 109:166804, (2012).

[123] K. D. Petersson, C. G. Smith, D. Anderson, P. Atkinson, G. A. C. Jones, and D. A. Ritchie. Charge and spin state readout of a double quantum dot coupled to a resonator. *Nano Lett.*, 10(8):2789–2793, (2010).

[124] D. J. Reilly, C. M. Marcus, M. P. Hanson, and A. C. Gossard. Fast single-charge sensing with a rf quantum point contact. *Appl. Phys. Lett.*, 91(16):162101, (2007).

[125] N. Ares, F. J. Schupp, A. Mavalankar, G. Rogers, J. Griffiths, G. A. C. Jones, I. Farrer, D. A. Ritchie, C. G. Smith, A. Cottet, G. A. D. Briggs, and E. A. Laird. Sensitive Radio-Frequency Measurements of a Quantum Dot by Tuning to Perfect Impedance Matching. *Phys. Rev. Appl.*, 5:034011, (2016).

[126] Electronic access:. https://www.coilcraft.com. Accessed: 2019-09-30.

[127] Electronic access:. https://www.physik.unibas.ch. Accessed: 2018-09-30.

[128] Electronic access:. https://www.zhinst.com/products/uhfl. Accessed: 2019-09-30.

[129] Yongjie Hu, Hugh O. H. Churchill, David J. Reilly, Jie Xiang, Charles M. Lieber, and Charles M. Marcus. A Ge/Si heterostructure nanowire-based double quantum dot with integrated charge sensor. *Nat. Nanotech.*, 2:622–625, (2007).

[130] Luka Trifunovic, Oliver Dial, Mircea Trif, James R. Wootton, Rediet Abebe, Amir Yacoby, and Daniel Loss. Long-Distance Spin-Spin Coupling via Cloating Gates. *Phys. Rev. X*, 2:011006, (2012).

[131] Guilherme Tosi, Fahd A. Mohiyaddin, Vivien Schmitt, Stefanie Tenberg, Rajib Rahman, Gerhard Klimeck, and Andrea Morello. Silicon quantum processor with robust long-distance qubit couplings. *Nat. Com.*, 8:450, (2017).

[132] J. Stehlik, Y.-Y. Liu, C. M. Quintana, C. Eichler, T. R. Hartke, and J. R. Petta. Fast Charge Censing of a Cavity-Coupled Double Quantum Dot Using a Josephson Parametric Amplifier. *Phys. Rev. Appl.*, 4:014018, (2015).

[133] P. Joyez, P. Lafarge, A. Filipe, D. Esteve, and M. H. Devoret. Observation of parity-induced suppression of Josephson tunneling in the superconducting single electron transistor. *Phys. Rev. Lett.*, 72:2458–2461, (1994).

[134] K. A. Matveev, M. Gisselfält, L. I. Glazman, M. Jonson, and R. I. Shekhter. Parity-induced suppression of the Coulomb blockade of Josephson tunneling. *Phys. Rev. Lett.*, 70:2940–2943, (1993).

[135] S. V. Lotkhov, S. A. Bogoslovsky, A. B. Zorin, and J. Niemeyer. Cooper Pair Cotunneling in Single Charge Transistors with Dissipative Electromagnetic Environment. *Phys. Rev. Lett.*, 91:197002, (2003).

[136] D. Sherman, J. S. Yodh, S. M. Albrecht, J. Nygård, P. Krogstrup, and C. M. Marcus. Normal, superconducting and topological regimes of hybrid double quantum dots. *Phys. Rev. Lett.*, 12:212–217, (2017).

References

[137] C. Barthel, D. J. Reilly, C. M. Marcus, M. P. Hanson, and A. C. Gossard. Rapid Single-Shot Measurement of a Singlet-Triplet Qubit. *Phys. Rev. Lett.*, 103:160503, (2009).

[138] Damaz de Jong, Jasper van Veen, Luca Binci, Amrita Singh, Peter Krogstrup, Leo P. Kouwenhoven, Wolfgang Pfaff, and John D. Watson. Rapid detection of Coherent Tunneling in an InAs Nanowire Quantum Dot through Dispersive Gate Sensing. *Phys. Rev. Appl.*, 11:044061, (2019).

[139] M. G. House, I. Bartlett, P. Pakkiam, M. Koch, E. Peretz, J. van der Heijden, T. Kobayashi, S. Rogge, and M. Y. Simmons. High-Sensitivity Charge Detection with a Single-Lead Quantum Dot for Scalable Quantum Computation. *Phys. Rev. Appl.*, 6:044016, (2016).

[140] M. J. Biercuk, D. J. Reilly, T. M. Buehler, V. C. Chan, J. M. Chow, R. G. Clark, and C. M. Marcus. Charge sensing in carbon-nanotube quantum dots on microsecond timescales. *Phys. Rev. B*, 73:201402, (2006).

[141] S. J. Angus, A. J. Ferguson, A. S. Dzurak, and R. G. Clark. A silicon radio-frequency single electron transistor. *Appl. Phys. Lett.*, 92(11):112103, (2008).

[142] Mingyun Yuan, Zhen Yang, D. E. Savage, M. G. Lagally, M. A. Eriksson, and A. J. Rimberg. Charge sensing in a Si/SiGe quantum dot with a radio frequency superconducting single-electron transistor. *Appl. Phys. Lett.*, 101(14):142103, (2012).

[143] Deividas Sabonis, Eoin C. T. O'Farrell, Davydas Razmadze, David M. T. van Zanten, Judith Suter, Peter Krogstrup, and Charles M. Marcus. Dispersive sensing in hybrid InAs/Al nanowires. *Appl. Phys. Lett.*, 115(10):102601, (2019).

[144] R. J. Schoelkopf, P. Wahlgren, A. A. Kozhevnikov, P. Delsing, and D. E. Prober. The radio-frequency single-electron transistor (RF-SET): A fast and ultrasensitive electrometer. *Science*, 280(5367):1238–1242, (1998).

144

[145] M. C. Cassidy, A. S. Dzurak, R. G. Clark, K. D. Petersson, I. Farrer, D. A. Ritchie, and C. G. Smith. Single shot charge detection using a radio-frequency quantum point contact. *Appl. Phys. Lett.*, 91(22):222104, (2007).

[146] T. Müller, B. Küng, S. Hellmüller, P. Studerus, K. Ensslin, T. Ihn, M. Reinwald, and W. Wegscheider. An in situ tunable radio-frequency quantum point contact. *Appl. Phys. Lett.*, 97(20):202104, (2010).

[147] Samuel J. Hile, Matthew G. House, Eldad Peretz, Jan Verduijn, Daniel Widmann, Takashi Kobayashi, Sven Rogge, and Michelle Y. Simmons. Radio frequency reflectometry and charge sensing of a precision placed donor in silicon. *Appl. Phys. Lett.*, 107(9):093504, (2015).

[148] M.-C. Harabula, T. Hasler, G. Fülöp, M. Jung, V. Ranjan, and C. Schönenberger. Measuring a Quantum Dot with an Impedance-Matching On-Chip Superconducting *LC* Resonator at Gigahertz Frequencies. *Phys. Rev. Appl.*, 8:054006, (2017).

[149] T. Duty, G. Johansson, K. Bladh, D. Gunnarsson, C. Wilson, and P. Delsing. Observation of Quantum Capacitance in the Cooper-Pair Transistor. *Phys. Rev. Lett.*, 95:206807, (2005).

[150] J. I. Colless, A. C. Mahoney, J. M. Hornibrook, A. C. Doherty, H. Lu, A. C. Gossard, and D. J. Reilly. Dispersive readout of a few-electron double quantum dot with fast rf gate sensors. *Phys. Rev. Lett.*, 110:046805, (2013).

[151] Sankar Das Sarma, Michael Freedman, and Chetan Nayak. Majorana zero modes and topological quantum computation. *N. J. Phys. Quant. Inform.*, 1:15001, (2015).

[152] Daniel Litinski, Markus S. Kesselring, Jens Eisert, and Felix von Oppen. Combining topological hardware and topological software: Color-code quantum computing with topological superconductor networks. *Phys. Rev. X*, 7:031048, (2017).

REFERENCES

[153] Sagar Vijay, Timothy H. Hsieh, and Liang Fu. Majorana fermion surface code for universal quantum computation. *Phys. Rev. X*, 5:041038, (2015).

[154] Anderson West, Bas Hensen, Alexis Jouan, Tuomo Tanttu, Chih-Hwan Yang, Alessandro Rossi, M. Fernando Gonzalez-Zalba, Fay Hudson, Andrea Morello, David J. Reilly, and Andrew S. Dzurak. Gate-based single-shot readout of spins in silicon. *Nat. Nanotech.*, (2019).

[155] N. J. Lambert, A. A. Esmail, M. Edwards, F. A. Pollock, B. W. Lovett, and A. J. Ferguson. Quantum capacitance and charge sensing of a superconducting double dot. *Appl. Phys. Lett.*, 109(11):112603, (2016).

[156] G. Zheng, N. Samkharadze, M. L. Noordam, N. Kalhor, D. Brousse, A. Sammak, G. Scappucci, and L. M. K. Vandersypen. Rapid high-fidelity gate-based spin read-out in silicon. *arXiv:1901.00687v1*, (2019).

[157] Imtiaz Ahmed, James A. Haigh, Simon Schaal, Sylvain Barraud, Yi Zhu, Chang-min Lee, Mario Amado, Jason W. A. Robinson, Alessandro Rossi, John J. L. Morton, and M. Fernando Gonzalez-Zalba. Radio-frequency capacitive gate-based sensing. *Phys. Rev. Appl.*, 10:014018, (2018).

[158] A. Rossi, R. Zhao, A. S. Dzurak, and M. F. Gonzalez-Zalba. Dispersive readout of a silicon quantum dot with an accumulation-mode gate sensor. *Appl. Phys. Lett.*, 110(21):212101, (2017).

[159] Matias Urdampilleta, David J. Niegemann, Emmanuel Chanrion, Baptiste Jadot, Cameron Spence, Pierre-André Mortemousque, Christopher Bäuerle, Louis Hutin, Benoit Bertrand, Sylvain Barraud, Romain Maurand, Marc Sanquer, Xavier Jehl, Silvano De Franceschi, Maud Vinet, and Tristan Meunier. Gate-Based High Fidelity Spin Read-out in a CMOS Device. *arXiv:1809.04584v1*, (2018).

[160] S. Schaal, S. Barraud, J. J. L. Morton, and M. F. Gonzalez-Zalba. Conditional Dispersive Readout of a CMOS Single-Electron Memory Cell. *Phys. Rev. Appl.*, 9:054016, (2018).

[161] J. M. Hornibrook, J. I. Colless, A. C. Mahoney, X. G. Croot, S. Blanvillain, H. Lu, A. C. Gossard, and D. J. Reilly. Frequency multiplexing for readout of spin qubits. *Appl. Phys. Lett.*, 104(10):103108, (2014).

[162] M. F. Gonzalez-Zalba, S. Barraud, A. J. Ferguson, and A. C. Betz. Probing the limits of gate-based charge sensing. *Nat. Com.*, 6:6084, (2015).

[163] A. C. Betz, R. Wacquez, M. Vinet, X. Jehl, A. L. Saraiva, M. Sanquer, A. J. Ferguson, and M. F. Gonzalez-Zalba. Dispersively Detected Pauli Spin-Blockade in a Silicon Nanowire Field-Effect Transistor. *Nano Lett.*, 15(7):4622–4627, (2015).

[164] Alessandro Crippa, Romain Maurand, Dharmraj Kotekar-Patil, Andrea Corna, Heorhii Bohuslavskyi, Alexei O. Orlov, Patrick Fay, Romain Laviéville, Sylvain Barraud, Maud Vinet, Marc Sanquer, Silvano De Franceschi, and Xavier Jehl. Level Spectrum and Charge Relaxation in a Silicon Double Quantum Dot Probed by Dual-Qate Reflectometry. *Nano Lett.*, 17(2):1001–1006, (2017).

[165] M. Fernando Gonzalez-Zalba, Sergey N. Shevchenko, Sylvain Barraud, J. Robert Johansson, Andrew J. Ferguson, Franco Nori, and Andreas C. Betz. Gate-Sensing Coherent Charge Oscillations in a Silicon Field-Effect Transistor. *Nano Lett.*, 16(3):1614–1619, (2016).

[166] R. Mizuta, R. M. Otxoa, A. C. Betz, and M. F. Gonzalez-Zalba. Quantum and tunneling capacitance in charge and spin qubits. *Phys. Rev. B*, 95:045414, (2017).

[167] A. P. Higginbotham, T. W. Larsen, J. Yao, H. Yan, C. M. Lieber, C. M. Marcus, and F. Kuemmeth. Hole Spin Coherence in a Ge/Si Heterostructure Nanowire. *Nano Lett.*, 14(6):3582–3586, (2014).

147

REFERENCES

[168] D. de Jong, J. van Veen, L. Binci, A. Singh, P. Krogstrup, L. P. Kouwenhoven, W. Pfaff, and J. D. Watson. Rapid detection of coherent tunneling in an InAs nanowire quantum dot through dispersive gate sensing. *Appl. Phys. Lett.*, 11, (2018).

[169] Jasper van Veen, Damaz de Jong, Lin Han, Christian Prosko, Peter Krogstrup, John D. Watson, Leo P. Kouwenhoven, and Wolfgang Pfaff. Revealing charge-tunneling processes between a quantum dot and a superconducting island through gate sensing. *arXiv preprint arXiv:1903.09066*, (2019).

[170] M. C. Jarratt, A. Jouan, A. C. Mahoney, S. J. Waddy, G. C. Gardner, S. Fallahi, M. J. Manfra, and D. J. Reilly. Dispersive Gate Sensing the Quantum Capacitance of a Point Contact. *arXiv:1903.07793*.

[171] J. R. Petta, A. C. Johnson, C. M. Marcus, M. P. Hanson, and A. C. Gossard. Manipulation of a single charge in a double quantum dot. *Phys. Rev. Lett.*, 93:186802, (2004).

[172] David M. T. van Zanten, Deividas Sabonis, Judith Suter, Jukka I. Väyrynen, Torsten Karzig, Dmitry I. Pikulin, Eoin C. T. O'Farrell, Davydas Razmadze, Karl D Petersson, Peter Krogstrup, and Charles M. Marcus. Photon Assisted Tunneling of Zero Modes in a Majorana Wire. *Nat. Phys.*, 16:663–668, (2020).

[173] Henrik Brenning, Sergey Kafanov, Tim Duty, Sergey Kubatkin, and Per Delsing. An ultrasensitive radio-frequency single-electron transistor working up to 4.2k. *J. Appl. Phys.*, 100(11):114321, (2006).

[174] W. G. van der Wiel, S. De Franceschi, J. M. Elzerman, T. Fujisawa, S. Tarucha, and L. P. Kouwenhoven. Electron transport through double quantum dots. *Rev. Mod. Phys.*, 75:1–22, (2002).

[175] N. J. Lambert, A. A. Esmail, F. A. Pollock, M. Edwards, B. W. Lovett, and A. J. Ferguson. Microwave irradiation and quasiparticles in a superconducting double dot. *Phys. Rev. B*, 95(23):235413, (2017).

[176] L. P. Kouwenhoven, S. Jauhar, K. McCormick, D. Dixon, P. L. McEuen, Yu. V. Nazarov, N. C. van der Vaart, and C. T. Foxon. Photon-assisted tunneling through a quantum dot. *Phys. Rev. B*, 50:2019–2022, (1994).

[177] Electronic access:. https://www.qdevil.com. Accessed: 2019-09-30.